DEVELOPMENT OF A FINITE ELEMENT MODEL OF THE NEONATAL BRACHIAL PLEXUS

By

Sarah Jean Wright

A DISSERTATION

Submitted to
Michigan State University
in partial fulfillment of the requirements
for the degree of

Biomedical Engineering – Doctor of Philosophy

2024

ABSTRACT

Neonatal brachial plexus palsy (NBPP) is an injury to newborn infants that occurs during the birthing process in 1.5/1,000 total births (1). About 2/10,000 total births result in an injury that persists past 12 months of age and leads to a permanent deficit in upper extremity function. When injuries to the brachial plexus occur, they may be classified based on reference to a historical definition: Erb's palsy or Klumpke's palsy. Erb's palsy involves the C5/C6 nerve roots, while Klumpke's palsy involves damage to the lower cervical and upper thoracic nerve roots (C8-T1).

Based on previous research, it is known that both endogenous and exogenous forces can have a direct effect on the fetus during labor and delivery. Endogenous force refers to internal forces from the mother (uterine contractions and pushing), while exogenous force is an external force applied by the birthing attendant. This latter force may involve downward axial traction, aligned with the infant's spine, or downward lateral traction on the neonatal head, which causes bending of the fetus' neck away from the anterior shoulder. While the long-term assumption that lateral, bending traction can cause enough stretch to result in a permanent injury has been confirmed through experimental and modeling studies, recent research also indicates that maternal forces – alone or in combination with axial traction – are also a likely cause of NBPP (1). However, the pattern of stretching within the complete neonatal brachial plexus has not been characterized. Further research is needed to understand how the various delivery forces stretch the five nerve roots of the brachial plexus to better understand the mechanisms of NBPP. Brachial plexus research on neonates is difficult to conduct, as these subjects are unavailable for research – especially research that may cause injury or requires the harvesting of tissues. Different ways to analyze the brachial plexus may include cadaveric, animal, and computational models.

Computational models can give insight into brachial plexus injuries, as they can designate specific forces, dimensions, and material properties such that the specific effect of one parameter can be investigated. The objectives of this dissertation were to develop both a two-dimensional (2D) and a three-dimensional (3D) finite element model of the neonatal brachial plexus that can be validated based on previous *in vitro* experiments and clinical observations. Once validated, the model will be used to analyze which maternal, neonatal, and delivery factors may affect the stretch in the brachial plexus and therefore increase injury risk.

Specifically, three objectives were established for this project: (1) Conduct statistical analysis of clinical NBPP data to better document the types of injuries that occur and their

relationship to maternal and neonatal factors; (2) Develop and validate a 2D Model of the neonatal brachial plexus as an initial step in model development, which can then be used to investigate the effect of anatomical variations in a simplified structure; and (3) Develop and validate a 3D Model of the neonatal brachial plexus, which can then lead to an analysis of the effect that specific NBPP injuries have on the change of stress throughout the plexus.

Altogether, these objectives offer advances in the world of computational modeling and biomechanical nerve injuries by providing useful insight for researchers, neurosurgeons, and other medical professionals to scientifically evaluate biomechanical aspects of neonatal brachial plexus injuries – in the hope to provide useful insight in ways to lessen the chances of these injuries occurring.

ACKNOWLEDGEMENTS

I would like to express my deepest gratitude and appreciation to Dr. Michele Grimm for her exceptional guidance, expertise, and unwavering support throughout the duration of this research endeavor. Under the leadership of Dr. Michele Grimm, this project has flourished, and her extensive knowledge and dedication have played a vital role in its success. I am profoundly grateful for the continuous support and encouragement throughout this project. Her unwavering belief in my abilities has been a constant source of motivation throughout my Ph.D. candidacy.

I wish to extend my appreciation to Dr. Anita Singh from Temple University. Her valuable research and collaboration aided the advances in my models and the advancements of brachial plexus research as a whole. Dr. Anita Singh has provided invaluable insights, valuable suggestions, and constructive feedback at every stage of the project.

I would like to recognize the assistance provided by Dr. Whitney Muhlestein from the University of Michigan. I would like to acknowledge her ability to foster a collaborative and stimulating research environment. Her willingness to join forces for the better of science has shown her desire to contribute to the advancement of knowledge in this field.

It is with deep sorrow and profound respect that I acknowledge the late Dr. Lynda Ju-San Yang, M.D., Ph.D., our esteemed collaborator, who unfortunately passed away during the course of this research project. Although no longer with us, her invaluable contributions, unwavering dedication, and lasting impact on this endeavor deserve to be recognized and celebrated.

Lastly, I would like to take a moment to express my heartfelt gratitude and appreciation to my family and friends, who have been unwavering in their love, support, and understanding throughout my Ph.D. journey. Their constant encouragement, sacrifices, and belief in my abilities have been instrumental in my accomplishments, and I am deeply grateful for their presence in my life.

TABLE OF CONTENTS

LIST OF ABBREVIATIONS

2D	Two-Dimensional
3D	Three-Dimensional
ANOVA	Analysis of Variance
BMI	Body Mass Index
DRG	Dorsal Root Ganglion
FEA	Finite Element Analysis
FEM	Finite Element Modeling
NBPP	Neonatal Brachial Plexus Palsy
PNS	Peripheral Nervous System
SAS	Statistical Analysis Software
SD	Shoulder Dystocia

INTRODUCTION

Human anatomy is a complex and intricate arrangement of structures that interconnect the systems, organs, tissues, and cells that work together to sustain life and enable physiological functions. Studying human anatomy and the biomechanics of these anatomical structures is crucial in various fields, including medicine, physiology, and engineering. It provides insight into mechanisms of injuries, facilitates the development of interventions, and deepens our appreciation for the intricacies of the human body.

Peripheral nerves are often researched to analyze anatomy and physiology, primarily through the lens of clinical practice or basic physiology and pathophysiology studies. Specifically, a section of the peripheral nerves known as the brachial plexus has been researched for the past century in relation to the occurrence of injuries to this set of nerves during the birthing process. The brachial plexus is a complex network of nerves that originates from the cervical spinal cord (C5-T1) and extends down the upper extremity, providing motor and sensory innervation to all aspects of the upper extremity **(Chapter 1,2,3)**. During the birthing process, this network may become injured – and this pattern of injury is generally referred to as Neonatal Brachial Plexus Palsy (NBPP).

In 1927, it was believed "that almost without exception, injuries of the cord or plexus are due to unphysiological forces imposed upon the foetus (*fetus*)"(2). It was thought and accepted that the injury was due to the clinician applying traction (bending) to an infant's head and neck – and not endogenous force (maternal force caused by internal contractions and/or pushing). This continued to be the assumed mechanism of injury for many decades. Clinical observation raised questions about this assumption, starting in the early 1990s (1). These questions spurred research into the forces of labor and delivery. In 1991, the amount of force applied by a clinician in actual clinical deliveries was measured, and it was concluded that the typical clinically-applied traction in normal deliveries is around 47 N (3). While a higher force (100 N) was measured in one of the deliveries where a temporary NBPP occurred, the same amount of force had been applied in a delivery without any neonatal injury. Thus, this study could not explain why specific brachial plexus injuries occur. Clinical, experimental, and computational studies were initiated to better understand mechanisms of NBPP and address some of the key questions related to this injury, including: (1) How much force (endogenous and/or exogenous) is required to injure the brachial plexus?; (2) How much stress or strain in the brachial plexus is needed to result in injury

(Chapter 5,7,8)?; (3) How do different types of clinician-applied birthing maneuvers affect the stretch and forces applied on the brachial plexus?; and (4) How do different anatomical variations (size and angles) of the brachial plexus change the stress that develops within portions of the plexus **(Chapter 5)**?

In the field of NBPP research, experimental work on cadaveric infants and clinical deliveries is challenging due to ethical concerns. Different ways to analyze the brachial plexus can include cadaveric, animal, and computational models. Due to the importance of using living or immediately post-mortem nerves for biomechanical and physiological investigations, animal models are a common approach to studying nerves, including the brachial plexus. In the late 1980s, mechanical failure testing of the nerve complex was conducted on adult rabbits (4). Kawai *et al.* showed that traction to the plexus caused root avulsions in combination with post-ganglionic nerve trunk ruptures. It was shown that a rupture is most common in the C5 nerve root, while avulsions are most common in the C7 and C8 nerves followed by C6 and T1 nerves (4,5). In 2018, biomechanics testing was conducted on neonatal piglets to provide a detailed understanding of the biomechanical properties of the plexus (6). Segments of the brachial plexus were tested through tensile loading at two different rates (quasistatic and dynamic). Singh *et al.* provided insight into the biomechanical properties of neonatal piglet brachial plexus for three different brachial plexus segments and two different stretch rates **(Chapter 3)**. Computational modeling is another way to research complex nerve injuries and biomechanical responses. Computational modeling allows the development and analysis of anatomically accurate models of biological structures that in other ways could not be experimentally researched. Computational models, including Finite Element Modeling (FEM), have been around since the 1940's -- focusing mostly on solid and structural mechanics. In recent decades, FEM has been expanded toward addressing biomedical engineering questions, including those related to medical devices, biological structures, and biomechanical injuries.

To date, no two-dimensional or three-dimensional FEM of a neonatal brachial plexus has been published. The use of computational modeling allows the exploration and analysis of this nerve complex to investigate the effect of maternal and neonatal parameters on brachial plexus stretch during the birth process. The development of our simplified two-dimensional model of the spinal cord, roots, and trunks of the brachial plexus is the first step to provide the opportunity to more accurately assess the effect of the birth process on the stretch within the brachial plexus and the impact of biological variations in structure and properties on the risk of Neonatal Brachial Plexus Palsy **(Chapter 5)**. An anatomically accurate FEM will allow an in-depth analysis of NBPP injuries by providing a better understanding of stress distribution within the nerves. Furthermore, the model will provide knowledge of the progression of injury when force is applied. We anticipate our novel, three-dimensional neonatal brachial plexus model can be used to simulate and study specific brachial plexus injuries (Erb's Palsy, Klumpke's Palsy, etc.) to further investigate patterns of injury in NBPP **(Chapter 7,8)**.

Chapter 1: Brachial Plexus Anatomy and Physiology

Brachial Plexus Anatomy Introduction

The brachial plexus is a complex network of nerves that connects the spinal cord to terminal branches, which then provides the innervation of the full upper extremity. This set of nerves is made up of five different sections: roots, trunks, divisions, cords, and terminal branches **(Figure 1).** The roots are connected to the anterior rami of the spinal nerves C5 – T1. The roots divide into three trunks known as superior (C5/C6), middle (C7), and inferior (C8/T1). Each trunk is then divided into an anterior and posterior portion, with a total of six divisions. The divisions then proceed to connect to three cords -- lateral, posterior, and medial -- which connect distally to the nerve branches known as the musculocutaneous, axillary, medial, radial, and ulnar nerves. These terminal branches supply function to the anterior muscles of the upper arm, the forearm, and the intrinsic muscles of the hand (7).

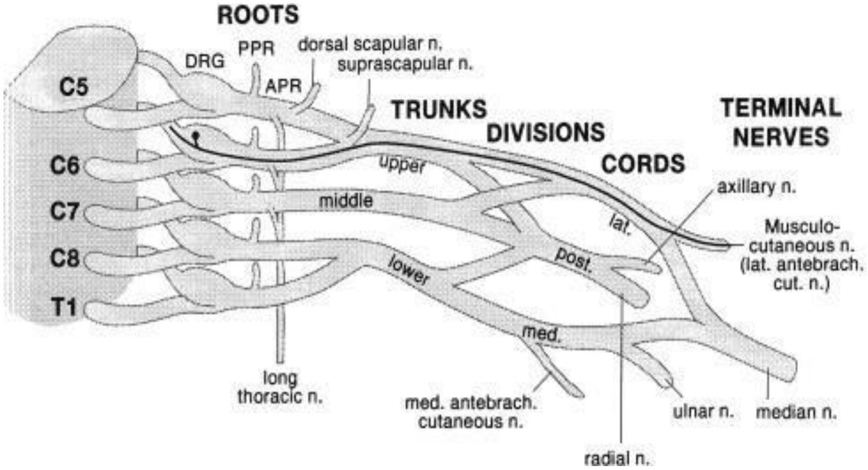

Figure 1: Brachial Plexus Anatomy Schematic (8).

Nerve Anatomy and Physiology

The severity and functional deficit of a brachial plexus injury depends on what nerve root and/or portion of the nerve is injured. The upper plexus is associated with the portion of nerves that control the upper arm, which if injured will cause a loss of mobility at the shoulder. If the middle (C7) and lower (C8/T1) portions of the plexus become injured, subsequently the forearm will be impacted by the injury. Brachial plexus injuries may include partial or total paralysis dependent on the location and severity of the injury.

Muscular Innervation

The musculocutaneous nerve stems from the lateral cord of the C5 and C6 nerve roots and gives function to the coracobrachialis, biceps brachii, and brachialis (9). The axillary nerve arises from the posterior cord and provides motor innervation to the deltoids and teres minor muscles (10). The median nerve innervates the muscles in the forearm, including the movement in one's wrists, thumbs, and fingers (excluding the fifth digit). The radial nerve originates from the medial cord of the C6 through C8 nerve roots and provides stimulation to the posterior forearm. The ulnar nerve continues from the C8 and T1 nerve roots and branches into the hand. This nerve innervates the palmaris brevis muscle and the fourth and fifth digits (11). Lastly, the interosseous nerve (dorsal interosseous nerve) is a continuation of the radial nerve that originates from the cervical nerve roots C7 and C8. This nerve supplies the function of the proximal posterior forearm, the wrist, and finger extensors. The nerves and associated nerve root innervations can be seen in **Table 1**.

Table 1: Nerve Innervations within Brachial Plexus Anatomy.

Upper Arm		Forearm	
Nerve	**Associated Nerve Roots**	**Nerve**	**Associated Nerve Roots**
Axillary Nerve	C5/C6	Median Nerve	C6/C7
Musculocutaneous Nerve	C5/C6	Anterior Interosseous Nerve	C7/C8
Radial Nerve	C6/C7/C8	Ulnar Nerve	C7/C8/T1
Posterior Interosseous Nerve	C6/C7/C8		

Anatomical Relationships

Within a spinal cord, there are 31 pairs of spinal nerves – 8 cervical pairs, 12 thoracic pairs, 5 lumbar pairs, 5 sacral pairs, and 1 coccygeal pair. In terms of anatomy, the brachial plexus is divided into 5 roots that come from the last 4 cervical nerves – C5, C6, C7, C8 – as well as the first thoracic nerve – T1. The nerve roots of C5 through C7 are supraclavicular (run above the clavicle), while C8 through T1 are retro clavicular and lie posterior to the 1st and 2nd ribs (1,12). The third section of the plexus, "cords," are distal to the clavicle. The posterior (middle) cord branches and travels under the neck of the scapula in transition to the axillary nerve. The remaining four nerve branches are centered around the axillary or brachial artery (13). The location of the brachial plexus can be seen in **Figure 2.**

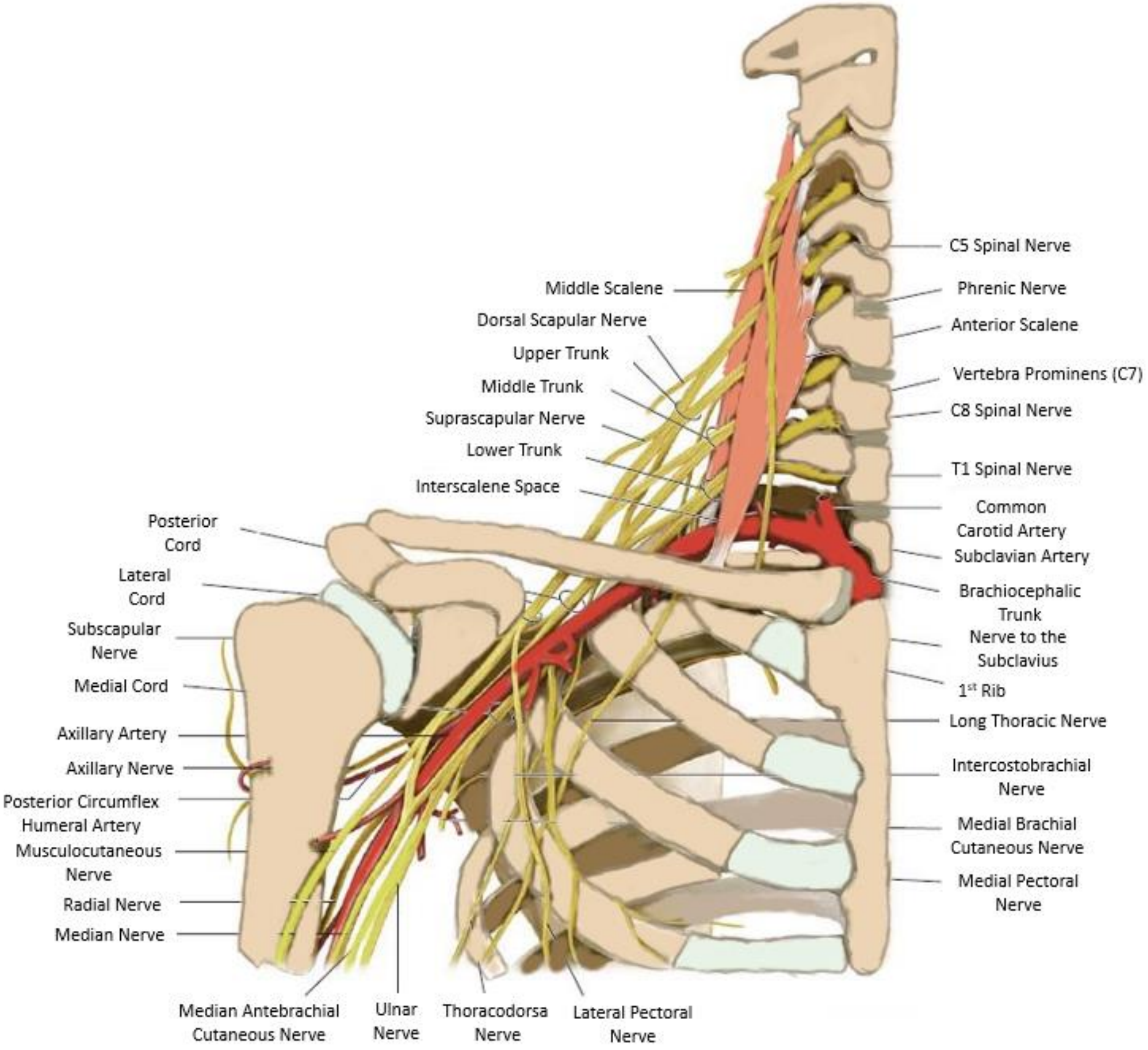

Figure 2: The structure of the brachial plexus in relation to muscles, arteries, and skeletal system. The brachial plexus runs from the cervical spine distally down the upper extremity (14).

Landmarks Surrounding the Brachial Plexus

The brachial plexus nerve roots stem from the foramen associated with the C5 – T1 vertebral bodies. In an article by Gilcrease-Garcia *et al.*, the following statement defines the main anatomy surrounding the brachial plexus – "A normal brachial plexus anatomy is assumed for five anatomic landmarks: the neural foramen, scalene triangle, lateral border of the first rib, medial border of the coracoid process, and lateral border of the pectoralis minor muscle"(13).

The neural (intervertebral) foramen is an opening between adjacent vertebrae through which the spinal nerve roots pass. Ventral and dorsal nerve roots exit the neural foramen laterally and merge to form the spinal nerves. The dorsal root ganglion (DRG) is located proximal to the union of the ventral and dorsal nerve roots (13). The DRG contains the cell bodies of sensory neurons that bring information from the periphery to the spinal cord (15).

The interscalene triangle is an anatomical landmark that can be used to locate a portion of the brachial plexus. The interscalene triangle is created by the anterior and middle scalene muscles. The spinous and transverse processes provide sites to which ligaments of the back and some muscles' tendons attach (16). The anterior scalene muscles begin from the C3-C6 vertebral processes. The middle scalene muscles begin from the C2-C6 processes. The subclavian artery ascends through the interscalene triangle. The upper (C5-C6) and middle (C7) nerve roots are superior to the artery, while the lower (C8-T1) nerve roots are posterior to the artery.

Distal from the nerve roots, the axons extend to form the three trunks. The trunks can be located anatomically at the lateral border of the middle scalene muscle **(Figure 3).** The lateral border of the first rib is the next landmark used to anatomically locate portions of the brachial plexus. Each trunk extends inferolateral to form anterior and posterior divisions. The six divisions are located near the lateral border of the first rib.

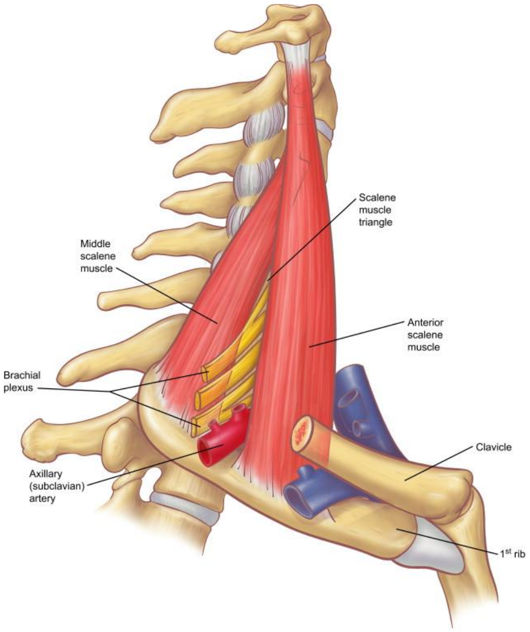

Figure 3: The interscalene muscle described as a landmark through which the roots of the brachial plexus and a portion of the subclavian artery pass (17).

The coracoid process is the next landmark used to anatomically locate portions of the brachial plexus. The coracoid process is a short, molded bone projecting from the shoulder blade – which the bicep attaches to. The posterior, medial, and lateral cords travel inferior to the coracoid process where they extend anteriorly from the divisions. The last well-known anatomic landmark is the lateral border of the pectoralis minor muscle, where the cords separate into the five terminal branches – musculocutaneous, median, axillary, radial, and ulnar (13).

Chapter 2: A Brief Discussion of Epidemiology and Pathomechanics of Neonatal Brachial Plexus Palsy

NBPP is estimated to occur in vaginal deliveries in 1-4 per 1,000 births and 0.3 per 1,000 cesarean deliveries (1,18–25). The most commonly used NBPP diagnostic scheme is known as the Narakas system of classification. There are four levels of brachial plexus injuries within this scheme **(Table 2).** Group I represents an injury of the upper plexus (C5/C6), while Group II represents an injury of the upper (C5/C6) and middle plexus (C7). Groups III and IV are applied to the diagnosis involving all five nerve roots, with Group IV including Horner Syndrome. Horner Syndrome, also known as oculosympathetic palsy, occurs due to nerve disruption on one side of the brain. This syndrome causes the patient to have symptoms that include a drooping eyelid, small pupils, and lack of sweating on that specific side of the face (26). In children who have sustained a brachial plexus injury, Horner Syndrome is associated with damage to the T1 nerve root.

Table 2: Narakas Classification of brachial plexus injury based on the number and level of nerve roots involved.

Groups	Affected nerve roots
I	C5, C6
II	C5, C6, C7
III	C5, C6, C7, C8, T1
IV	C5, C6, C7, C8, T1 + Horner Syndrome

Injury Mechanisms

Structural damage that results in persistent injury typically involves avulsion or rupture of the nerve root **(Figure 4).** An avulsion is defined as a disruption of the nerve root at its junction with the spinal cord, while a rupture occurs distal to the vertebral foramen. A neuroma (scar tissue) may develop in the region of the nerve root and consists of severe stretching and scarring of the nerve.

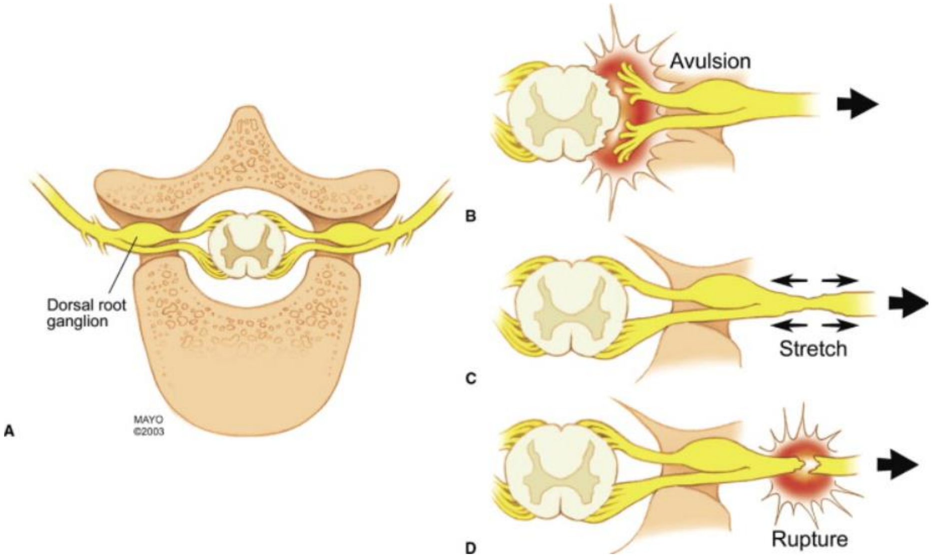

Figure 4: Nerve Injuries of the brachial plexus including avulsion and rupture (27).

During the birthing process, the mother can be positioned in many different ways by the birthing attendant, often depending on the mother's preference and the position of the baby within the uterus. **Figure 5** illustrates the mother laying in a supine position known as the lithotomy position. Within this position, the birthing attendant may assist with the birthing process in multiple ways, including using operative vaginal delivery tools (forceps or vacuum-assisted) and applying traction to the infant's head (1). The birthing attendant will assess the characteristics of the delivery and decide what intervention may be needed. This exogenous force from the birthing attendant combined with the endogenous force, generated by the uterine contractions, increases the intrabdominal pressure through pushing, thus the infant is then moved through the pelvis and birth canal. There is a chance that injury to the brachial plexus may occur to the infant either due to endogenous force only or with the added exogenous force as the birthing process progresses.

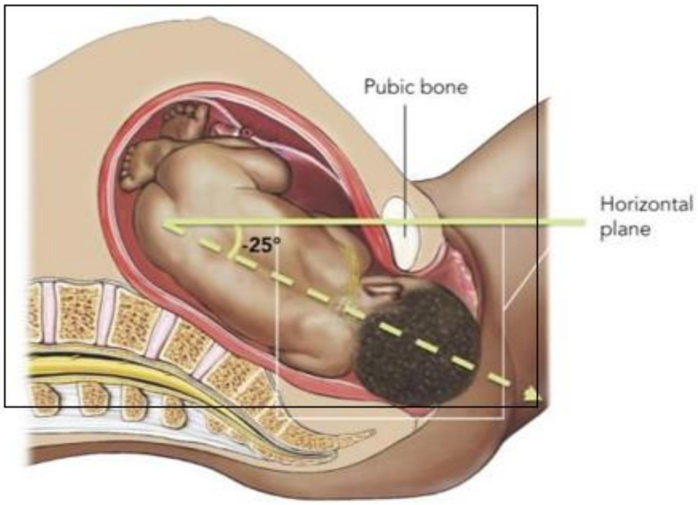

Figure 5: Schematic of infant within the uterus of a mother in labor lying in the lithotomy position (1). This image shows the orientation of the infant's spine (dotted line) and represents the end of the second stage of labor, when the head is crowning.

During the birthing process, there may be a point where the progression of the shoulders becomes stuck causing a widening of the angle between the infant's neck and shoulders – this is known as shoulder dystocia (SD) when it occurs to the anterior (upward facing) shoulder during vaginal cephalic delivery. Once the progression of delivery is stopped due to SD, stretch occurs to the brachial plexus due to both endogenous and exogenous forces. Compression of the brachial plexus may influence the occurrence of the injury - it may effectively shorten the nerve, increasing the strain in the proximal portion or may damage the epineurium at the location of the "pinch" and make it easier for the nerve to rupture.

Pathomechanics

Pathomechanics can be defined as the change in the normal biomechanical function of a joint, an extremity, or the torso as the result of trauma or disease (28). Trauma from a brachial plexus injury may be classified as permanent if the deficits persist for at least 12 months, in which case permanent changes in the biomechanical function of the upper extremity may occur. Thousands of brachial plexus injury combinations are plausible due to the complexity of the nerve's anatomy (1).

Functional and structural deficits may occur when brachial plexus injuries occur. If NBPP is suspected at or after birth, the site of the injury is documented in the neonatal physical exam, as well as the location of any bruising, the presence of a fractured clavicle, abnormal cord blood gas values, and the overall muscle tone of the neonate (1). **Table 3** explains the association of various nerve root injuries and their effect on the muscles of the upper extremity. As about 90% of NBPP resolve spontaneously, the extent of an NBPP is evaluated clinically around week four after birth to provide an assessment of whether surgical intervention is likely to be recommended.

Table 3: Paresis to muscles due to brachial plexus injury.

Affected Nerve Roots	Associated Muscles
C5, C6	Paresis of the deltoid and bicep muscle
C5, C6, C7	Paresis of the deltoid, bicep, and triceps muscle
C5, C6, C7, C8, and T1	Paralysis to the entire arm and the presence of Horner syndrome

Clinical presentation of NBPP injury differs depending on which nerve root or roots are injured. When Erb's Palsy is diagnosed, the patient will anatomically show an adducted arm, internally rotated shoulder, flexed wrist, and extended fingers. This anatomical classification is known as Waiter's tips deformity **(Figure 6).** When a patient presents with Waiters tips posture– the arm is unable to be raised from the side – this is due to the inability to flex the elbow. When Klumpke's palsy occurs (C8-T1), the patient will exhibit a flaccid hand with an active arm (29,30). A less common injury known as intermediate palsy (C7-T1 injury), presents within a patient showing an abducted arm, flexed elbow, and flaccid hands and otherwise active arm (31,32). When total plexus injury occurs to the patient, a total loss of function occurs to the upper extremity.

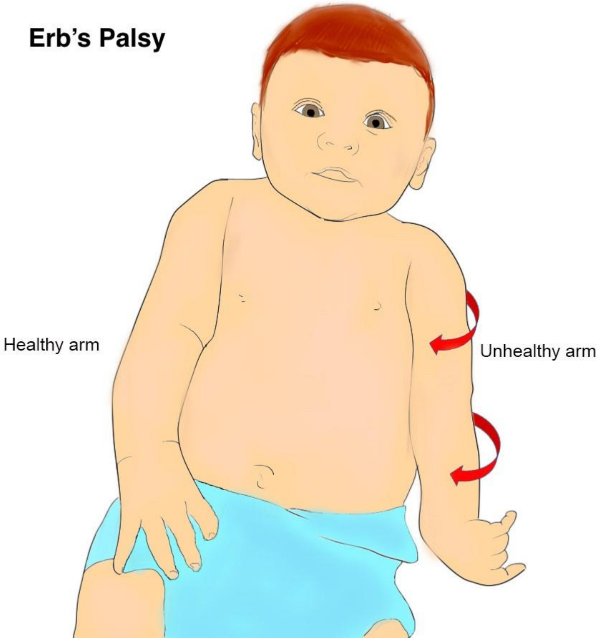

Figure 6: Erb's Palsy presents with a classical anatomical presentation known as Waiters tips deformity, with an adducted arm, internally rotated shoulder, flexed wrist, and extended fingers.

Management and Rehabilitation of Persistent of NBPP

In the United States, the rate of permanent injury, one that persists past 12 months of age, is reported to be between 8-33% of the overall occurrence of NBPP (33–40). The complexity of the injury determines the intervention needed for each individual. There is no single way to manage this injury – one can have surgical, therapeutic, or non-surgical treatments.

Surgical options include primary reconstructive surgery – which involves nerve graft repair, also known as nerve transfers. A nerve graft involves repairing a damaged nerve by connecting it with a new nerve transplanted from a separate part of the patient's body. **Figure 7** portrays the beginning of a nerve transfer process, in which the surgeon is conducting a reconstructive brachial plexus surgery on an infant patient.

Figure 7: The process of nerve grafting. In this instance, the surgeon is grafting the spinal accessory nerve to transfer and connect to a portion of injured nerve in the forearm. Image taken during primary reconstructive surgery at the University of Michigan.

Non-operative rehabilitation options include sensory stimuli and passive movements conducted by medical professionals and family members of the infant. Rehabilitation techniques may include electrostimulation, as well as immobilized splints used for the torso, head, and upper extremity to limit movement (41). Botulinum toxin injections can also be used between opposing muscles, such as the biceps and triceps, in order to reduce the impact of a contracture in some of the muscles of the upper extremity.

Conclusion

Biomechanical injuries of brachial plexus nerves can present differently among patients depending on the severity of the injury. The mechanism of injury – either endogenous or exogenous force – may play a part in the location and severity of the brachial plexus injury. To date, the amount of force needed to cause this injury is unknown. While this injury may not present outwardly immediately after birth, clinical presentation plays an important part in diagnosing this injury. Pathomechanics allows the functional and structural deficits of NBPP to be analyzed – allowing for management and rehabilitation techniques to be selected.

Chapter 3: Nerve Biomechanics and Currently Published Finite Element Models of Brachial Plexus’

Introduction to Biomechanics

Biomechanics is defined as the mechanics of biological tissues or the study of the mechanical laws relating to the movement or structure of living organisms. To date, limited research has been conducted on the biomechanical properties of human nerves – as nerves are nonhomogeneous in nature and are not generally considered to be a load bearing tissue (42–49). Current *in situ* analyses of animal nerves are being conducted to better understand their mechanical properties (50,51).

Anatomy and Biomechanics of Nerves

Nerves are complex structures composed of specialized cells called neurons. Neurons consist of various components, including the cell body (soma), dendrites, axons, and nerve fibers **(Figure 8.A).** Nerves are made up of axons (nerve fibers) and dendrites (branched extensions of a nerve cell). The axons are encased within a myelin sheath – a layer of fat and protein that surrounds the membrane **(Figure 8.B).** Nerves are made up of three layers of connective tissue known as the endoneurium, perineurium, and epineurium. The endoneurium is a layer that surrounds each axon; the perineurium surrounds groups of axons called fascicles; and the epineurium is a layer that covers the outer surface of the nerve (52).

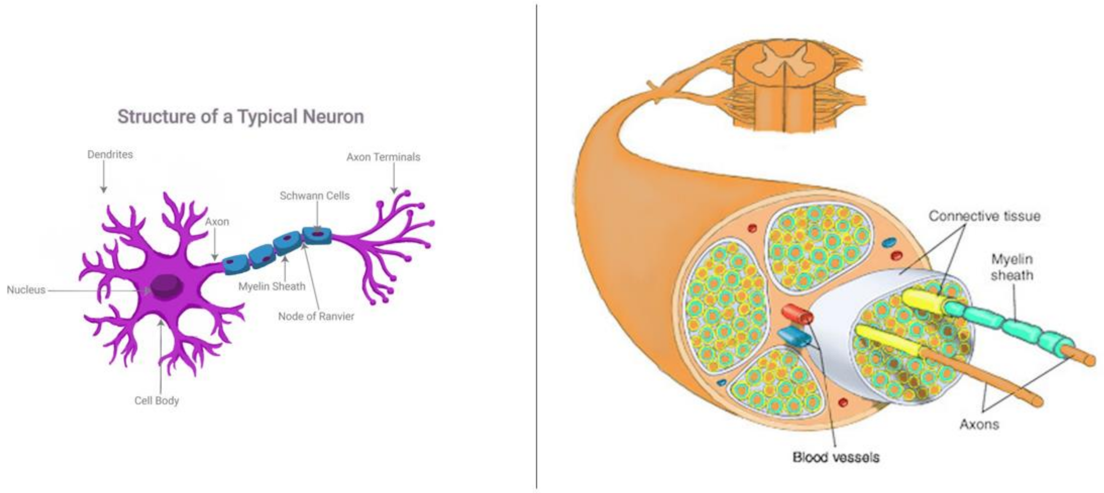

Figure 8: (A) Structure of a neuron; and (B) Structure of a nerve. The green connective tissue is the endoneurium, the white is the perineurium, and the yellow is the epineurium (14).

The biomechanics of nerves involves investigating the mechanical properties of these components, such as their elasticity, stiffness, and response to deformation or stretching. Since the 1980's, there has been a handful of research published reporting on the failure and mechanical responses from brachial plexus tissue (6,48,51,53–58). These tests were conducted on rabbits, piglets, and adult human cadaveric specimens. A search of the online database PubMed (National Library of Medicine) yielded no published articles that describe the mechanical properties of living and or fresh human neonatal brachial plexus tissue. One paper published in 1997 in Russia does provide properties for the phrenic (C3) and vagus (C4) nerves from fetuses (26 to 40-weeks' gestation) (59). However, the testing method did not account for potential slippage in the nerve during testing, which raises concerns about the accuracy of the ultimate strain and Young's modulus properties for those structures (60).

Biomechanics of Neonatal Brachial Plexus Palsy

Mechanical properties of human neonatal brachial plexi are currently unknown due to ethical issues surrounding conducting research on the vulnerable subject – infants. The biomechanics of NBPP involve studying the mechanical factors and forces (exogenous and endogenous) that contribute to causing the injury. NBPP occurs due to stretching of the nerves past their normal, elastic limit. Biomechanics plays a role in understanding the mechanisms of injury during childbirth, specifically, the mechanical forces that play a part during the birthing process.

The biomechanics of neonatal brachial plexus palsy involves investigating the mechanical factors contributing to nerve injury, studying the response of nerves to stretch and compression, understanding the regenerative process, and exploring the functional consequences of the condition. In our case, we are focusing specifically on understanding the effects of force and the nature of nerve stretching during the birthing process.

With respect to the development of our 2D and 3D computational models **(Chapter 5,7,8)**, our study used mechanical properties from Dr. Anita Singh from Temple University (6,51). Biomechanical analysis has been conducted on neonatal piglets – which represent a similar anatomical structure and material properties in relation to human neonates. Singh *et al.* used both the brachial plexus and tibial nerves from neonatal piglets to run tensile loading tests to analyze the effect of stretch rates on mechanical properties.

Singh *et al.* specifically researched two stretch rates (quasistatic and dynamic) via tensile tests conducted on neonatal piglets (6). The two cases, quasistatic and dynamic, had the following tension rates: 0.01-mm/second and 10-mm/second. 114 brachial plexus segments (roots/trunks, cords, and distal nerves) were collected from 3–5-day old piglets and tested through controlled stretch while monitoring the resulting load using a 200 N load cell. The experimental properties for the quasistatic and dynamic rates for the root/trunk segments can be seen in **Table 4**. During this research Singh *et al.* discovered that the maximum load, maximum stress, and Young's modulus values were significantly higher at the dynamic deformation rate in comparison to the quasistatic deformation rate.

Table 4: Experimental material properties of piglet brachial plexus segments (roots/trunks) for two tensile test cases: quasistatic and dynamic (6).

	Trunks		**Cords**		**Nerve Endings**	
	0.01 mm/s [n=32]	10 mm/s [n=25]	0.01 mm/s	10 mm/s	0.01 mm/s	10 mm/s
Youngs Modulus [MPa]	1.48 +/- 0.19	2.02 +/- 0.21	2.41 +/- 0.40	6.39 +/- 0.67	4.51 +/- 0.53	14.87 +/- 1.59
Maximum Stress [MPa]	0.20 +/- 0.02	0.45 +/- 0.04	0.46 +/- 0.02	1.31 +/- 0.08	0.98 +/- 0.10	3.51 +/- 0.44

Material Properties and Mechanical Response of Nerves

When developing and analyzing experimental properties measured in peripheral nerves, one must take into consideration the variations that occur within these heterogeneous structures, including (1) the difference in nerve root structure compared to more distal portions of the nerve, including the effect of differences in micro tissue layers between locations; (2) the nonlinearity of the mechanical response of nerves, similar to other biological tissues; and (3) the fact that material properties of nerve change with both age and death.

In 1950, Sunderland and Bradley accepted that a section of nerve packed with thick fibers would be weaker than one packed with fine fibers due to the way nerves increase in size proportionally as the fiber size increases (61). According to Rexed *et al.,* using human adult cadaveric specimens (14-87 years of age), it is known that posterior nerve roots are finer in comparison to anterior nerve roots (62). This supports the conclusion that posterior roots would be expected to be stronger than the anterior roots of the same spinal level.

The way in which nerve injury progresses in relation to applied tension to peripheral nerves is poorly understood in the world of science. Limited research has been conducted to analyze the limit of stretching that the nerve may undergo before a structural change occurs. When developing a computational model, it is not yet possible to model the micro-layers accurately, as the dimensions and material properties of these layers have not been characterized. While research has been conducted on peripheral nerves as one solid structure, excluding the micro-layers, these results are just the first step in understanding the stress-strain behavior and other biomechanical properties.

Nerves are described by nonlinear biomechanical response curves, as the nerves' behaviors are not always directly proportional to the magnitude of the input they receive. When it comes to computational modeling, it is difficult to conduct a nonlinear analysis for nerves due to the lack of published, nonlinear material properties for human nerves. Even with respect to the piglet data that has been published to date, only linear elastic properties are available.

Linear elastic material laws can be used to study the nerve's structural failure under load when it comes to computational modeling if the examined response focuses on stress rather than strain or deformation. Stress is defined as the ratio of the applied force to the initial cross–sectional area of an object ($Stress = \frac{Force}{Area}$). Nerves can be placed under a multitude of mechanical stresses including compressive, shear, and/or tensile stresses **(Figure 9).** Tensile stress can be applied longitudinally to the peripheral nerve creating an elongation of the nerve (an increase in strain) (44).

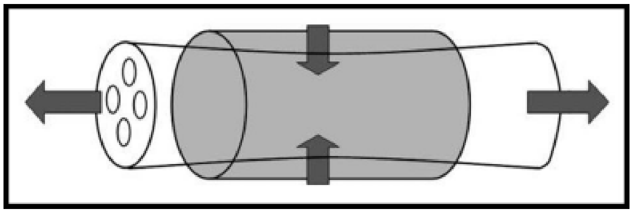

Figure 9: Tensile stress applied longitudinally to the nerves – increasing the strain. Simultaneously, transverse contraction occurs within the middle of the nerve that is experiencing a tensile stress at the two distal ends (44).

While studies have been conducted on adult cadaveric specimens, the results cannot be applied directly to a neonatal nerve as morphological changes occur to the peripheral nervous system (PNS) with age, including the fact that the myelination process continues from fetal development through about 5 years of age (63) and then deterioration of myelin sheaths (64). With advancing age, deterioration of the nerve can coincide with decreases in sensory nerve conduction velocity, amplitude of compound nerve action potentials, myelin thickness, and the number of large, myelinated fibers (64). In summary – the material properties within nerves change with age and adult nerves are not appropriate to use for a neonatal analysis.

Another significant hurdle to conducting a finite element analysis on nerves is the lack of material properties available due to the inability to run experimental tests on living nerves in human volunteers, whether adults or children. Changes in the material properties occur postmortem. Thus, cadaveric specimens, neonatal or adult, cannot be used as an accurate substitute for living subjects, as the organic matrix degradation that occurs after death will change the material properties within the nerves and other substructural properties.

Thus, for this study, a decision was made to use experimentally determined properties from the brachial plexus of piglets, as described above, these properties were used within the computational models as a surrogate due to the reasonable match for the modeled human tissue based on age (early myelination), anatomy (brachial plexus includes the same structures), and size. In addition, specimens have been tested immediately postmortem as well as *in vivo*, eliminating the problem associated with measurements on postmortem tissue.

Material Representation of Nerves

Nerve tissue is known to be nonlinearly viscoelastic and anisotropic with respect to its mechanical properties. However, the characterization of properties of nerves has actually been very limited – in part because nerves are not considered a load bearing tissue. Many of the FEM that exist for nerves, specifically the spinal cord and optic nerve, initially assumed that the material was linearly elastic and isotropic (65,66) – and this is a common assumption in early modeling of all biological tissues. The equilibrium equations governing the deformation of a linearly elastic, isotropic material are:

$$\frac{\partial \sigma_x}{\partial x} + \frac{\partial \tau_{xy}}{\partial y} + \frac{\partial \tau_{xz}}{\partial z} + b_x = 0$$

$$\frac{\partial \tau_{yx}}{\partial x} + \frac{\partial \sigma_y}{\partial y} + \frac{\partial \tau_{yz}}{\partial z} + b_y = 0$$

$$\frac{\partial \tau_{zx}}{\partial x} + \frac{\partial \tau_{zy}}{\partial y} + \frac{\partial \sigma_z}{\partial z} + b_z = 0$$

Where σ_i represents the normal stress perpendicular to a plane; τ_i are the shear stresses parallel to each plane and b_i epresents the components of the body force that is applied in each direction. Hooke's law then gives the following relationship between stress and strain in three dimensions for a linear elastic, isotropic material:

$$\begin{bmatrix} \sigma_x \\ \sigma_y \\ \sigma_z \\ \tau_{xy} \\ \tau_{yz} \\ \tau_{zx} \end{bmatrix} = \frac{E}{(1+v)(1-2v)} \begin{bmatrix} 1-v & v & v & 0 & 0 & 0 \\ v & 1-v & v & 0 & 0 & 0 \\ v & v & 1-v & 0 & 0 & 0 \\ 0 & 0 & 0 & \frac{1-2v}{2} & 0 & 0 \\ 0 & 0 & 0 & 0 & \frac{1-2v}{2} & 0 \\ 0 & 0 & 0 & 0 & 0 & \frac{1-2v}{2} \end{bmatrix} \begin{bmatrix} \epsilon_x \\ \epsilon_y \\ \epsilon_z \\ \gamma_{xy} \\ \gamma_{yz} \\ \gamma_{zx} \end{bmatrix}$$

where E is the Young's modulus and v is the Poisson's ratio.

For a 2D model, σ_z, τ_{zx}, and τ_{yz} would be removed from the matrix equation, along with their corresponding strains and Poisson's ratio components.

Published Finite Element Models of the Brachial Plexus

To date, only two adult brachial plexus models have been published (67,68). In an article written by Perruisseau-Carrier *et al.*, a 3D finite element model of an adult brachial plexus and the surrounding structures (vascular, nerve, muscular, and bone) was created **(Figure 10)**(68). This model was created using T1-weighted MRI scans (axial, sagittal, and coronal slices) of the brachial plexus and the following software: ITKSNAP, GMSH, and ABAQUS (Dassault Systèmes). The goal of their study was to determine which law of mechanical behavior was more appropriate for modeling the brachial plexus by comparing the results with Hooke's isotropic linear elastic law to those that used Ogden's isotropic hyperelastic law. The model was used to estimate the displacement of the nerve as the arm was moved to several angles of abduction, and this was compared to MRI-imaged positions of the nerve. The authors framed the work based on the goal of developing models for image-guided surgery. The main finding was that the deformation predicted from Hooke's law was less accurate in comparison to using Ogden's law. While segmentation and meshing of the entire plexus was achieved, the structure focused on the overall anatomy rather than the separation of the divisions, cords, and distal nerves.

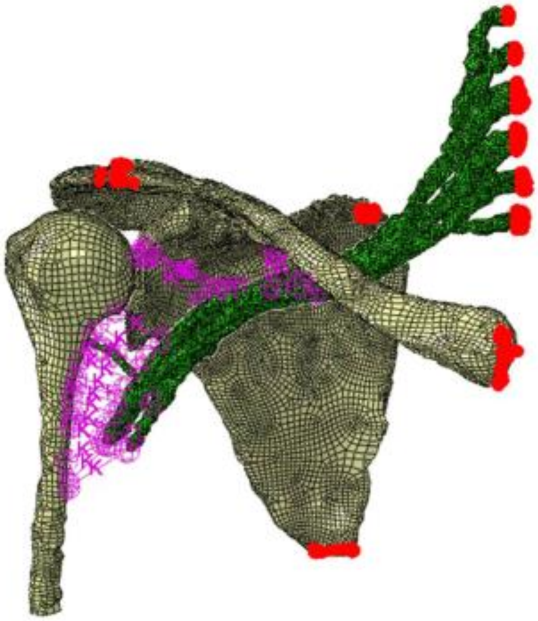

Figure 10: Three-dimensional computational model of the adult brachial plexus, soft tissue, and bone structures (68).

The second published adult brachial plexus model was developed from CT and MRI scans. This model was developed using Jvision (JSOL, Tokyo, Japan) and LS-Dyna (JSOL) software. The model consisted of the spine, dura mater, spinal nerve root, brachial plexus, thoracic cage, and upper limb **(Figure 11)**(67). The objective of this study was to validate the model and analyze patterns of injury by applying stress to portions of the model through different spinal motions. The results showed that a maximum value of strain of 21% occurred when the spine was retroflexed by 33 degrees. A limitation of the Mihara *et al*. model stemmed from the fact that it was not anatomically accurate, as the plexus was simply extended from the nerve roots to a length that corresponded to the complete anatomy, without including the complex structure of the divisions and cords of the plexus. This is due to the fact that a portion of the plexus was obstructed from view during the MRI scans due to the clavicle being anterior to the distal portions of the plexus.

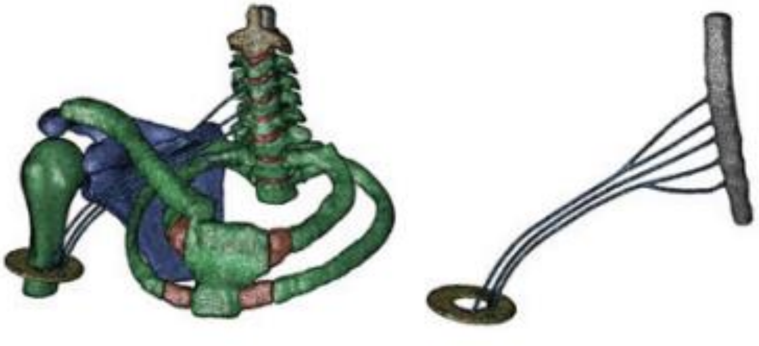

Figure 11: Three-dimensional model of the spine, dura mater, spinal nerve root, brachial plexus, thoracic cage, and upper limb (67).

Conclusion

To date, no neonatal brachial plexus finite element model has been published. This may be due to many different limitations that occur with the development of a neonatal model. First, no geometric properties of neonatal brachial plexus nerves are published due to the difficulty of conducting research on human neonatal cadavers and the challenge of collecting properties from images due to the interference of the clavicle. Second, as discussed above, characterization of the mechanical properties of the infant brachial plexus cannot be made directly from human specimens. In addition, no model of the human brachial plexus has been developed that includes the full complexity of the anatomy. These gaps in the literature provide the opportunity for this dissertation, in which both 2D and 3D models of the neonatal brachial plexus have been developed. **Chapter 5** begins the exploration and model development using a 2D model of the proximal plexus. **Chapter 7** explains the process of collecting neonatal and adult brachial plexus dimensions for this project. Lastly, **Chapters 5, 7, and 8** discuss the development process of creating the novel 2D and 3D neonatal brachial plexus model.

Chapter 4: Statistical Analysis of Maternal and Neonatal Variables Related to the Occurrence of Permanent Neonatal Brachial Plexus Injuries

Previous research on cadaveric specimens determined that ruptures typically occur in the upper plexus (C5 and C6) and avulsions occur in the lower plexus (C8 and T1) (69). These statistical patterns of injury have not been examined in clinical cases. The main objective of this chapter is to use a database of clinical cases to analyze the maternal, neonatal, and delivery factors that are related to the occurrence of patterns of avulsions and ruptures, as these may lend insight into factors that increase the risk of these injuries. The second objective is to analyze the statistical frequency of occurrence of avulsions and ruptures in each nerve root. The clinical patterns of injury will be used as one source of validation for the finite element models of the neonatal brachial plexus **(Chapters 7 and 8)**.

Introduction to Statistical Analysis

Statistical analysis of the patterns of brachial plexus injuries in infants has rarely occurred in recent decades. This may be due to the ethical concerns that surround undertaking exploratory surgery in infants. It is also complicated by the fact that neurosurgeons typically do not have access to the labor and delivery records of the mother, as she is not their patient. The University of Michigan has attempted to bridge this gap in knowledge through a study that included both members of the Brachial Plexus Palsy Program and an obstetrician. Neurosurgery and allied health professionals (e.g., physical, and occupational therapists) assessed the function and outcomes in each child, while an obstetrician reviewed each maternal chart, which had been accessed through an IRB-approved process. The University of Michigan Neurosurgery team provided the de-identified data to our research group to perform further statistical analyses. Data included maternal, neonatal, and delivery variables collected during the pregnancy **(Appendix Table 32)**, and they included both binary and numerical data. The goal of this portion of the project is to use analyze the data collected for the many different parameters and see if they can be used to tell before birth if the infant might be more susceptible to brachial plexus injuries and whether the pattern of injury (upper trunk ruptures and lower trunk avulsions) seen in cadaveric studies carries over to clinical cases.

Statistical Methodology

A retrospective study of patients was conducted based on data collected from the University of Michigan’s brachial plexus program. Maternal and neonatal data was collected from patients seen from the years 2014 to 2018. In all, 103 patients were seen by the clinic during that time, 28 of whom underwent a neurosurgical procedure. During primary reconstructive surgery, the status of each nerve root was documented by the surgeon, Dr. Lynda Yang. The maternal and neonatal medical records for the entire population of 103 patients were also evaluated by Dr. Suneet Chauhan, an obstetrician, for key perinatal and neonatal parameters.

As stated previously, the three sections of the brachial plexus include the upper (C5/C6), middle (C7), and lower (C8/T1). During primary reconstructive surgery, the C5 – T1 nerve roots were analyzed visually by medical professionals through from the University of Michigan Neurosurgery department and classified based on one of the five criteria: rupture, avulsion, not determined, surgically could not look, and normal. Using the data of the 28 patients who underwent primary reconstruction and the criteria listed, six groups were created. The groups were assigned based on the location of the injury and the structural severity, defined based on the occurrence and location of any nerve root avulsions. The number of patients and description of each group can be seen in **Table 5**.

Table 5: Six injury groups defined based on the occurrence and location of any nerve root avulsions study.

Group	Group Abbreviation	Injury Criteria	Number of patients
1	UMNA	Upper/mid plexus with no avulsion	8
2	UMA	Upper/mid plexus with avulsion	5
3	PNA	Pan plexus with no avulsion	3
4	PLA	Pan plexus with lower avulsion	7
5	PUA	Pan plexus with upper avulsion	2
6	PULA	Pan plexus with upper and lower avulsion	3

Group 1 was defined as having an upper and middle plexus injury with no avulsion. This means C5, C6, and/or C7 were ruptured and C8/T1 were normal (non-injured). Group 2 was defined as the upper and middle plexus with avulsion, in which the upper and middle plexus had at least one avulsion of the nerve roots. Groups 3-6 were defined as pan plexus injuries, which occur when all levels of the nerves and trunks are damaged. Group 3 was defined as pan plexus with no avulsion, in which all levels of the plexus had ruptured. Group 4 was defined as pan plexus with lower avulsion, in which C5-C7 was ruptured while C8 and/or T1 were avulsed. Group 5 was defined as pan plexus with upper root avulsions, in which C5 or C6 was avulsed and at least one of C8 and T1 was ruptured. Lastly, Group 6 was defined as pan plexus with at least one nerve root from both the upper and lower plexus avulsed.

Data Collection

It was not possible to analyze statistically every variable collected due to either a lack of data – in many medical records the pertinent information was not documented – or insufficient variation within the patients to allow for a statistical pattern to be identified (low power). Thus, only 28 patients and their data were used in this statistical analysis. The subset of maternal and neonatal parameters collected from the antenatal medical records for the 28 patients can be seen in Table 5. The parameters that were analyzed included both binary (yes/no) and numerical variables. The full set of data for the 28 subjects can be seen in Appendix **(Table 32)**.

The definition of most of the variables is straightforward. Those that may require additional explanation are:

- Gravidas: The number of times a female has been pregnant (e.g., Nulligravida = never pregnant; primigravida = first-time pregnant; multigravida = many pregnancies)
- Paraterm: The number of pregnancies delivered after 20 weeks of gestation. This number includes all births beyond 20 weeks of gestation whether or not the baby was born alive (70).
- Apgar Score: The Apgar score comes from an evaluation that occurs 1 minute and 5 minutes after birth. The Apgar test measures the baby’s appearance, pulse, grimace, activity, and respiration (71). The test can be scored from 0 to 10 points, with 0 to 2 points per category. A score of 7 points or above is considered a healthy baby with no need for immediate medical care.

Table 6: Maternal and Neonatal Variables Analyzed within SAS Software.

Maternal Variables	Neonatal Variables
Gravidas	Apgar Score (1 minute and 5 minute)
Maternal Age	Birthweight
Maternal body mass index (BMI)	Head Circumference
Weeks' Gestation	Neonatal Length
Paraterm	

Statistical Analysis Tests

Statistical analysis is an important part of neonatal brachial plexus research as it may lend insight into determining which factors are likely to correspond to an increased risk of NBPP. Statistical Analysis Systems (SAS) Studio software was used to run statistical analysis tests. The statistical analysis test process can be seen in **Figure 12**.

The first step of the statistical analysis was to run a Power Analysis: One-Way Analysis of Variance (ANOVA) for each variable. Statistical power is conducted to determine if the number of subjects available for each test is sufficient to conduct further statistical evaluation. A power value of 0.8 or above is considered adequate to most statistical professionals to conclude the study has enough power to continue analysis.

A Shapiro-Wilks test was then conducted to assess the normality of the dataset. When conducting this analysis, the null hypothesis was that the distribution of the sample was normal. If the p-value is below the alpha value of 0.05, the null hypothesis was rejected, and concluded the sample was not normally distributed. Thus, if the value was greater than 0.05, one will fail to reject the null hypothesis -- and it was appropriate to show the sample as normally distributed. A Q-Q plot can be used to visualize the normality of the data set. If the data is normally distributed, the Q-Q plot will show a straight diagonal line with the datapoints.

If the Shapiro-Wilks test showed a normal distribution, the next statistical test conducted was the Levene's test to check for homogeneity (of variance). For the variance between groups to be homogenous, the range for the dependent variable must be equal within all groups. A null hypothesis is used to allow one to assess the validity of the observed results. The null hypothesis for this analysis is described as "the groups we are comparing all have equal variances." If the p-value was less than 0.05, the null hypothesis was rejected, and the variables variances were not equal – thus the next step was to run a Welch ANOVA test. If the p-value for the Levene's test was greater than 0.05, one would fail to reject the null hypothesis and would conclude that there was equal variance between the groups.

After normality and equal variances assumptions were confirmed, a one-way ANOVA test was conducted. A One-Way ANOVA test was conducted to compare the means of a selected variable between the six groups within this dataset. If the p-value was less than the significance level value of 0.05, then one could reject the null hypothesis and conclude that at least one of the population means was different from the others. Rejecting the null hypothesis indicated that at least one of the group's means was different – however it did not identify which of the six groups had a statistically different mean. A Tukey Post-Hoc test was conducted next to determine which specific group and/or groups were different. A Tukey post-hoc test specifically makes pairwise comparisons between group means.

If the Levene's test showed a p-value less than 0.05, the null hypothesis was rejected, and the parameter's variances were not equal – thus the next step was to run a Welch ANOVA test. A Welch ANOVA test can be used even if the data violated the assumption of homogeneity and is an alternative to the customary one-way ANOVA test. A Welch test is used to assess the mean value of three or more groups. If the p-value is less than 0.05 one can conclude that the means of all groups are not equal. To identify significant differences between the groups, the Tukey Post-Hoc test can be conducted. If the p-value for the Welch test was greater than 0.05, one can conclude the means of the group are equal and no further tests are required.

Returning to an earlier decision point in the process, if the sample was not normally distributed (by rejecting the null hypothesis of the Shapiro Wilkes test), a Chi-square test was conducted to determine if the distribution of one categorical variable was similar or different in comparison to a second categorical variable. When running this analysis, if the p-value is less than 0.05 there is enough evidence to reject the null hypothesis and conclude, in our case, that this is enough evidence from the sample to show that there is a significant difference in the distribution of the specific variable tested between the six groups.

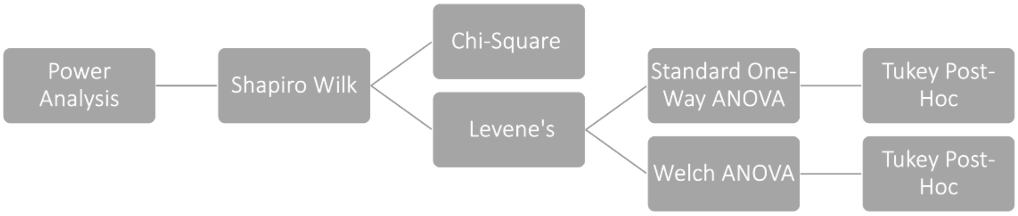

Figure 12: Decision tree illustrating the process of statistical analysis tests conducted comparing the injury groups to each other.

In addition to comparing the six injury groups with each other, we had the opportunity to determine how the parameters that characterized our injured population compared to those values within a large, general population. This was done for the seven numerical variables using a one-sample t-test to determine whether the mean of the data significantly differed from the United States' mean for that specific variable. If the p-value is less than 0.05 the null hypothesis is rejected, and one can conclude we have sufficient evidence that the specific variable is significantly different then the United States mean value of that variable **(Table 11).**

Finally, a frequency of occurrence test was conducted to analyze the occurrence of avulsions and rupture in each nerve root among all 28 patients. The percentage of the infants who had experienced a rupture or avulsion of each of the nerve roots of the brachial plexus is provided in **Table 12.**

Statistical Results

Statistics Summary

Table 6 displays the summary of statistics for each of the variables analyzed within this chapter. The mean and standard deviation was calculated for each. **Figure 13** visually shows histograms for each variable overlaid with normal density curves. A histogram provides a visual representation of the distribution of data. In addition, the normal density curve overlaying each graph visual shows where the mean of the distribution is located.

Table 7: Summary of maternal and fetal parameters, including mean and standard deviation of each group.

		Group 1	**Group 2**	**Group 3**	**Group 4**	**Group 5**	**Group 6**
Gravidas	Mean	4.50	3.60	1.70	3.40	8.50	2.30
	Stdev.	4.34	1.51	1.15	2.64	4.95	1.52
Maternal Age $[\boldsymbol{years}]$	Mean	28.10	28.80	23.30	30.00	32.00	22.00
	Stdev.	5.44	5.07	3.51	7.67	9.90	3.60
Maternal BMI $[\boldsymbol{kg/m^2}]$	Mean	37.60	NA	40.00	45.10	NA	36.00
	Stdev.	9.61	NA	NA	0.07	NA	NA
Weeks' Gestation	Mean	37.80	39.00	38.70	39.00	39.50	39.00
	Stdev.	1.00	1.00	1.50	1.60	0.70	0.00
Paraterm	Mean	2.30	1.60	1.00	1.70	2.50	2.00
	Stdev.	2.40	1.30	NA	1.20	2.10	1.40
Birthweight $[\boldsymbol{kg}]$	Mean	4.10	4.50	3.90	4.00	3.60	4.30
	Stdev.	0.50	0.20	0.30	0.70	NA	0.20

Table 7 (cont'd)

Head Circumference [cm]	Mean	34.70	36.60	NA	34.00	33.70	25.00
	Stdev.	1.20	0.80	NA	2.60	NA	NA
Neonatal Height Length [cm]	Mean	52.50	54.30	54.00	54.20	54.80	55.00
	Stdev.	3.00	2.50	NA	3.20	0.30	NA
Apgar [1 min]	Mean	4.80	5.40	4.30	3.40	5.00	1.70
	Stdev.	3.00	1.50	2.10	2.00	1.40	1.20

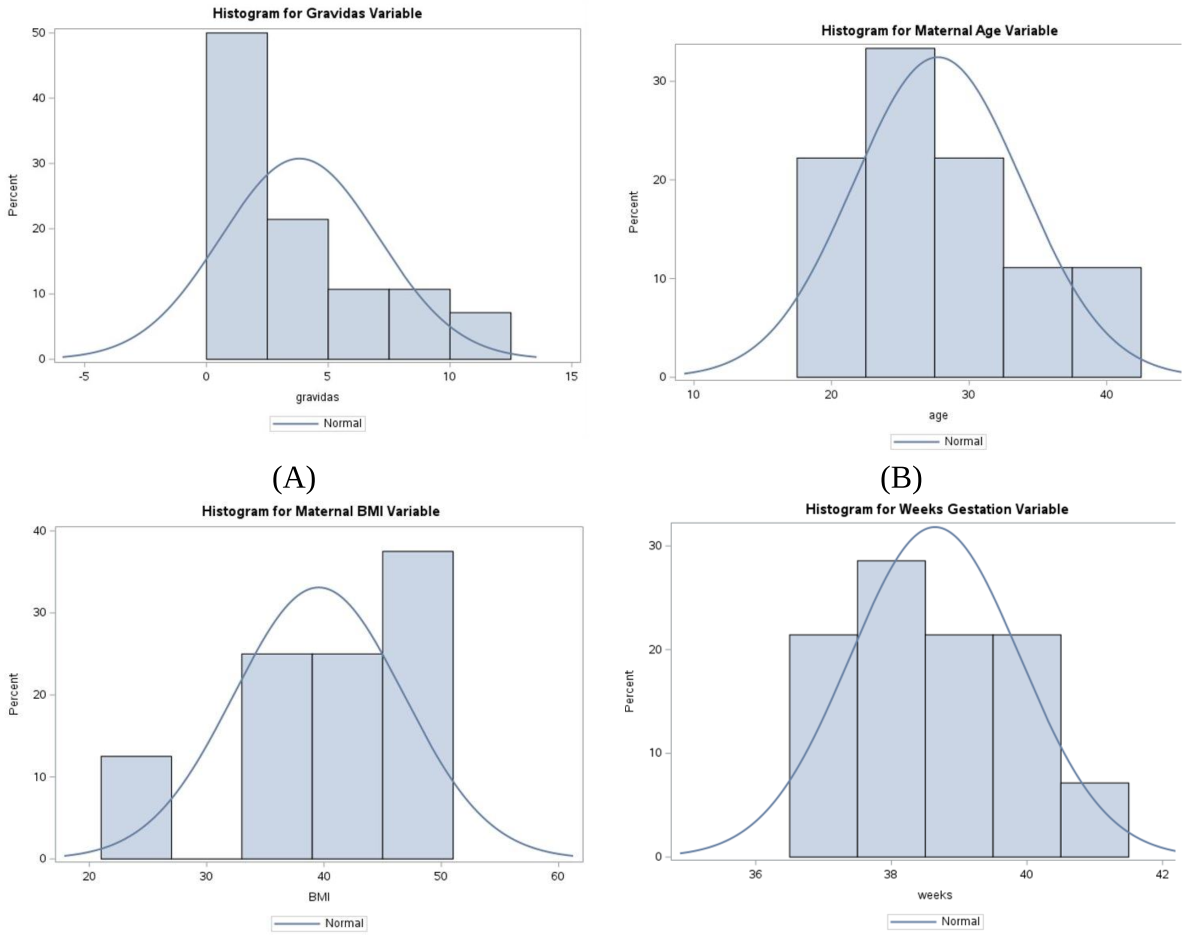

(A) (B)

(C) (D)

Figure 13: Histogram for the variable with overlaid normal density curve for the mean (cm). The variables are as follows (A) Gravidas; (B) Maternal Age; (C) Maternal BMI; (D) Gestation; (E) Paraterm; (F) Neonatal Weight; (G) Head Circumference; and (H) Neonatal Length.

Figure 13 (cont'd)

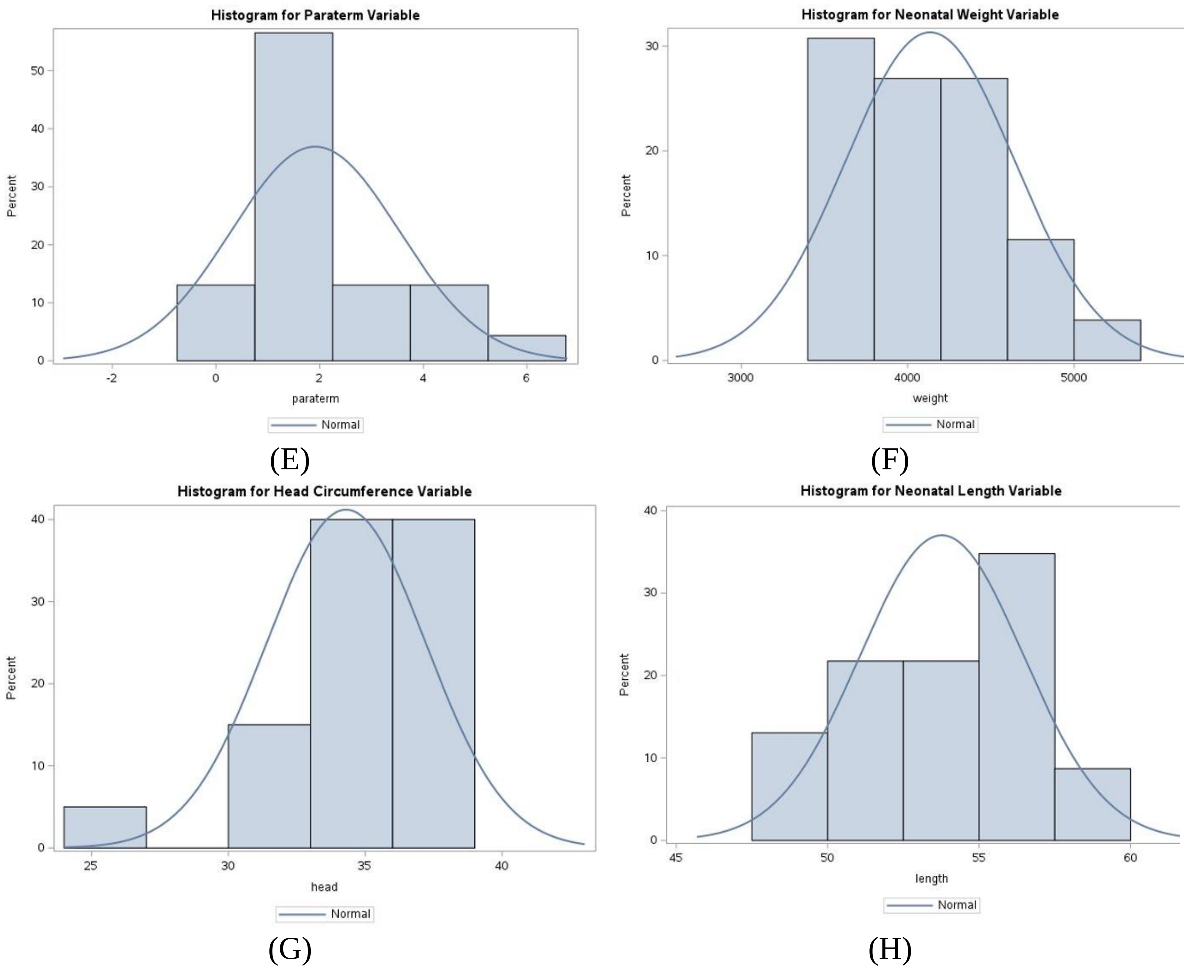

Histogram for Paraterm Variable

Histogram for Neonatal Weight Variable

(E) (F)

Histogram for Head Circumference Variable

Histogram for Neonatal Length Variable

(G) (H)

Comparison Between Injury Groups

The post-collection power analysis indicated that there were insufficient data to reliably investigate the between group differences between the Apgar score, maternal age, and maternal BMI. However, those variables were compared to the national population data, as described in the next section.

Six parameters were analyzed through the statistical test process shown in **Figure 12**. These parameters went through analysis to determine if there is a significant difference in the variable within the six injury groups defined in **Table 5**.

Table 8: Statistical results for numerical maternal and neonatal variables.

	Statistical Analysis Test			
Variable	**Shapiro – Wilk (Normal Distribution)**	**Levene's (Equal Variance)**	**Welch ANOVA**	**One-Way ANOVA**
Neonatal Weight	> 0.05	0.0974	-	0.4574
Head Circumference	> 0.05	0.0011	0.0153	-
Neonatal Length	>0.05	0.7696	-	0.8328
Gestational Weeks	< 0.05	-	-	-
Gravidas	< 0.05	-	-	-
Paraterm	< 0.05	-	-	-

Table 8 shows the results of statistical tests conducted on neonatal and material NBPP variables. When examining neonatal weight, head circumference, and neonatal length data through the Shapiro-Wilks test, we concluded that the data is normally distributed. Continuing the analysis to the Levene's test, we can conclude that the variances are equal for the neonatal weight and length variables, but that there is unequal variance for the head circumference data ($p < 0.05$). Lastly, we can conclude there is no significant difference between the neonatal weight and neonatal length between the six groups. However, in the case of head circumference, we were able to conclude there is significant difference between at least one of the groups. A Tukey-Kramer post-hoc test was conducted to decide which group or groups were significantly different from each other **(Table 9).**

Table 9: Statistical results for Tukey-Kramer post-hoc test.

Differences of Groups Least Squares Means Adjustment for Multiple Comparisons: Tukey-Kramer	
Variables	**Significant differences between groups**
Head Circumference	1v2,1v5,1v6,2v4,2v5,2v6,4v6,5v6

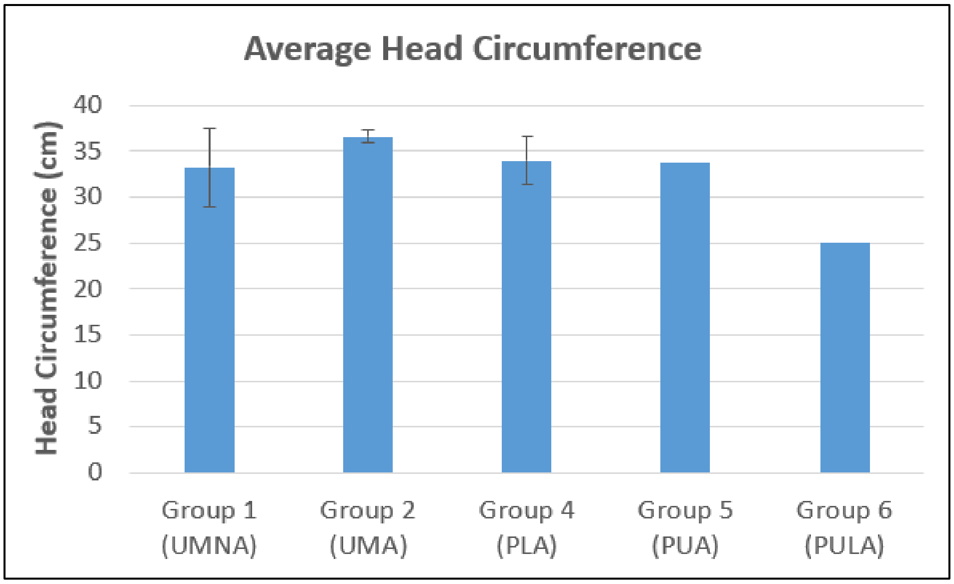

Figure 14: Mean head circumference for the groups, excluding group 3 due to lack of data collected. Error bars represent standard deviation. Group 1 = Upper/mid plexus with no avulsion; group 2 = upper/mid plexus with avulsion; group 3 = pan plexus with no avulsion; group 4 = pan plexus with lower avulsion; group 5 = pan plexus with upper avulsion; and group 6 = pan plexus with upper and lower avulsion.

The mean values for the head circumference for each group are provided in **Figure 14**. In summary, Group 6 had a statistically different head circumference when compared to groups 1, 2, 4, and 5, while group 5 had a statistically different head circumference from groups 1 and 2. Groups 2 and 4 were also statistically different from each other.

Of the three variables that were not normally distributed – gestation, gravidas and paraterm – we can conclude through the Chi-Square test that there is not a significant statistical difference for those variables between the six groups – as the alpha value was greater than 0.05 **(Table 10).**

Table 10: Statistical results for Chi-square probability test.

	Chi-Square (X^2) Probability Value Results	
Variables	**Test Statistic Value**	**Chi-Square Probability**
Gestation	25.6797	0.0623
Gravidas	42.9460	0.1674
Paraterm	25.6797	0.6914

One Sample T-Test Analysis

A one sample t-test was conducted to identify any significant difference for each numerical parameter within the entire study population (infant sustained a permanent brachial plexus injury and underwent surgery) in comparison to the United States' mean. The results of these t-tests are shown in **Table 11** including the degrees of freedom, group mean, U.S mean, and p-value. The degrees of freedom indicate the number of independent values for each parameter analyzed – this value shows that some variables had limited values collected in comparison to others. In comparison to the U.S mean, there was a significant difference in the following variables: Apgar at 1 minute (lower), weeks of gestation (lower), birthweight (higher), head circumference (higher), and mother's BMI (higher).

Table 11: Statistical results of one sample t-test analysis.

Variable	Degrees of Freedom	Group Mean	U.S Mean	p-value
APGAR Score (1 min)	27	4.18	7	<0.001
Neonatal Weight (g)	25	4134.5	3250	<0.001
Head Circumference (cm)	19	34.3	33.9	0.0487
Gestational Weeks	27	38.6	40	<0.001
Maternal BMI	6	40	24	0.0014
Neonatal Length (cm)	22	53.7	54.2	0.4473
Maternal Age (years)	26	27.7	26.3	0.8283

Note: *United States mean values were collected from various sources* (72–75). *Reference 70 was used for average neonatal weight, head circumference, and length; reference 71 was used for average maternal age; and reference 72 was used for average gestational weeks. Reference 73 was used for average maternal BMI.*

Frequency of Occurrence of Avulsions versus Ruptures

Among the 28 neonates with NBPP who underwent surgery during the study period, the C5 through T1 nerve roots were assessed to categorize each nerve root as one of the following: rupture, avulsion, not determined, did not look at, and normal. The percentage of the infants who had experienced a rupture or avulsion of each of the nerve roots of the brachial plexus is provided in **Table 10** and **Figure 15**.

Table 12: Frequency of occurrence of ruptures and avulsions throughout the brachial plexus among 28 infants who underwent surgical treatment for NBPP.

		Frequency	Percent
C5	Rupture	25	89.3
	Avulsion	3	10.7
C6	Rupture	18	64.3
	Avulsion	10	35.7
C7	Rupture	17	60.7
	Avulsion	8	28.6
C8	Rupture	8	28.6
	Avulsion	7	25
T1	Rupture	10	35.7
	Avulsion	2	7.1

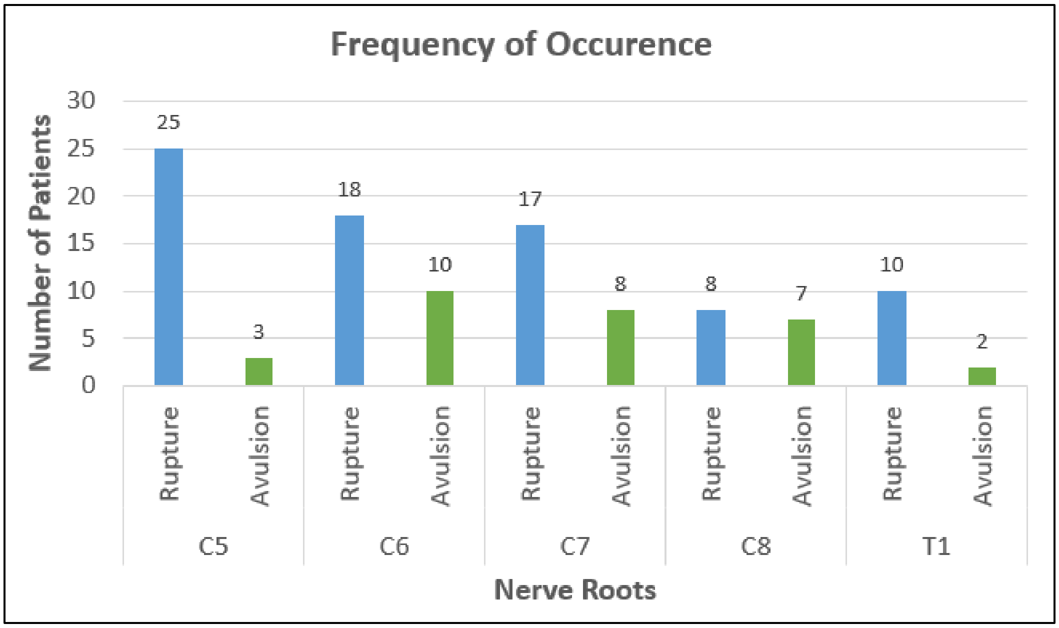

Figure 15: Frequency of occurrence of ruptures and avulsions throughout the brachial plexus within 28 infants who underwent surgical treatment for NBPP.

Research on 9 neonatal cadavers previously found that failure of the C5 and C6 nerve roots primarily occurred through rupture, while failure of C8 and T1 was dominated by avulsions (67). The current analysis confirmed the Metaizeau *et al*. findings that the failure to the lower plexus is preceded by failure of the upper plexus (i.e., all 28 subjects experienced failure of the upper plexus, while only a subset saw failure in C7, C8, and/or T1). The 28 subjects within this set of data demonstrated a much greater rate of ruptures in the lower plexus than was seen in the experimental cadaveric study. This finding has translational significance, as whether a rupture or avulsion is present alters the surgical strategy of nerve reconstruction. Interestingly, C6 had the highest number of avulsions out of the 28 neonates – even though it was still at a lower rate than the ruptures at that level.

Conclusion

The main objective of this chapter was to use a database of clinical cases to analyze the maternal, neonatal, and delivery factors associated with a population of infants who sustained a permanent NBPP injury, as these may lend insight into variables that increase the risk of these neonatal brachial plexus injuries. Using SAS software – through the Tukey-Kramer test – we concluded that only head circumference showed a significant difference between the six groups. Head circumference may impact which portion of the plexus may become injured – as a larger head circumference may correlate to a larger neonate in general (weight, length, shoulder width).

The increase in body size may cause a need for extra applied force that may include forceps, vacuum, and increased maternal pushing, and it may increase the risk of bending of the neck when a shoulder dystocia occurs. This will be an interesting variable to investigate through computational modeling of the effect of the birth process on the brachial plexus in the future.

In comparison to the United States mean through the one-sample t-test, there was a significant difference in the following variables: 1-minute APGAR (lower), weeks of gestation (lower), birthweight (higher), head circumference (higher), and mothers BMI (higher). These significant results are the first step in discussing the possibility of external variables playing a part in neonatal brachial plexus injuries. The numerical neonatal variables (birthweight, and head circumference) may be investigated through computational modeling of the effect of the birth process on the brachial plexus in the future. Currently, we can associate that a higher birthweight may cause the need for additional force, either exogenous or endogenous, to progress the birthing process. This additional force may be the cause of the injury to the plexus. Furthermore, an increase in birthweight is correlated with a higher chance of shoulder dystocia occurring (76). Most brachial plexus injuries occur in infants that have no currently identifiable risk factors for the baby or the mother; however, the occurrence of shoulder dystocia increases the risk of brachial plexus injury 100-fold compared to deliveries without a shoulder dystocia (76). The incidence of brachial plexus injuries after shoulder dystocia varies from 4% to 40% (77).

It has been published in the literature that maternal weight gain is associated with larger infant birth weight (75). As larger infants have a higher, though still low, risk of shoulder dystocia, and shoulder dystocia results in a significant increase in risk of NBPP, the fact that both maternal weight and the infant's birth weight are higher within the group of surgically treated infants than the US mean is not surprising. This is the first study in which the association of the actual pattern of injury – rather than simply the occurrence of a temporary or permanent injury (78) – with maternal and infant factors has been investigated. Expanding the population of infants for whom the full scope of maternal and perinatal data is available will add power to the analysis and the insight that we can gain. The clinical patterns of injury observed in this study population will be used as one source of validation for the three-dimensional finite element model of the neonatal brachial plexus **(Chapter 7).**

Chapter 5: Investigating the Effect of Anatomical Variations in the Response of the Neonatal Brachial Plexus to Applied Force: Use of a Two-Dimensional Finite Element Model

This chapter was submitted for publication to the journal PLOS-One on August 21,2023. The revised paper, included here, was submitted on October 25, 2023. The formatting was changed to fit this dissertation formatting requirements and all reference citations refer to the bibliography at the end of the dissertation.

Abstract

The brachial plexus is a set of nerves that innervate the upper extremity and may become injured during the birthing process through an injury known as Neonatal Brachial Plexus Palsy. Studying the mechanisms of these injuries on infant cadavers is challenging due to the justifiable sensitivity surrounding testing. Thus, these specimens are generally unavailable to be used to investigate variations in brachial plexus injury mechanisms. Finite Element Models are an alternative way to investigate the response of the neonatal brachial plexus to loading. Finite Element Models allow a virtual representation of the neonatal brachial plexus to be developed and analyzed with dimensions and mechanical properties determined from experimental studies. Using ABAQUS software, a two-dimensional brachial plexus model was created to analyze how stresses and strains develop within the brachial plexus. The main objectives of this study were (1) to develop a model of the brachial plexus and validate it against previous literature, and (2) to analyze the effect of stress on the nerve roots based on variations in the angles between the nerve roots and the spinal cord. The predicted stress for C5 and C6 was calculated as 0.246 MPa and 0.250 MPa, respectively. C5 and C6 nerve roots experience the highest stress and the largest displacement in comparison to the lower nerve roots, which correlates with clinical patterns of injury. Even small (+/- 3 and 6 degrees) variations in nerve root angle significantly impacted the stress at the proximal nerve root. This model is the first step towards developing a complete three-dimensional model of the neonatal brachial plexus to provide the opportunity to more accurately assess the effect of the birth process on the stretch within the brachial plexus and the impact of biological variations in structure and properties on the risk of Neonatal Brachial Plexus Palsy.

Introduction

Neonatal brachial plexus palsy (NBPP) occurs during the birthing process in approximately 1.4/1,000 total births (1,18–25) When the injury persists past 12 months of age, continuing outcomes may include joint subluxation, muscle weakness, and sensory dysfunction (79). Until the early 1990's, it was thought that NBPP solely occurred due to trauma induced by lateral neck traction caused by the birthing attendant (exogenous force). Since then, clinical evidence has demonstrated that both temporary and permanent NBPP can occur due to other mechanisms of injury. Factors affecting the mechanism of injury may include bending of the neck, fetal malpositioning, labor induction, labor abnormalities, operative vaginal delivery, and shoulder dystocia (1).

NBPP injuries are difficult to research clinically due to ethical issues that surround the vulnerable subject group - infants. Finite element models (FEM) present an opportunity to investigate various aspects of NBPP. Currently, only two models of the adult brachial plexus have been published (67,68). The anatomy of the surrounding bone and ligament structures were obtained through MRI scans; however, both papers were unable to assess the anatomy of the brachial plexus distal to the nerve trunks. As both the anatomy and the material properties of the brachial plexus are expected to be different between neonates and adults, it is important to develop a more accurate neonatal model of the brachial plexus if the goal is to investigate the mechanisms of NBPP. To date, no FEM model of the neonatal brachial plexus and spinal cord have been published in the literature – neither two-dimensional nor three-dimensional. The objective of this study was to create a two-dimensional model of the neonatal brachial plexus that could be used to investigate how stress develops in the various brachial plexus roots when loads and displacements are applied. The first phase of the project focuses on the development and validation of the model. The second phase focuses on analyzing the effect of stress on the nerve roots based on variations in the angles between the nerve roots and the spinal cord that occur through normal anatomical variations.

Methods

ABAQUS CAE (v. 2022, Dassault Systèmes) was used to design, mesh, and analyze a brachial plexus and spinal cord model of a human neonate. Vertebral bodies and connective tissue surrounding the spinal cord and its connection to the nerve roots were not included in this 2D model. The properties and anatomy of the connective tissue around the junction of the nerve roots to the spinal cord have not been fully described. As the impact of the 3D structure of the vertebral bodies and spinal ligaments cannot be easily translated into the plane of this model, their effects were included through the applied boundary conditions (as described below) rather than adding additional structures.

While in reality the brachial plexus is divided into five sections – roots, trunks, divisions, cords, and terminal nerves, our 2D model was constructed solely of the roots and trunks due to the 3D, anatomical complexity that occurs within the division section **(Figure 16).**

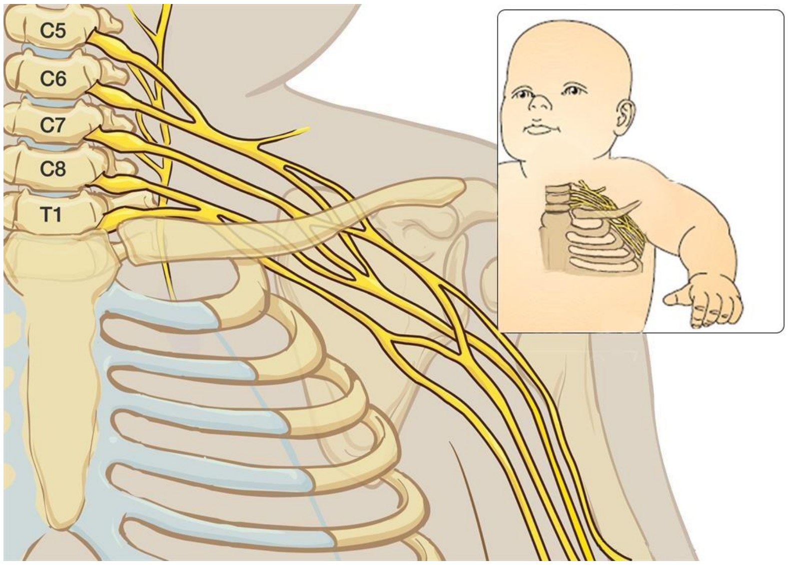

Figure 16: Anatomy of the brachial plexus. The brachial plexus is made of five sections: roots, trunks, divisions, cords, and terminal branches.

The model was designed based on dimensions measured by colleagues at the University of Michigan's Neurosurgery Department during primary reconstructive surgery. Average dimensions obtained from 23 infants were provided to the modeling team and are listed in **Table 13**. This included the length of the sections as well as both the transverse and cranial-caudal dimensions of each nerve root. The cranial-caudal dimensions were used to represent the thickness of the nerves in this 2D model, as that dimension falls within the plane of analysis.

Table 13: Average Dimensions for Infant Brachial Plexus.

Dimensions (mm)	C5	C6	C7	C8	T1
Cranial Caudal root diameter	3	3.1	3.8	2.7	2.5
Transverse root diameter	1.1	1.3	1.6	1.4	1.4
Spinal root to dorsal root ganglion	7.5	7.5	7.5	7.5	7.5
Dorsal root ganglion to end of bony foramen	9	8	7	5.5	-
Foramen to formation of trunk	14	15.5	19	7	6

Two cases were developed to represent the difference between quasistatic stretch (0.01 mm/second) and dynamic stretch (10 mm/second) of the nerves, as seen in **Table 12**. Within ABAQUS software, boundary conditions and loads were established. The boundary conditions were the same for both cases, including an encastré condition to the midline of the spinal cord and XSYMM conditions to the superior and inferior portions of the five nerves. The encastré boundary condition constrained all active structural degrees of freedom within the edge selected and the XSYMM boundary condition allowed the nerve to stretch only in the plane of the model when loads were applied. Encastré is known as a fixed boundary condition in other more common finite element modeling software. The XSYMM boundary condition has symmetry about a plane X = constant (U1 = UR2 = 0). These boundary conditions were selected to represent the anatomical constraints that limit deformation or displacement of the spinal cord and nerve roots *in situ*. The encastré and XSYMM boundary conditions can be seen in **Figure 17**.

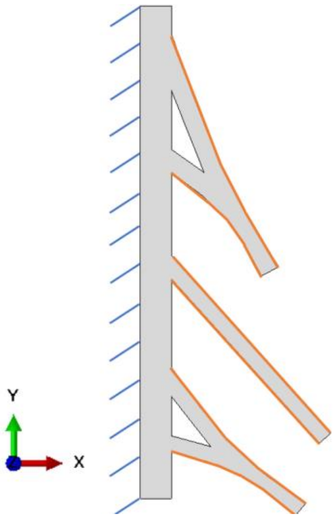

Figure 17: Boundary conditions used within ABAQUS software. An encastré (fixed) boundary condition to the midline of the spinal cord (blue lines) and XSYMM boundary condition to the superior and inferior surfaces of the five nerves (orange lines).

To date, there has been no assessment of the mechanical properties of the human neonatal brachial plexus. Thus, the Young’s modulus and Poisson’s ratio were from data collected from neonatal piglets, as seen in **Table 12** (6,80). The same material properties were used for both the brachial plexus and the spinal cord, as the model was constructed as a single, deformable structure.

In phase one, a load was applied perpendicular to the plane of the distal end of each trunk, and the resulting stress was evaluated against *in vitro* tensile tests conducted on neonatal piglets. In phase two, the model was changed to evaluate the effect of different nerve root angles on the stress that develops within the nerve root. Loads were again applied perpendicular to the distal end of each trunk. In both phases of the study, the values of stress were analyzed by identifying the element with the maximum stress at the junction between the nerve root and the spinal cord.

Phase One – Validation of Two-Dimensional Model

Two different loading conditions were examined with the model, as summarized in **Table 14.** Both simulated a pulling force applied to the nerves at the distal end of the trunk, as would occur with the depression of the shoulder while the head and neck remained aligned with the axis of the spine. Two different loading rates were simulated, to match experimentally available data for validation (6). Tests at higher loading rates demonstrated both higher Young's Modulus and failure load, due to the viscoelastic nature of nerves. For each case, the appropriate material properties were defined within the model, and the experimentally determined maximum load was applied.

A tensile force of 5x the load to rupture a single nerve root **(Table 14)** was divided between the trunks based on composite theory. As the Young's modulus was constant for the three trunk levels, the load to each trunk was defined as being proportional to its cross-sectional area. The stretch-inducing load was modeled as an applied pressure distributed over the distal end of each nerve trunk – at the junction with the division. Thus, the upper trunk connected to the C5 and C6 nerve roots, the middle trunk was the extension of the C7 nerve root, and the lower trunk included the C8 and T1 nerve roots. The magnitude of the pressure was calculated based on the share of the load on each trunk normalized by the estimated cross-sectional area. The cross-sectional area of each nerve root was calculated based on an ellipse with the major and minor axes equal to the cranial-caudal and transverse dimensions **(Table 13),** and the areas used were then summed for the upper (C5 + C6) and lower (C8 + T1) trunks, assuming that the tissue volume (and thus cross-sectional area) was maintained as the roots combined into trunks. As area factored into both the distribution of the force across the five nerve roots and the conversion of the force on each trunk to an applied pressure, the pressure was equal for each of the trunks **(Table 14).** The applied pressure for the distal portions of the three trunks in Case 1 was 0.332 MPa. For Case 2, the applied pressure was 0.653 MPa.

Table 14: Mechanical Properties Applied within 2D Model of the Neonatal Brachial Plexus and Spinal Cord – As Measured in Piglet Brachial Plexus Roots at Two Loading Rates (6,80).

Case	Loading Rate [mm/sec]	Maximum Load [N]	Young's Modulus [MPa]	Poisson's Ratio	Applied Pressure at Distal Trunk [MPa]
1	0.01	1.08	1.48	0.4	0.332
2	10	2.12	2.02	0.4	0.653

Phase Two – Anatomical Variations

In phase one, a two-dimensional model of a neonatal brachial plexus was created and validated in comparison to an *in vitro* neonatal piglet study (see Results). The angles were constrained for C5/C6 and C8/T1 based on the clinically-measured lengths of the respective nerve roots **(Table 13).** This base-line geometry was reviewed by the University of Michigan Neonatal Brachial Plexus Program team to confirm that it was reasonable compared to *in vivo* observation. Phase two used the validated model and created anatomical variations in order to evaluate the effect of different nerve root angles on the stress that develops within the nerve root. The starting angle for each nerve root was measured in ABAQUS for phase one - the validated model **(Figure 18).** The anatomy of the validated model was then adjusted to represent a change in the angle between each nerve root and the spinal cord (± three and six degrees), the same stretch-inducing pressures were applied to the distal end of the trunks, and the stress in the proximal nerve root was then evaluated.

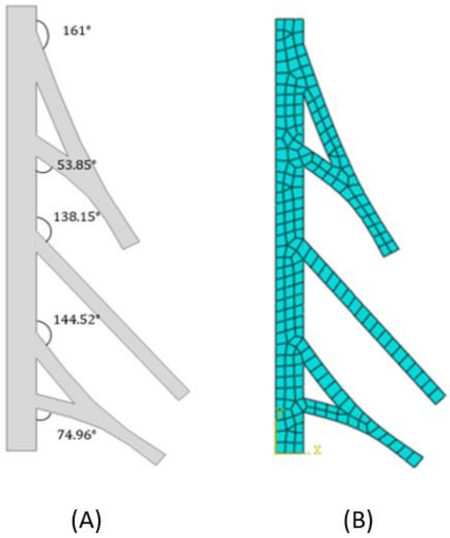

Figure 18: (A) Original geometry of the spinal cord + brachial plexus root/trunk model with the initial angles at each nerve root indicated; and (B) Mesh of 2D FEM of a neonatal brachial plexus and spinal cord.

Results

Phase One-Validation

A mesh convergence was conducted to determine the number of required elements to ensure that the results of the analysis are not affected by the mesh size and therefore provide an accurate solution. A maximum global mesh size of 2 mm and a minimum mesh size of 0.2 mm was used throughout the model. The model was meshed with a total of 304 nodes and 212 elements – 206 linear quadrilateral (CPS4R) and 6 triangular (CPS4). **Table 15** provides the maximum values of stress predicted at each nerve root by the model for both loading cases. All stress measurements were taken at the proximal end of the nerve root, where it intersects with the spinal cord.

Our model was validated through comparison with the results of Dr. Anita Singh (6). Dr. Singh calculated a stress in the piglet brachial plexus corresponding to the experimentally-measured failure load. For Case 1, the maximum stress found experimentally was 0.200 MPa, and for Case 2 it was 0.450 MPa. In our model, the predicted maximum Von Mises stress for C5 in Case 1 was 0.246 MPa, and in Case 2 was 0.486 MPa **(Table 15).** C5 was selected as the nerve root for comparison in this validation because it is the first nerve root that experiences failure in a brachial plexus injury when the arm is adducted - which matches the alignment of the brachial plexus with the spinal cord in this model. As the model will eventually be used to better understand NBPP, and most births occur with the arm adducted, this was determined to be the appropriate starting point for evaluating the stress that occurs in the nerve roots. C5 and C6 nerve roots experience the highest stress and the largest displacement in comparison to the lower nerve roots, which correlates with clinical patterns of injury.

Table 15: Maximum stress values in the proximal nerve root for Case 1 (low loading-rate properties – 0.01 mm/sec) and Case 2 (high loading-rate properties – 10 mm/sec). Stress values were identified at the proximal end of the nerve root, where it joins with the spinal cord**.**

Von Mises Stress [MPa]	**Comparison Maximum Nerve Trunk/Root Stress – Experimental Mean** (6)	**C5**	**C6**	**C7**	**C8**	**T1**
Case 1	0.200 +/- 0.020	0.246	0.250	0.236	0.171	0.181
Case 2	0.450 +/- 0.040	0.486	0.495	0.466	0.327	0.357

The results are presented visually for Case 1 in **Figure 19**. The pattern of stresses was the same for Case 1 and Case 2, as the nerve roots were modeled as homogeneous, linear elastic materials. The alignment between the predicted stress at the proximal nerve root of C5 and the experimentally measured failure stress for an isolated root/trunk segment gave confidence that the model was reasonably biofidelic and that it could be used for other parametric analyses.

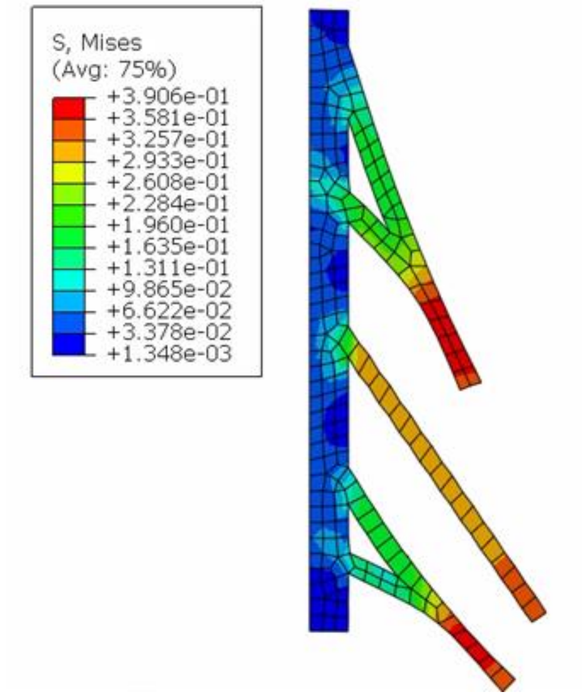

Figure 19: Von Mises Stress results of Case 1 model (low loading-rate properties – 0.01 mm/sec).

<u>Phase Two – Anatomical Variations</u>

Using the validated model, variations from the original anatomy in the angle between each nerve root and the spinal cord (± three and six degrees) were created, and the stress in the proximal nerve root was then evaluated. The variation in predicted Von Mises stress is reported in **Table 16** and **Figure 20**.

Table 16: Results of Case 1 model (low loading-rate properties – 0.01 mm/sec) with a range of nerve root angle iterations.

	Maximum Stress Values at the Nerve Root [MPa and %]				
	6 Degree Increase	**3 Degree Increase**	**Original Anatomy**	**3 Degree Decrease**	**6 Degree Decrease**
C5	0.137 (-44%)	0.182 (-26%)	0.246	0.218 (-11%)	0.278 (+13%)
C6	0.275 (+10%)	0.280 (+12%)	0.250	0.248 (-1%)	0.308 (+23%)
C7	0.301 (+28%)	0.306 (+30%)	0.236	0.285 (+21%)	0.292 (+24%)
C8	0.180 (+5%)	0.203 (+19%)	0.171	0.203 (+19%)	0.286 (+67%)
T1	0.209 (+15%)	0.210 (+16%)	0.181	0.205 (+13%)	0.298 (+65%)

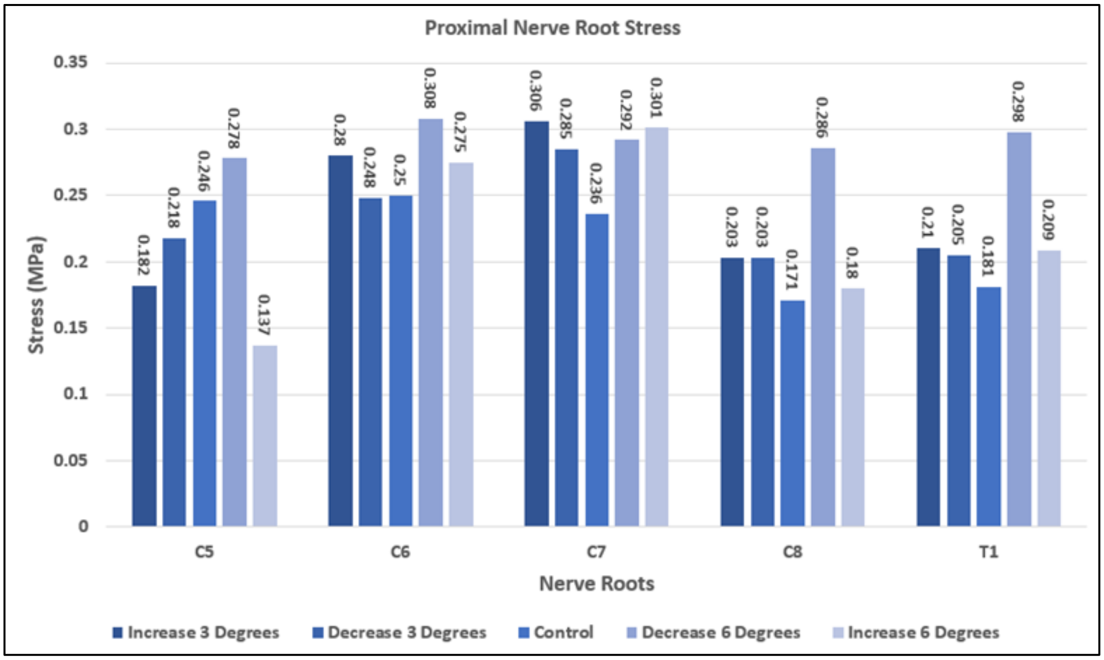

Figure 20: Results of Case 1 model (low loading-rate properties – 0.01 mm/sec) with a range of nerve root angle iterations.

There was no clear pattern in the change in stress predicted at the junction of the nerve root and spinal cord for the variations in nerve root angle. At C5, the stress decreased to 56% of the original baseline value when the angle between the nerve root and the spinal cord increased by only 6 degrees. With a 6 degree decrease in angle with respect to the spinal cord, the model predicted an increase in stress in C5 of 13%. In contrast, C6 saw an increase in stress with both increases in the nerve root angle (10% and 12% at +6 and +3 degrees) as well as a 23% increase in stress for the decrease in angle of 6 degrees. At a decrease in angle of 3 degrees, the stress in C6 changed only by 1%. Looking at the lower trunk, the predicted stress in the C8 and T1 nerve roots increased for all four changes in angle – up to 67% higher than the control model with a decrease of 6 degrees. The stress at the C7 nerve root increased by between 21% and 30% for both the increases and decreases in the nerve root angle, demonstrating much more consistency compared to other nerve roots.

Discussion

To date, only two models of a brachial plexus – either 2D or 3D – have been published in the literature, and both represent adult anatomy and material properties. The first model, published in 2017 (68), was designed to investigate the effect of non-linear tissue properties instead of linear (Hookean) properties on prediction of tissue deformation during image-guided surgery.

Unsurprisingly, they found that non-linear properties (Ogden hyperelastic model) provided more accurate deformation and displacement of the brachial plexus when comparing the predictions to an MRI assessment. However, the Perruisseau-Carrier study was not interested in assessing injury or the stress in the tissue. The second assessed the effect of angular displacement of the neck on the strain in the various nerve roots and compared that to clinical patterns of injury for validation (67). As in the current study, Mihara and colleagues used linear, isotropic properties to describe each of the tissues. The Mihara model appears to have used the properties of the dura mater surrounding the spinal cord rather than of the spinal cord itself in the analysis. Mihara did not have any direct experimental results to compare their predictions to, and so validated the model strictly based on the pattern and location of maximum strain compared to clinical injury patterns. Interestingly, they did not reach their stated injury threshold of 30% in any of the nerve roots in any of the simulated neck motions – with a maximum of 21% strain for 33° retroflexion (pulled backwards) of the cervical spine and 15% for 23.5° lateroflexion (bent to one side – in this case, bent away from affected brachial plexus) of the cervical spine. Mihara and colleagues did not discuss the likely effect of using linear instead of non-linear properties on the predicted strain, and they also constructed their brachial plexus segments without the benefit of images or otherwise measured dimensions. Neither the Perruisseau-Carrier nor the Mihara models included structures of the brachial plexus distal to the trunks – simply extending the trunks distally down the arm.

Thus, the existing work provides many opportunities to advance modeling of the brachial plexus – with respect to infant anatomy and material properties, validation through comparison to experimental measurements, and construction of an anatomically accurate 3D model of the brachial plexus. The current paper takes some initial steps in that direction – developing and validating a 2D model of the infant brachial plexus using appropriate anatomical and material property data and comparing predicted stress to experimental studies. Following validation, the effect of small variations in anatomy were investigated, which has not been evaluated previously within biomechanical literature.

When it comes to any finite element analysis, limitations exist and must inform the application of the results. In our model, the first limitation stems from the fact there are no neonatal values for mechanical properties of the human infant brachial plexus and spinal cord, thus the needed use of data from neonatal piglets. However, the similarity in structure and size provides a level of confidence that this surrogate is a reasonable match for human tissue of the same age –

especially given the range of normal biomechanical properties seen in both species. The second limitation is the inability to model the complete brachial plexus in two dimensions. The need to stop at the division level limits our ability to study the entirety of the brachial plexus and does require loads to be applied through the distal end of the nerve trunk rather than being transmitted from further down the upper extremity. The third limitation is the inability to accurately apply the loads within the model due to lack of data pertaining to how the load is distributed within nerves, as well as the model being simplified in two dimensions. In reality, load will be transferred to each trunk through the distal portions of the nerves and the pathway that the load will follow up the nerve to each nerve root is not simple. The two existing brachial plexus models did not address the issue of load distribution between the portions of the plexus as they induced stress through displacement instead of an applied load. Thus, the reason we selected the course of action to apply the load within this model is to simulate the bending of the infant’s neck away from the anterior shoulder during the birthing process.

A 2D model will never fully describe the behavior observed in an actual brachial plexus structure due to the limitations that exist in representing the complex anatomy. However, conducting a stress analysis on an anatomically accurate two-dimensional brachial plexus model allows for validation using available *in vitro* piglet data. Having the ability to validate the 2D model by matching experimentally-determined stress, strain, and force data allows for a level of confidence that this piglet data can be used in the next step, which involves developing a 3D model. Clinical patterns of injury and some experimental work (6) demonstrate that C5 and C6 experience higher stress under initial loading of the brachial plexus than do the lower roots. Our simulation also demonstrated that pattern of stress, as seen in **Table 15**, even without the complete, complex anatomy of the plexus. This provided an initial level of comfort that the model had some degree of biofidelity. While the applied pressure was distributed based on the nerve root cross-sectional areas, the resulting stress was not constant across the five nerve roots. Thus, the anatomy drove the higher stress at C5 and C6 rather than simply being a balance between applied force and cross-sectional area **(Figure 19).**

One of the goals of this study was to validate the model against previous literature such that our predicted values of stress were similar to those obtained through experimental testing. As no other model of the human neonatal brachial plexus has to date been published, it is not possible to compare findings from this model to previous models. When the maximum stress predicted at the proximal end of the nerve root from the model was compared to the failure stress determined from testing of piglet brachial plexus mechanical response, the original anatomy was able to reasonably match the stress values at both the high and low deformation rates. While it may be assumed that such a comparison is trivial as both the loading conditions and the material properties came from the same experimental studies, it must be remembered that the anatomy of this 2D model was determined from clinical measurements on humans – not based on the piglet. Thus, while the failure properties of the neonatal piglet brachial plexus (in terms of stress and strain) are expected to be representative of what would be found in a human infant, this model allows for the fact that there are anatomical differences between the species.

When comparing the predicted displacement and strain to the maximum experimental strain, the values predicted by this model were significantly lower than those seen experimentally **(Table 17).** This is most likely due to the model being developed and analyzed using linear elastic material properties in comparison to a non-linear material. An isotropic linear elastic material can be characterized by two physical constants, including Young's modulus and Poisson's ratio. A linear elastic model can be described by a linear relationship between stress and strain – this relationship is known as Hooke's Law. However, a non-linear elastic material does not obey Hooke's Law. Biological tissues, including nerves, typically display a region of low stiffness followed by an almost linear increase in the elastic region – ending with a yield stress value that may cause failure to the material or may allow plastic deformation before final rupture occurs. Singh only reported single values for Young's modulus, and did not include any information on the initial, nonlinear region. However, it is reasonable to assume that the nerve segments did actually demonstrate non-linear behavior. But without any information on that early, low-stiffness behavior of the plexus, the model – using linear elastic properties – is not able to simulate the high deformation-low stress region of the response. Thus, if the non-linear characterization of the neonatal brachial plexus nerve roots is available and can be included in a model, the predicted deformation and strain would be expected to increase – and then more closely match the experimental findings.

Table 17: Comparison of predicted displacement and strain compared to maximum experimental strain for Case 1 (low loading-rate properties – 0.01 mm/sec) and Case 2 (high loading-rate properties – 10 mm/sec). Displacement values were identified at the distal end of the trunk.

		Original Segment Length (SC to distal trunk) [mm]	**Predicted Displacement [mm]**	**Maximum Predicted Strain**	**Experimental Maximum Strain** (6)
Case 1	**Upper Trunk**	41.4	7.3	17.6%	24%
	Middle Trunk	38.3	3.8	9.9%	
	Lower Trunk	30.8	4.3	13.9%	
Case 2	**Upper Trunk**	41.4	10.6	25.6%	34%
	Middle Trunk	38.3	5.3	13.8%	
	Lower Trunk	30.8	5.8	18.8%	

As this model's anatomy only hints at the complex structure seen *in vivo*, it is clear that the results of the analysis can neither be used to predict actual deformation of the nerve roots seen during various loading scenarios nor to assess specific risk of injury for an individual. However, it is appropriate to use the model to investigate specific apples-to-apples comparisons, such as the effect of changes in the angle between the nerve root and the spinal cord. The examination of the effect of even small variations in the angle between the nerve root and spinal cord is important because it is well known that there is no single "normal" angle that will be observed among all neonates – anatomical variation is one of the sources of biological variability from one individual to the next. The findings in Phase Two of this study show that a slight variation within the nerve root angles, either an increase or a decrease, significantly changed the stress values at the proximal nerve root, as seen in **Table 17.**

This variation in stress will parallel an increase or decrease in strain and therefore the likelihood of failure at each nerve root. This study provides insight into one of the factors that may affect an individual infant's susceptibility to brachial plexus injury during the birthing process. It also justifies a more complete assessment of the effect of anatomical variations within a 3D model – which is much more complicated.

This 2D model is the first step towards developing a complete 3D model of the neonatal brachial plexus. Future work will include creating a complex 3D model with all five sections of the brachial plexus – roots, trunks, divisions, cords, and branches. This will provide the opportunity to more accurately assess the effect of the birth process on the stretch within the brachial plexus and the impact of biological variations in structure and properties on the risk of NBPP.

Acknowledgements

We thank our colleagues from Dr. Lynda Yang’s neurosurgery team at the University of Michigan, who provided insight and expertise that assisted the research – including the infant nerve dimensions.

Chapter 6: Collection Process of Adult Brachial Plexus Dimensions

The ability to collect neonatal measurements of the brachial plexus is severely limited due to the lack of exploratory surgeries on this age of subjects. One can collect measurements of the lengths of specific portions of the plexus via medical images. However, a large part of the plexus cannot be measured using medical images due to the obstruction of the clavicle. The transverse dimensions of the plexus also cannot be collected from standard medical images due to the inability to collect three-dimensional images.

The objective of this chapter is to describe the processes used to obtain anatomically-accurate neonatal brachial plexi dimensions through the use of neonatal reconstructive surgery, adult cadaveric dissection, and adult MRI imaging. Through the combination of these three techniques – a ratio was developed to accurately scale the known adult dimensions to develop appropriate neonatal dimensions to be used within the three-dimensional computational model discussed in **Chapter 7 and 8. Figure 21** illustrates a flow chart to describe the dimension collection process.

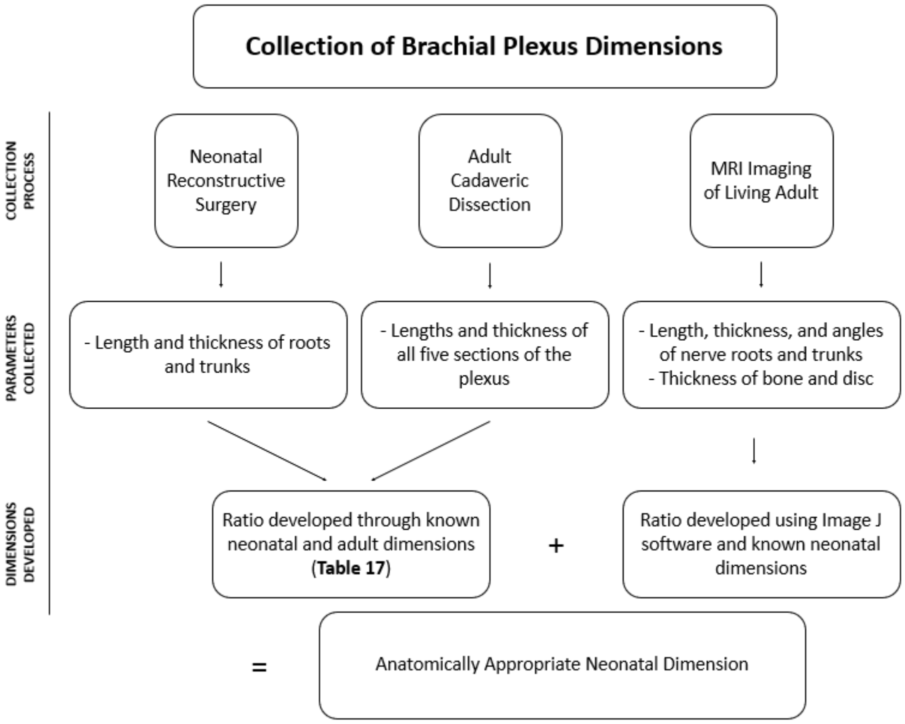

Figure 21: Flow chart describing the process used to collect, ratio, and develop neonatal dimensions through neonatal reconstructive surgery, adult cadaveric dissections, and MRI imaging.

Collection of Brachial Plexus Dimensions – Surgery, Dissection, and Images

Collection of Neonatal Brachial Plexus Dimensions through Reconstructive Surgery

The dimensions of neonatal brachial plexus roots and trunks had been collected during primary reconstructive surgery through Dr. Lynda Yang from the University of Michigan's Neurosurgery department. Specifically, the lengths and thicknesses of the roots and trunks were collected, and average data were provided to this research group. During the reconstructive surgery, the surgeons were unable to measure the more distal portions of the plexus as they were not exposed during the surgery. Thus, no measurements were available for the structure beyond the trunks. **Table 18** shows the collected average neonatal dimensions.

Table 18: Average neonatal dimensions (length and thickness) collected through primary reconstructive surgery [n=3].

	Neonatal Dimensions		
	Length [mm]	**Cranial Caudal [mm]**	**Transverse [mm]**
C5 Root	14.00	3.00	1.10
C6 Root	15.50	3.10	1.30
C7 Root	19.00	3.80	1.60
C8 Root	7.00	2.70	1.40
T1 Root	6.00	2.50	1.40
Upper Trunk	11.00	6.00	1.83
Middle Trunk	19.00	3.80	1.60
Lower Trunk	11.00	2.25	1.26

Collection of Adult Brachial Plexus Dimensions through Cadaveric Dissection

Due to the inability to collect the complete neonatal dimensions through reconstructive surgery, another process was needed to identify appropriate dimensions. In discussion with the University of Michigan's Department of Neurosurgery, it was agreed that determining a ratio between representative adult dimensions and the known neonatal dimensions was an appropriate strategy. Thus, dissection of the brachial plexus of two adult cadavers was undertaken. The left and right plexus dimensions were collected for each cadaveric specimen. Dimensions included the segment lengths as well as the cranial caudal and transverse dimensions of the roots through to the terminal branches. **Figure 22** portrays a left plexus dissection of an adult male. During the dissection process, the complete set of dimensions for the second cadaver was unable to be collected. Thus, average values were calculated from only one cadaver (both the left and right plexus), and these values were used to as the representative adult dimensions seen in **Table 19.**

Figure 22: Left brachial plexus dissection on an adult male cadaver (Roots – Branches).

Table 19: The mean adult brachial plexus dimensions collected from one cadaveric specimen using both the left and right plexus. The terminal branch lengths were unable to be collected during the dissection as they extended all the way to the hand.

Adult Brachial Plexus Dimensions			
	Length [mm]	**Cranial Caudal [mm]**	**Transverse [mm]**
C5 Root	35	4	3
C6 Root	27.5	7	4
C7 Root	30	7	5.5
C8 Root	20	5.5	4.5
T1 Root	17.5	4.5	4
Upper Trunk	30	8.5	5
Middle Trunk	16.4	7	5
Lower Trunk	50	5	4.5
Upper Anterior Division	52.5	4.5	2.5
Upper Posterior Division	25	5	4
Middle Anterior Division	32.5	5	4
Middle Posterior Division	25	3.5	3
Lower (C8) Anterior Division	30	4.5	3.25
Lower (C8) Posterior Division	75	4.5	3.5
Lateral (Upper) Cord	40	8	4
Middle Cord	50	8.5	5.5
Posterior (Lower) Cord	20	8.5	7
Musculocutaneous Branch	NA	3.5	2.5
Axillary Branch	NA	4.5	2.5
Median Branch	NA	3	2
Ulnar Branch	NA	3	2
Radial Branch	NA	5	4

After the dimensions were collected from the adult plexus, scaling ratios were calculated between segments of the adult anatomy – the length and thickness of each of the more distal segments was related to the size of the roots. Thus, the size of each of the distal segments was related to a dimension that had previously been measured in the infant brachial plexi.

Table 20: Scaling ratios calculated between segments of the adult brachial plexus. All sizes were related to either the root or trunk dimensions so that they could subsequently be applied to the measured neonatal dimensions.

Scaling Ratios				
	Equations	**Length**	**Cranial Caudal**	**Transverse**
Upper Trunk	$\frac{C5\ Root}{Upper\ Trunk}$	1.17	0.47	0.60
Middle Trunk	$\frac{C7\ Root}{Middle\ Trunk}$	1.83	1.00	1.10
Lower Trunk	$\frac{C8\ Root}{Lower\ Trunk}$	0.40	1.1	1.59
Upper Anterior Division (UAD)	$\frac{C5\ Root}{UAD}$	0.67	0.89	1.2
Upper Posterior Division (UPD)	$\frac{C5\ Root}{UPD}$	1.40	0.80	0.75
Middle Anterior Division (MAD)	$\frac{C7\ Root}{MAD}$	0.92	1.4	1.38
Middle Posterior Division (MPD)	$\frac{C7\ Root}{MPD}$	1.20	2.00	1.83
Lower (C8) Anterior Division (LAD)	$\frac{C8\ Root}{LAD}$	0.67	1.22	1.38
Lower (C8) Posterior Division	$\frac{C8\ Root}{Upper\ Trunk}$	0.27	1.22	1.29
Lateral (Upper) Cord	$\frac{C5\ Root}{Lateral\ Cord}$	0.88	0.50	0.75
Middle Cord	$\frac{C7\ Root}{Middle\ Cord}$	0.60	0.82	1.00
Posterior (Lower) Cord	$\frac{Lower\ Trunk}{Posterior\ Cord}$	1.00	0.65	0.64
Musculocutaneous Branch	$\frac{C5\ Root}{Musc.Branch}$	NA	1.14	1.20
Axillary Branch	$\frac{C7\ Root}{Axillary\ Branch}$	NA	1.55	2.20
Median Branch	$\frac{C7\ Root}{Median\ Branch}$	NA	2.33	2.75
Ulnar Branch	$\frac{C8\ Root}{Ulnar\ Branch}$	NA	1.83	2.25
Radial Branch	$\frac{C8\ Root}{Radial\ Branch}$	NA	1.1	1.13

As a check on the assumption that ratios calculated for the dimensions of the adult brachial plexus could provide reasonable anatomy for a neonatal plexus, the ratios between the root and trunk measurements were compared between the infant and adult specimens **(Table 21).** The only ratio that was significantly different between the adult and infant specimens was for the length of the C7 root compared to the middle trunk. As the middle trunk extends directly and only from the C7 nerve root, this difference is most likely due to differences in the assessment of where that nerve root transitions into the trunk. There is not a merger of nerve roots in the trunk as seen with the upper or lower trunks. Overall, this comparison reinforced our approach to determining appropriate dimensions for the neonatal model.

Table 21: Calculated root and trunk ratios for both infant and adult brachial plexus dimensions.

	Length		**Cranial-Caudal**		**Transverse**	
	Adult	**Infant**	**Adult**	**Infant**	**Adult**	**Infant**
$\frac{C5\ Root}{Upper\ Trunk}$	1.17	1.27	0.47	0.50	0.6	0.60
$\frac{C7\ Root}{Middle\ Trunk}$	1.83	1.0	1.0	1.0	1.1	1.0
$\frac{C8\ Root}{Lower\ Trunk}$	0.4	0.64	1.1	1.2	1.0	1.1

By applying the calculated scaling ratios to the average neonatal dimensions of the roots and trunks, anatomically appropriate neonatal brachial plexus dimensions were developed for the full plexus, as seen in **Table 22.** These dimensions were then used to develop the novel three-dimensional computational model presented in **Chapter 7 and 8**. As the terminal branches extend distally beyond what is normally considered to be the brachial plexus, and those lengths were not measured in the adult cadavers, only the proximal portion of the branches was included in the model.

Table 22: Neonatal Brachial Plexus Dimensions calculated from measured root and trunk dimensions **(Table 16)** using the scaling factors listed in **Table 18.**

Anatomically Appropriate Neonatal Plexus Dimensions			
	Length [mm]	**Cranial Caudal [mm]**	**Transverse [mm]**
Upper Anterior Division	21.00	3.33	1.76
Upper Posterior Division	19.60	3.00	1.10
Middle Anterior Division	17.54	4.84	2.51
Middle Posterior Division	22.80	7.60	2.93
Lower (C8) Anterior Division	27.22	1.96	1.22
Lower (C8) Posterior Division	10.89	1.96	1.13

Table 22 (cont'd)

Lateral (Upper) Cord	12.25	2.50	1.26
Middle Cord	11.40	3.13	1.60
Posterior (Lower) Cord	6.53	3.00	1.37
Musculocutaneous Branch	NA	4.29	1.47
Axillary Branch	NA	5.32	3.52
Median Branch	NA	5.91	4.40
Ulnar Branch	NA	4.24	1.58
Radial Branch	NA	2.50	3.15

Chapter 7: Development and validation of a three-dimensional computational model of the neonatal brachial plexus

This chapter was submitted for publication to the Journal of Biomechanical Engineering on September 19,2023. The formatting was changed to fit this dissertation's formatting requirements. Citations for the references were adjusted to the bibliography at the end of the dissertation.

Abstract

Finite element modeling of biological systems – including bones, organs, and musculoskeletal soft tissues — is a significant component of today's biomedical literature when the research question addresses the response of the tissue to mechanical input, whether at the cell, tissue, or organ level. To date, there are a limited number of models that address the mechanical response of peripheral nerves; however, there are no published models of neonatal brachial plexus nerves. The brachial plexus is a complex set of nerves that may be injured during the birthing process, resulting in an injury known as Neonatal Brachial Plexus Palsy (NBPP). Injury to this set of nerves may cause a permanent deficit in the upper extremity if it persists past 12 months of age. Due to the impossibility of clinical investigation of human neonatal nerve injury response, injury mechanisms for the neonatal brachial plexus have not been investigated in-depth. Finite element modeling of this complex structure will allow us to scientifically evaluate biomechanical aspects of neonatal brachial plexus injuries – with a long-term goal of providing helpful insights to lessen the chances of these injuries occurring. The objectives of this paper are to: (1) develop a novel three-dimensional neonatal brachial plexus model; (2) validate the model against published *in vitro* experimental data; and (3) compare the computational results to clinical patterns of injury. This novel model was successfully developed and validated in comparison to tensile test data obtained from experiments on neonatal piglets.

Introduction

The brachial plexus is a complex set of nerves that extend from the cervical (C5) to the thoracic (T1) nerve roots. This network of nerves innervates the upper extremity and may be injured during the birthing process causing an injury known as Neonatal Brachial Plexus Palsy (NBPP). Permanent damage to the nerves occurs either as an avulsion and/or rupture of one or more nerves – most commonly within the roots of the plexus. A brachial plexus injury may cause muscle weakness as well as a decrease in movement and sensation in the upper extremities. NBPP occurs in 1-4/1000 vaginal births – about 10 percent of which persist past 12 months and result in a permanent deficit (1,18–25).

As the clinical investigation of human neonatal nerve biomechanics is impossible, the mechanisms for this injury have not been thoroughly investigated. Previously published research has shown that endogenous (maternal) and exogenous (clinician-applied) forces affect the fetus during the birthing process. However, to date, the amount of force, either endogenous or exogenous, needed to cause an injury to the human fetus' brachial plexus is unknown. In previous years, a multitude of biomechanical testing has occurred using animal surrogates, birth simulators, and human cadaveric model (48,53,54,56,58,69,81–84). These models provide some insight into either the mechanical response of an isolated nerve or the effect of forces external to the neonate on a reference structure (e.g., a single displacement transducer). However, no currently available model links the external force experienced by the infant to stress and strain within the complete brachial plexus such that it can be used to assess the likelihood of failure.

Computational modeling is an alternative way to investigate the pathomechanics and pathophysiology of nerves that experience injuries. The first objective of this project was to develop a novel three-dimensional computational model of a neonatal spinal cord and brachial plexus that includes all five sections of the plexus – roots, trunks, divisions, cords, and terminal branches. This model is superior to previously published computational models of the adult brachial plexus (67,68) as it was created to be anatomically accurate through the terminal nerves – showing the complexity within the divisions.

Once an anatomically accurate model was developed, the model was validated against experimental data obtained from neonatal piglets. The goal for the model at this stage was to apply a traction force to the five terminal nerve endings and analyze the change in stress along the plexus in comparison to previously published *in vitro* experiments.

This validated, anatomically accurate model of a neonatal brachial plexus was created to provide useful insight for researchers, neurosurgeons, and others interested in this injury and to scientifically evaluate biomechanical aspects of neonatal brachial plexus injuries – with the hope that the analysis will eventually provide helpful insight into ways to lessen the occurrence of these NBPP injuries.

Methodology

A finite element model (FEM) of a three-dimensional (3D) human neonatal spinal cord and brachial plexus model was designed, meshed, and analyzed within Solidworks (v. 2022, Dassault Systèmes). The anatomy of the brachial plexus includes five sections: roots, trunks, divisions, cords, and terminal branches. The complexity of the model includes anterior and posterior structures at the level of the divisions that extend into the plane of the third dimension. This 3D brachial plexus model was developed with the complete and correct anatomy for the five sections **(Figure 24).**

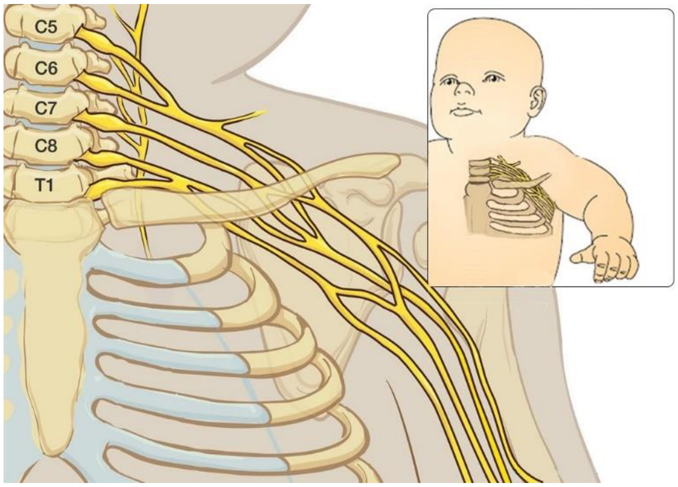

Figure 23: Anatomy of the brachial plexus. The brachial plexus is made of five sections: roots, trunks, divisions, cords, and terminal branches.

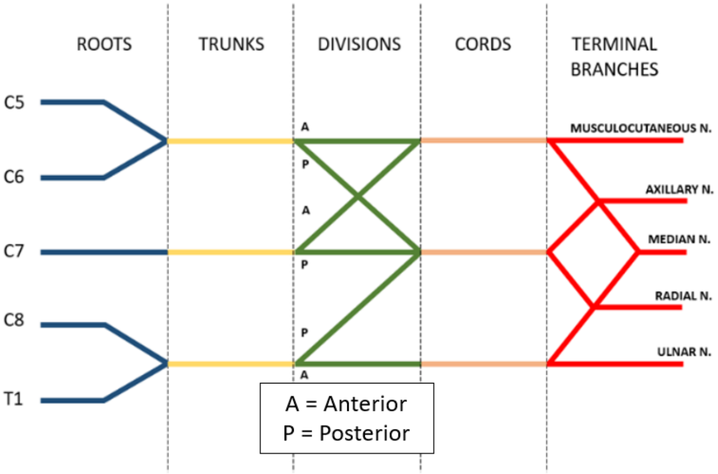

Figure 24: Simplified anatomical diagram of the brachial plexus.

Anatomical Data Collection

Computational modeling of biological structures often involves the use of medical imaging (MRI and CT) to develop the geometry of the model. The location of the brachial plexus does not allow this use of medical imaging due to a large portion of the plexus (divisions through the proximal portion of the terminal nerves) being obstructed by the clavicle. To develop this novel model – initial dimensions (diameters and lengths) for the nerve roots and trunks were collected by clinical collaborators during primary reconstructive surgery of infants (3 – 7 months of age). Mean values from this data were provided to the modeling team. The dimensions for the model's divisions, cords, and branches were determined based on proportional calculations in comparison to adult cadaveric dimensions, as measured during a dissection. Furthermore, spinal cord dimensions and the distance between nerve roots were analyzed based on MRI scans of the infants and calculated through ImageJ (github.com/imagej/ImageJ) software. The plexus was modeled as a single, solid structure, which eliminated the need to include the delicate *in situ* connections between the rootlets and the spinal cord white matter.

Boundary Conditions and Material Properties

The anatomy surrounding the brachial plexus is complex in nature and includes fascia, nerves, vessels, fat pads, and muscles. When creating the model, these surrounding features were taken into consideration for the development of boundary conditions. A standard fixed boundary condition was selected for the outer face of the spinal cord of the model. This finite element condition constrains all available degrees of freedom in the reference coordinate system (x, y, z) as the spinal cord is encased within the vertebral canal. A fixture constraint in relation to the front plane was used along the faces of the roots through the branches to prescribe zero displacements in the + y and ± z directions – as the nerves distally extend in the + x and - y direction when traction is applied approximately parallel to their length.

Due to the difficulty in analyzing human neonatal tissue *in vivo* and the inaccuracies found in cadaveric nerve biomechanics, there are no published material properties on human neonatal nerves. The Young's modulus and Poisson's ratio were therefore taken from neonatal piglets **(Table 23)**(6,80), with data obtained from both slow (0.1 mm/sec) and fast (10 mm/sec) rates of stretch. The same material properties were used for both the brachial plexus and the spinal cord. The model was analyzed using a linear elastic isotropic material model, based on the availability of property data. The use of material property data from two strain rates allowed the viscoelastic nature of the nerve to be taken into account within the model while still using linear elastic properties.

Table 23: Mechanical Properties of the Neonatal Brachial Plexus and Spinal Cord – Measured in Piglet Brachial Plexus Roots at Two Loading Rates. Case 1 represents a loading rate of 0.01 mm/sec and case 2 of 10 mm/sec. Maximum load and Young's Modulus were taken from a neonatal piglet experimental study (6) The Poisson's ratio value used was from a study conducted on fresh pig spinal cords [48].

Cases		**Maximum Load [N]**	**Young's Modulus [MPa]**	**Poisson's Ratio**	**Mass Density $[kg/m^3]$**
Experimental	1	1.08	1.48	0.4	-
	2	2.12	2.02	0.4	-
Computational	1		1.48	0.4	1000
	2		2.02	0.4	1000

A mesh convergence study was conducted to determine the number of required elements to ensure the results of the analysis were not affected by the mesh size and provide a mathematically accurate solution. An H adaptive mesh refinement was used to reduce the element size in areas of high strain within three iterations until a defined tolerance level was achieved. For this study, a 5% variation in predicted stress was selected as the tolerance level due to the variability that exists within both the material properties and anatomy between individuals – both of which impact the precision of the results. The refinement went through iterations portraying maximum element sizes from 4 – 1.5 mm, with the corresponding minimum element sizes of 0.25 – 0.12 mm. Taking into consideration computation time, number of nodes, number of elements, and the change in predicted stress between these iterations, the mesh size selected had a maximum element dimension of 2.48 mm and a minimum of 0.12 mm. The total number of nodes within the model was 269,637, with 165,439 elements. A tensile force was applied at the distal end of each nerve branch, as would occur with the depression of the shoulder while the head and neck remained aligned with the axis of the spine. The force was applied as a pulling force perpendicular to the distal, cross-sectional face of the nerve **(Figure 26).**

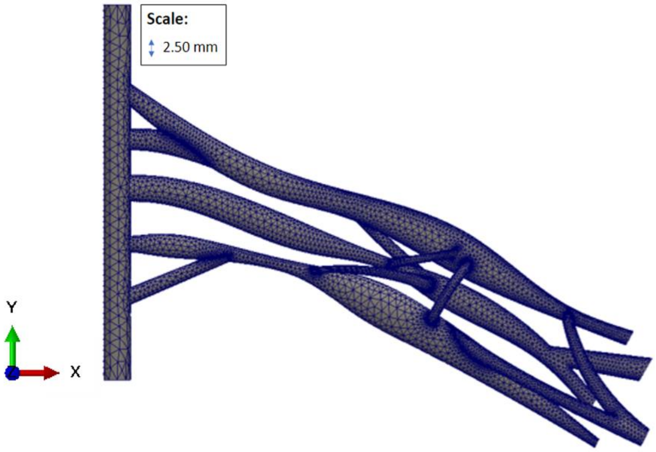

Figure 25: Meshed FEM of the brachial plexus developed for this study showing the spinal cord and all five sections of the plexus – roots, trunks, divisions, cords, and branches (frontal view).

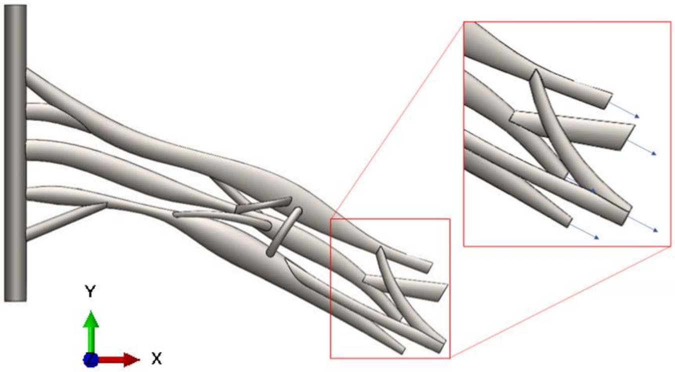

Figure 26: Loading conditions placed at the distal, cross-sectional faces of the five terminal nerve endings. The force was applied as a pulling force perpendicular to the distal, cross-sectional face of the nerve.

Data Analysis

A static analysis was conducted within Solidworks Simulation Module (v. 2022, Dassault Systèmes) to analyze the validity of the model. The model was validated against *in vitro* neonatal piglet data measured experimentally for both slow (Case 1) and fast (Case 2) deformation rates (6). Experimentally measured injury threshold values for the roots, cords, and terminal branches are provided for both cases in **Table 24.** The first objective of the analysis was to predict the amount of applied force needed to cause an injury-threshold (avulsion or rupture) level of stress at the plexus' roots in comparison to this known injury threshold data. The applied force value needed to cause the injury threshold level of stress at the C5 nerve root was determined for the two deformation rates - 0.22 MPa for Case 1 and 0.47 N for Case 2. C5 was selected as the region of interest as this is the location where the failure of the brachial plexus is initiated when the arm is adducted against the body (1).

Table 24: Experimentally measured injury threshold values at three locations – roots, cords, and terminal branches.

Injury Locations	Roots	Cords	Terminal Branches
Stress Values [MPa]	0.22	0.49	0.98

Results

Validation

The tensile force needed to simulate an injury causing stress to the C5 nerve root was 1.45 N equally distributed and perpendicular to each nerve ending. Clinical research has demonstrated that the cephalad nerve roots (C5/C6) have higher stress values than the lower roots (C8/T1) when loading of the full plexus is initiated with the arm in an adducted position. Our model confirms this outcome **(Figure 27 and 28).** The inferior portion of the C5 nerve root shows a stress value of 0.223 MPa – which demonstrates higher stress than the injury threshold **(Figure 28).** The lower nerve roots showed a lower predicted stress (under the injury threshold), with values of 0.135 MPa at C6 and 0.178 MPa at C7.

The stress value calculated above the injury threshold at the C5 nerve root was localized at the inferior portion of the root, as seen in red in **Figure 28.** In this case, failure would begin at this region of highest stress and then progress to rupture of the entire nerve root. Similar failure progression is seen in polymer ruptures in which the specimen's stress is localized to one region and then expands as the load is applied until rupture occurs (85).

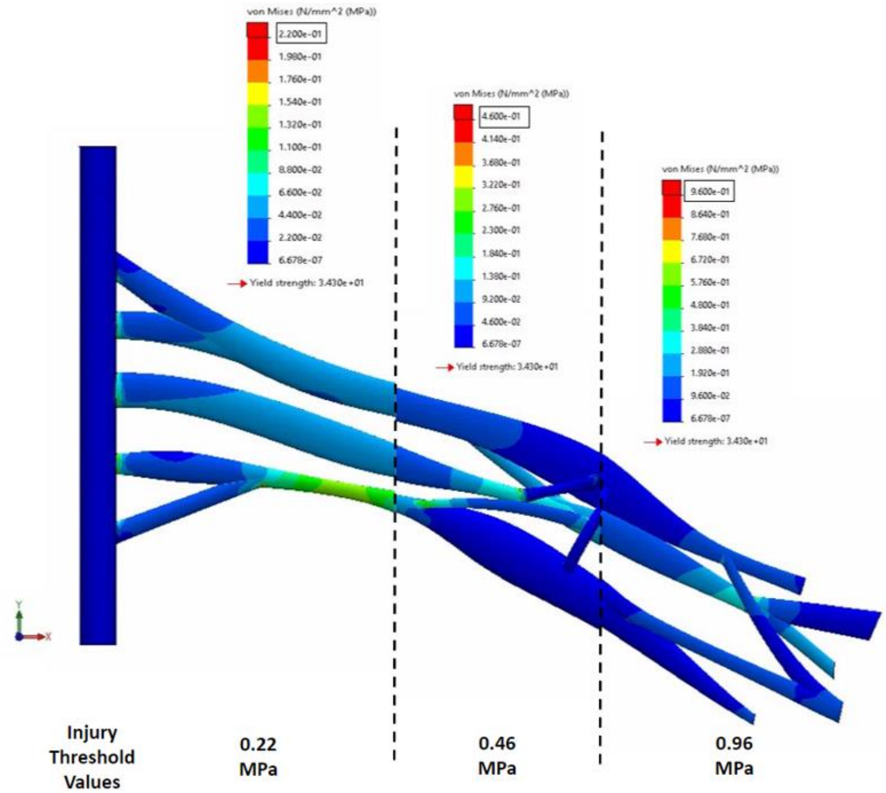

Figure 27: Von Mises stress analysis on a neonatal brachial plexus model indicating three injury threshold values along the plexus. Note that the injury threshold for the cords and branches is significantly higher than for the nerve roots and trunks. The color distribution has been adjusted for each of the more distal sections such that the injury threshold is indicated in red.

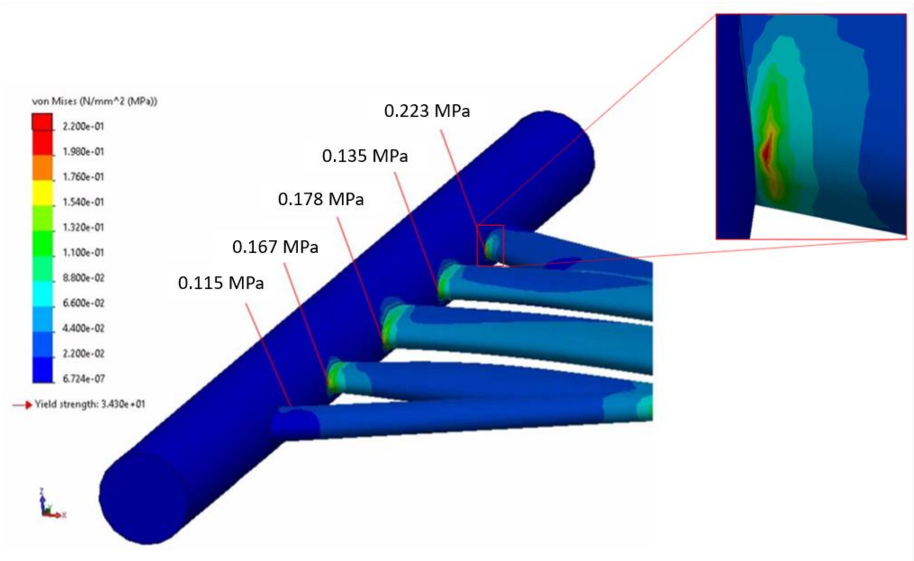

Figure 28: Von Mises stress analysis on a neonatal brachial plexus model where (a) red depicts stress values greater than 0.22 MPa and (b) showing C5 stress increases above the roots' injury threshold, resulting in a likely injury to the nerve root.

Using an element on the anterior surface of the upper trunk of the plexus and tracing a line along the length from the C5 nerve root through to the musculocutaneous nerve, the pattern of stress along the length of the plexus was identified **(Figure 29).** This was not the location of the maximum stress within a section, but within the cords and branches the maximum stress remained below their injury threshold level. The stress pattern along the plexus demonstrated that the stress does increase distally along the plexus, but still remains below the injury threshold for the cords and branches.

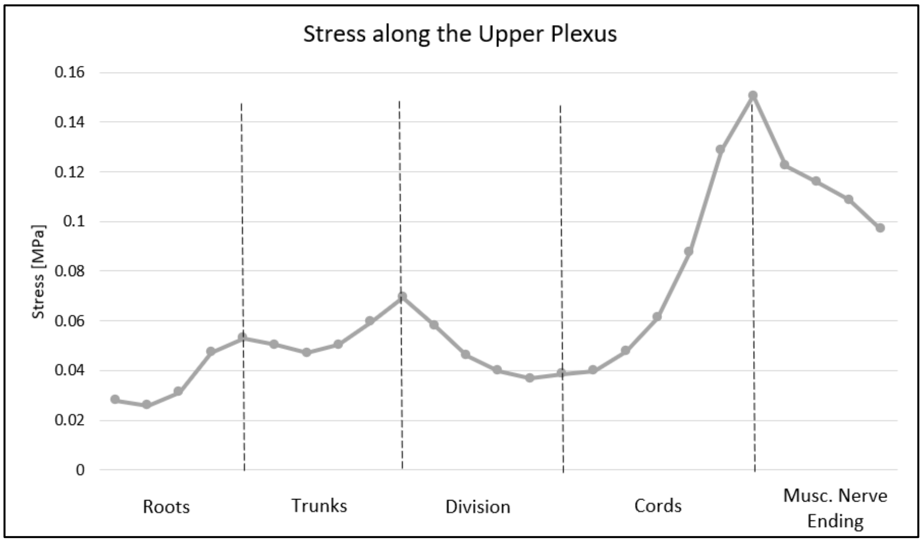

Figure 29: Von Mises stress value determined for a representative point at the middle of the anterior face of the upper plexus – C5 nerve root to the musculocutaneous nerve ending. The FEM predicted an increase in stress along the plexus.

In comparison to the experimental *in vitro* neonatal piglet study, the load needed to cause an injury of our human neonate FEM is higher in comparison **(Table 25).** This is due to the fact that the cross-sectional area of the sections of the neonatal plexus model is larger than those of the piglet brachial plexus used in the experimental research. The diameter of the human neonatal nerves is 1.7 ± 0.8 times that of the neonatal piglet nerves. For Case 1, the piglet load to failure is 26% less than the value predicted through the FEM, while for Case 2 the experimental failure load measured in the piglet is 34% less than that predicted with the FEM.

The validated model can now be used to investigate mechanisms of injury. For example, simulating a C5 injury (severing the C5 nerve root) supports the investigation of the progression of the injury from the C5 to the lower nerve roots. When C5 no longer carries its share of the load, the FEM results show that the stress value of the lower roots (C6 to T1) increased in comparison to the uninjured model. The uninjured maximum Von Mises stress value within the C6 nerve root was 0.135 MPa when 1.45 N was applied **(Figure 28)**; however, when C5 was severed, that value increased by 32% to 0.178 MPa under the same applied load. While this value is still below the injury threshold value of 0.22 MPa – the significant increase in stress after C5 fails demonstrates how this first event in the injury sequence affects the lower nerve roots. In the model simulation, the C6 nerve root will experience stresses that lead to failure with only 0.35 N of additional force.

Table 25: FEM of neonatal brachial plexus calculated loads for cases 1 and 2 in comparison to experimental values conducted on neonatal piglets (6).

	Infant BP FEM			**Experimental Results**		
	Load [N]	**Maximum Stress [MPa]**	**Musculocutaneous Nerve Diameter [mm]**	**Load [N]**	**Maximum Stress [MPa]**	**Musculocutaneous Nerve Diameter [mm]**
Case 1	1.45	0.22	2.25	1.08	0.22	0.9 ± 0.4
Case 2	3.20	0.50		2.12	0.49	

Discussion

In some children, there may be more than one level of nerve root in the brachial plexus that is injured during the birth process. To date, both computational and physical models developed to investigate the mechanisms of NBPP have relied on a single, indicator nerve for the upper plexus (82,86,87). An anatomically accurate model of the complex, 3D plexus allows for a more detailed assessment of the stresses and injury progression to be evaluated. It also allows for the effect of full or partial disruption of the nerve roots to be investigated. Clinical patterns of brachial plexus injury and some experimental work demonstrate that C5 and C6 experience higher stress under initial loading of the brachial plexus than do the lower roots, and that these levels are damaged first (6). This simulation confirms this outcome.

While two three-dimensional models of the adult brachial plexus have been published (67,68), they are anatomically accurate only through the level of the trunks. This is the first 3D model of the complete brachial plexus, for either neonates or adults, which extends through the distal branches. This complete computational model will allow further research to be conducted to evaluate brachial plexus injuries and identify the location of stress values that reach or exceed the experimentally-determined injury threshold limit. Simulation of brachial plexus injuries (Erb's Palsy, Klumpke's Palsy, etc.) can be conducted by severing the nerve roots and analyzing the stress and displacement values throughout the plexus. Further simulation analysis is ongoing for a better understanding of the stress distribution within the nerves that occurs during the birthing process.

When it comes to research related to human neonatal nerves, significant challenges exist. These stem from the fact one cannot conduct an analysis of living nerves, while cadaveric nerves are not an appropriate surrogate due to a change in their mechanical properties postmortem. Finite element modeling allows research to be conducted when mechanical properties and dimensions are known, while we acknowledge all models have limitations that must be considered when framing and evaluating the results.

In this study, the first limitation is due to the lack of values for the mechanical properties of the human neonatal brachial plexus and spinal cord. The use of properties from the brachial plexus of neonatal piglets provides a level of confidence due to the similarity in their size and microstructure, as well as the match between the anatomy and age of the subject. Similarly, the complete dimensions of a human infant's brachial plexus have not been documented. However, by combining the clinically measured dimensions of the roots and trunks with data from both imaging studies of an infant's brachial plexus and more complete dimensions measured through dissection of an adult brachial plexus, we are confident that we have constructed an accurate representation of a neonatal brachial plexus.

Of course, there is no single value for the mechanical properties nor a single set of anatomical dimensions for the human infant brachial plexus that applies across the population. When the model is used to investigate NBPP mechanisms, it will be possible to evaluate the effect of normal variations in the mechanical properties and anatomy of the nerve. However, the model as currently constructed demonstrates its value for the investigation of how various forces or displacements result in stress within the complex geometry of the plexus – and how these stresses may be indicative of injury risk.

For the first time, an anatomically accurate model of the human brachial plexus, in this case of a neonate, has been developed to include the nerve roots through the distal nerve branches. That model has also been validated using the limited experimental and clinical data available – demonstrating that: 1) in comparison with the behavior of the piglet brachial plexus, reasonable levels of applied force will cause failure-inducing levels of stress; 2) the variation in maximum stress between the five nerve roots mirrors what has been seen clinically and in cadaveric studies with respect to injury patterns; and 3) the pattern of stress along the length of the plexus aligns with the variations in strength (failure stress) that has been measured experimentally for the plexus.

Acknowledgments

We dedicate our research to the late Dr. Lynda Yang. We thank our colleagues from the University of Michigan who provided insight and expertise that assisted the research and data collected.

Funding

This research was funded through the National Science Foundation (NSF) Award CBET 2028474.

Chapter 8: Analysis of Biomechanical injury Using a Finite Element model of the Neonatal Brachial Plexus

Introduction

An anatomically appropriate finite element model (FEM) of the neonatal brachial plexus was developed and validated in Chapter 7. This model will allow in-depth analysis of NBPP injuries by providing a better understanding of stress distribution within the nerves. The first application of this model will be to investigate the progression of NBPP within the complex structure of the brachial plexus. This will be done by simulating commonly occurring patterns of brachial plexus injuries (e.g., Erb's Palsy, Klumpke's Palsy, etc.) and evaluating how these patterns affect stress in the nerve roots that remain intact. This will allow the study of the forces applied and their effects on brachial plexus injuries. Thus, the objectives presented in this chapter are to (1) simulate different NBPP injuries that can occur, including C5 injury, Erb's Palsy, and Klumpke's Palsy; and (2) analyze the stress and displacement that occurs throughout the plexus when these injuries occur.

Methodology

The development and validation of this model have been discussed in **Chapter 7.** The model includes a portion of the spinal cord and all five sections of the plexus including roots, trunks, divisions, cords, and terminal branches **(Figure 30).**

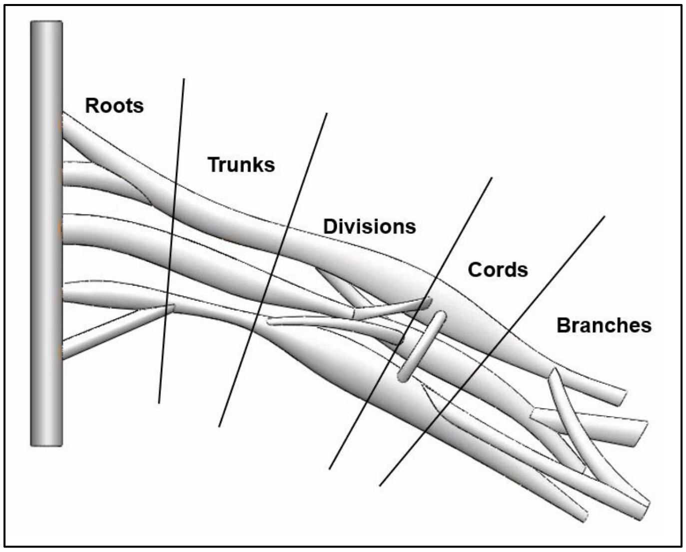

Figure 30: Validated anatomically-appropriate finite element model comprised of all five sections of the brachial plexus – roots, trunks, divisions, cords, and terminal branches. This model is the first known model of the brachial plexus – neonatal or adult - to contain all five sections, including the anterior and posterior divisions.

Simulation of Brachial Plexus Injuries

Previously published injury threshold values were used within this paper to analyze when the stress increases above the threshold to conclude an injury would likely occur (6) **(Table 26)**. After the application of a load to the distal nerve branches was simulated, the stress within all five sections of the plexus were analyzed.

Table 26: Experimentally measured injury threshold values at three locations – roots, cords, and terminal branches.

Injury Locations	Roots	Cords	Terminal Branches
Stress Values [MPa]	0.22	0.49	0.98

The model was previously validated by conducting analysis to represent the level of force needed to cause an injury to the C5 nerve root for both loading cases (0.01 and 10 mm/sec). In case one, a tensile force value of 1.45 N equally distributed over the nerve branches was used to cause a localized stress value of 0.223 MPa in the C5 nerve root – above the injury threshold value of 0.22 MPa. In case two, a tensile force value of 3.20 N was used to cause a stress value of 0.50 MPa – above the injury threshold value of 0.45 MPa. These force values were used as the starting point in analyzing simulated injuries through the finite element model of the neonatal brachial plexus. Common neonatal brachial plexus injuries including, C5 injury, Erb's Palsy, and Klumpke's Palsy, were simulated through the model to analyze stress and displacement changes along the entire plexus. These simulations can be seen in **Figure 31.**

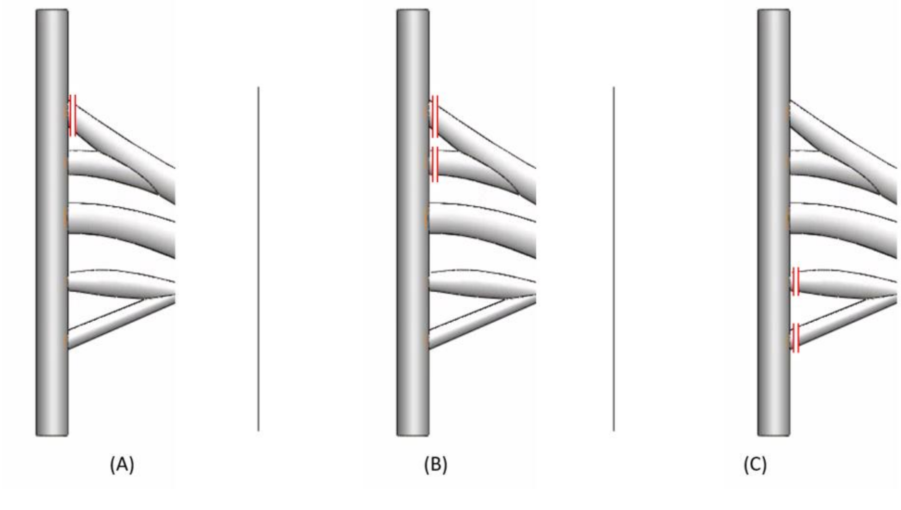

Figure 31: Simulated injuries to the neonatal brachial plexus FEM. Simulation of (A) C5 injury; (B) Erb's Palsy; and (C) Klumpke's Palsy. Erb's palsy occurs when the C5 and C6 nerve roots are both injured, while Klumpke's Palsy occurs when the C8 and T1 nerve root is injured. Note that the full model was used for this simulation – but this figure only shows the region of the nerve roots.

Results

Control – No Injury Simulated

A tensile force of 1.45 N was used to analyze the stress along the plexus of the non-injured model. The analyzed stress at C5 was 0.223 MPa. This value is above the injury threshold value (0.22 MPa) at the nerve roots, and one would conclude an injury is likely to occur to this portion of the plexus. The stress at the lower roots (C6-T1) were below the injury threshold value **(Table 25).**

Table 27: Stress value with a force of 1.45 N when no injury was induced within the FEM.

Stress values using a force value of 1.45 N					
Injury Locations	**C5**	**C6**	**C7**	**C8**	**T1**
Stress Values [MPa]	0.223	0.135	0.178	0.170	0.115

Simulated C5 Injury

The first injury simulation involved severing the C5 nerve root, reflecting a rupture or avulsion of that nerve root at the connection with the spinal cord **(Figure 31.A)**. Once the C5 nerve root was severed, a force of 1.45 N was distributed equally to the five terminal nerve endings to analyze the change of stress in comparison to the non-injured model. Using the control level of force (1.45 N), the stress at C6 increased by 31% to a value of 0.1775 MPa within the simulated C5 injury model **(Table 25).** While this value is below the injury threshold value one would assume that if a force continues to be applied and increases in magnitude, an injury is still possible.

Since the force value of 1.45 N predicted a stress at the C6 nerve root to be below the injury threshold value – the force value was increased until the C6 nerve root stress value surpassed the stress value of 0.22 MPa **(Table 25).** An increase in force of 25% to 1.80 N causes a stress value of 0.2203 MPa – above the injury threshold value. While 25% might seem to be a large jump, this is in reality a minuscule increase of 0.07 N of applied tensile force to each terminal nerve branch (0.35 N of additional force distributed across 5 terminal branches).

Table 28: Analyzing the maximum stress [MPa] at the C6 nerve root for distributed force levels ranging from the control value to a value where it reaches the established injury threshold. In this case, the force needed to cause the stress value to increase above the injury threshold value of 0.22 MPa was 1.80 N.

Applied Force [N]	**1.45**	**1.50**	**1.60**	**1.70**	**1.80**
Maximum Stress at C6 [MPa]	0.1775	0.1836	0.1958	0.2035	0.2203

The change of stress was analyzed for the remaining roots (C7-T1) using the tensile force value of 1.80 N **(Table 26)**. With this amount of force, one would conclude an injury to the C6 nerve root would occur, as the stress value analyzed was 0.2203 MPa – above the injury threshold value. The results also show the value of C7 to be above the injury threshold value. In this case, we would conclude injury would progress through the C6 and C7 nerve roots. While C8 is slightly (0.8 MPa) below the threshold value, one must remember that variations exist within the nerve complex depending on the subject. Thus, in this model, if the thickness (diameter) of the C8 nerve root is slightly smaller than in the model, the C8 nerve root may become injured as well. A visual representation of the stress distribution with a brachial plexus in which a C5 injury was induced can be seen in **Figure 32. Figure 33** illustrates the location of the maximum stress for each nerve root – where the maximum stress for C6-C8 was at the inferior portion of the nerve roots, while the maximum stress for the T1 nerve root was superior.

Table 29: The maximum stress value of each nerve root analyzed with a force of 1.80 N when a C5 injury is created within the FEM.

Stress values using a force value of 1.80 N					
Injury Location	**C5**	**C6**	**C7**	**C8**	**T1**
Maximum Stress [MPa]	0	0.2203	0.2277	0.2192	0.1463

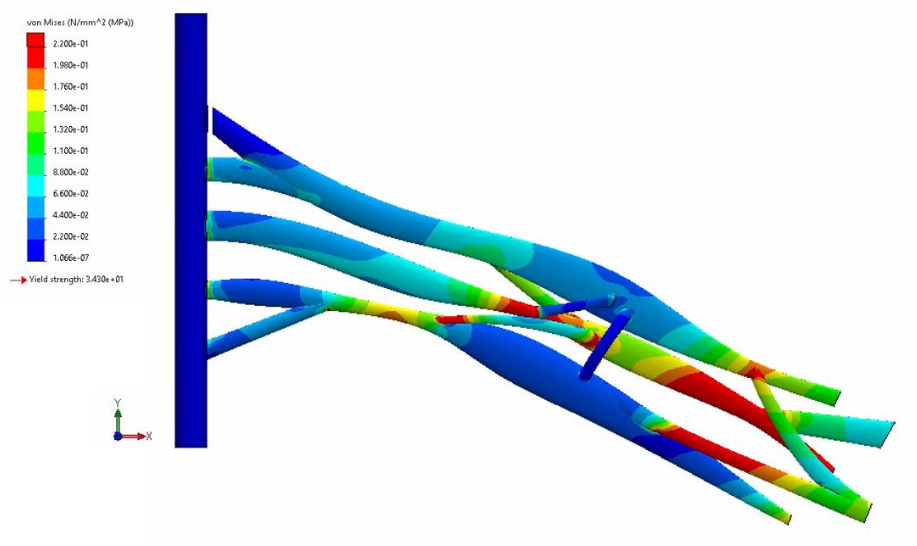

Figure 32: Simulated C5 injury of the FEM portraying the stress distribution when a tensile force of 1.80 N was applied perpendicularly to the five terminal nerve endings. Note the distal portions of the plexus have larger injury threshold values in comparison to the roots.

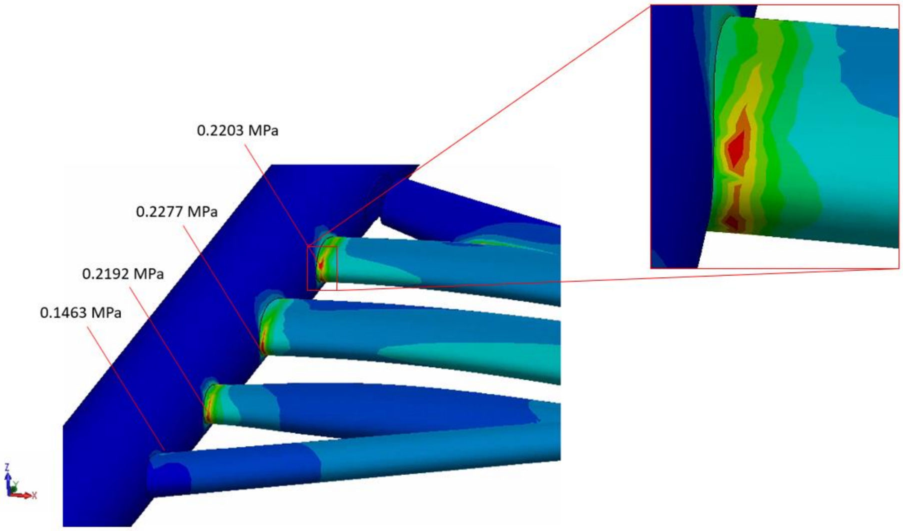

Figure 33: Von Mises stress analysis on a neonatal brachial plexus model with a C5 injury where red depicts stress values greater than 0.22 MPa. In this case, C6 and C7 show stress that has increased to a value above the roots' injury threshold, resulting in a likely injury to the nerve roots.

Simulation of Erb's Palsy

Erb's palsy is a common NBPP injury that occurs when C5 and C6 are injured, with an avulsion or rupture if the injury is permanent. Once the C5 and C6 nerve roots were severed in the computational model, the stress value of C7 was analyzed with a tensile force value of 1.45 N applied to the nerve endings **(Figure 31.B).** The stress value of C7 of 0.452 MPa was predicted – showing the progression of injury would most likely continue down to C7 if force continued to be applied to the neonate.

Using a force value of 1.45 N showed a stress value of the next nerve root (C7) of over double the injury threshold. Thus, the applied force value was reduced to depict the minimum force value needed to still cause the injury to progress to the C7 nerve root. A tensile force of 1.2 N is needed to initiate an injury-causing stress value of 0.2382 MPa **(Table 27).** In comparison to the control model, the necessary applied force value decreased by 16% – showing that less force is needed to cause the injury progress and involve C7 after an Erb's Palsy has occurred.

Table 30: Stress value with a force of 1.20 N when Erb's Palsy is induced within the FEM.

Stress values using a force value of 1.20 N					
Injury Location	**C5**	**C6**	**C7**	**C8**	**T1**
Maximum Stress [MPa]	0	0	0.2382	0.1906	0.1337

Simulation of Klumpke's Palsy

Klumpke's Palsy can also occur during the birthing process and is an injury causing the C8 and T1 nerve roots to become injured. Generally, this injury occurs when the arm is abducted, and so is more commonly related to a breech presentation (1). Once the two lower nerve roots were severed within the computational model, the stress within the upper nerve roots was analyzed **(Figure 31.C).** A force of only 1 N was needed to initiate an injury-causing stress value at the C5 nerve root. The stress values for the upper three nerve roots (C5-C7) were 0.2382 MPa, 0.1482 MPa, and 0.1842 MPa, respectively.

The force value needed to develop an injury-causing stress level to the C5 nerve root following a previous Klumpke's palsy pattern of injury was 45% lower than in the control model. In this case, C5 stress value increased above the injury threshold value by 8% - while C6 and C7 stayed below the threshold.

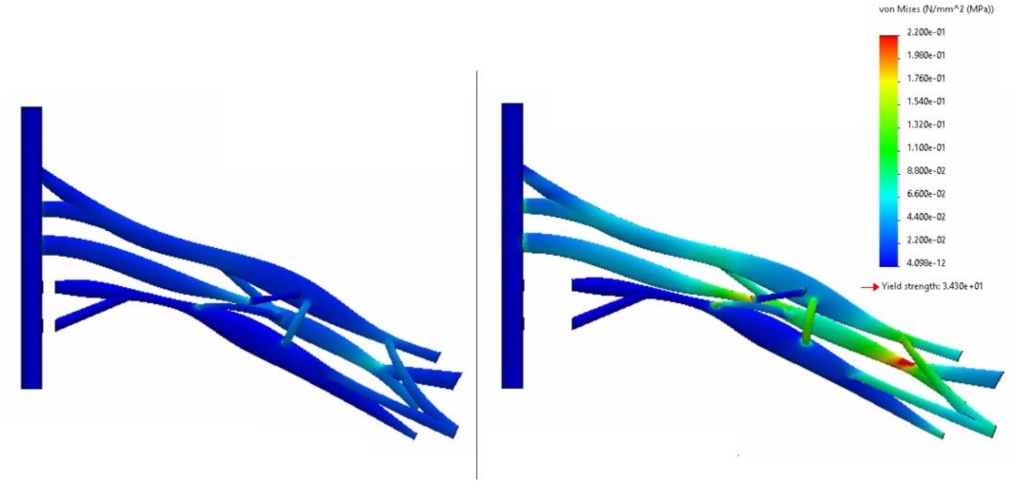

Figure 34: Simulation of a Klumpke injury where C8 and T1 nerve roots are severed near the spinal cord. The maximum stress at the inferior portion of the C5 nerve root increased above the injury threshold value to 0.238 MPa.

Discussion

The benefit of this novel, complex brachial plexus model, is that it was developed through known neonatal and adult dimensions and ratios, allowing for an anatomically appropriate model to be constructed. While the model was created using plexus dimensional ratios from a single subject – a cadaveric male – variations in the dimensions between subjects is expected to occur, including the angles, lengths, and thicknesses of the nerve segments. A change in anatomical structure will come with a change in stress values, which may make one brachial plexus more susceptible to injury than another. More significant anatomical differences may also occur when it comes to individual patients. For example, when conducting the cadaveric dissection, one specimen's brachial plexus T1 nerve root connected directly to the lower cord, completely bypassing the lower trunk and division. This anatomical variation will change the stress distribution along the plexus and possibly the pattern of injury that occurs to the plexus.

The analysis conducted with the use of this novel three-dimensional model is the first to discuss the change in the stress within the complete brachial plexus that is likely to occur as an injury is initiated and progresses during the birthing process. This pattern of stress progression when a nerve root is injured may be more obvious in an engineer's eyes than a clinician, as engineers are taught in-depth the mathematical relationships that apply to force and stress analysis in both simple and complex structures. From a clinician's point of view, this model allows a visual representation of the localized points of higher stress within the entire plexus and how those change as failure at each nerve root occurs. When combined with a fetal model, this analysis will also offer insight into the amount of applied force that may cause an injury – and this value may then subsequently be used for medical professionals' training regarding the effect that various types and directions of force have on patients.

The current model portrays the nerves in their natural orientation expected when the arm would be placed by the patient's side during birth with no bending of the neck. One goal in future iterations of this model is to combine the brachial plexus within a simplified fetus model to allow for variations of the model to include anatomical positions of the fetus. These anatomical positions may include an abducted arm and bending of the fetus' neck. When Klumpke's palsy occurs in a patient, in general the arm will have been abducted away from the body at the time of the injury. The current model in combination with a simplified fetus model would allow Klumpke's palsy injury to be analyzed both visually with an abducted arm and in relation to the stress distribution that occurs when force is applied.

When it comes to developing a biological computational model, significant challenges exist. A limitation in simulating the effect and progression of specific brachial plexus injuries includes the fact that it does not represent the true, gradual injury phenomenon that occurs clinically. Instead, the nerves are severed and then loads are applied to investigate the effect of that injury. A more accurate representation of these injuries may occur if the model was able to simulate a force and, once the stress value goes above the injury threshold value, the "injured" element is eliminated while the force continues to be applied. Advancements in the model's properties and the software used are needed before this approach can be pursued. Overall, the analysis of these injury iterations is the first step in describing what changes in stress occur when various forces are applied to the plexus. This model may be of use to neurosurgeons, researchers, and other medical professionals in describing what portion of the plexus may be injured and what specific orientation of the baby may have influenced the occurrence of the injury.

Chapter 9: Future Work and the Advancements of Computational Modeling of the Neonatal Brachial Plexus

Introduction

The advancements of computational modeling of biological tissues have greatly improved over previous decades. Macro-level advancements have occurred with the development of whole-body FE models for injury predictions in motor accidents. Micro-level advancements in organ and tissue models have also been occurring more recently, including modeling of articular cartilage layers, tumors, nerves, etc. As stated in previous chapters, the difficulty of finite element analysis and running complex non-linear analysis of nerves includes the inability to collect material properties from living tissue, and the fact that cadaveric tissue does not accurately mimic living tissue. Modeling viscoelastic material is one of the most difficult tasks in dynamic finite element analysis (FEA), as there are no universal guidelines in the development process [53]. The objective of this final chapter is to (1) explain the limitations of running a lateroflexion simulation with the current model; and (2) explain the process that has occurred in the start of using nonlinear, viscoelastic materials within an analysis. In addition, future directions for computational modeling of NBPP will be discussed.

Simulation of Lateroflexion of the Spinal Cord

The original, non-injured model **(Chapter 7)** was used to simulate lateroflexion of the infant's neck. During the birthing process – due to the clinician's applied force – the fetus' neck can be bent away from the anterior shoulder. While this direction of force application is contraindicated in the case of a shoulder dystocia (87), it is a known way in which a brachial plexus injury can occur. The goal of this simulation was to analyze the maximum amount of force needed to cause a stress value above the injury threshold value.

Methods of Lateroflexion Simulation

The model was run as a static analysis using a linear elastic isotropic material. The material properties can be seen above in **Chapter 7 – Table 23.** Boundary conditions within this simulation included fixing the five terminal nerve endings, as well as the bottom edge of the spinal cord. The five terminal nerve endings were fixed to replicate a neonate's shoulder in a stand-still position while only the head was flexed away from the anterior shoulder. The objective of fixing the distal portion of the spinal cord was to mimic the stability the spinal cord has while encased within the vertebral canal. A shear force was applied to the top plane of the spinal cord to represent the pulling of the neck away from the anterior shoulder.

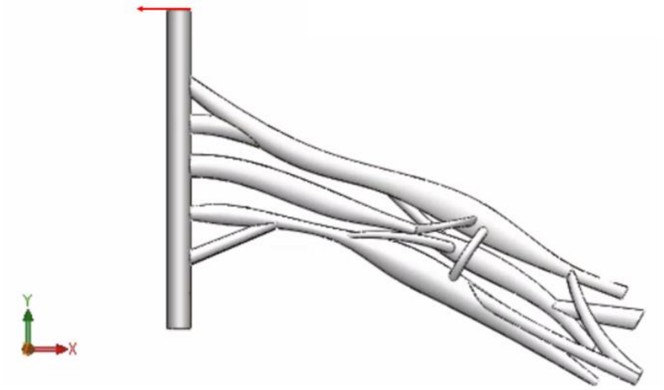

Figure 35: Loading condition placed on the superior cross-sectional face of the spinal cord. The force was applied as a shear force in the -x direction away from what would be the anterior shoulder of the fetus.

Lateroflexion Results and Conclusion

A shear force of 0.02 N was applied on the top plane of the spinal cord as seen in **Figure 35.** While the majority of the stress stayed well below the injury threshold value, a high localized stress occurred at the superior portion of the C5 nerve root. The maximum localized stress at this location was 0.311 MPa – well above the injury threshold value of 0.22 MPa.

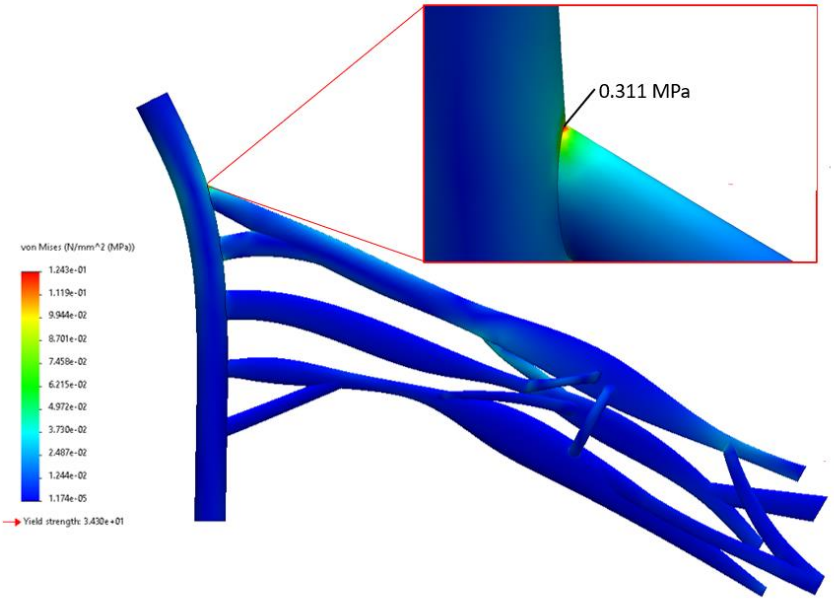

Figure 36: Von Mises stress results of lateroflexion of the spinal cord.

The miniscule amount of force needed to cause an injury to the C5 nerve root in this simulation should be questioned due to the limitations that surrounded the development and analysis of the model. The biggest limitation within this simulation is the inability to create boundary conditions that replicate the effect of the vertebral column. If the brachial plexus model was in combination with a spine model, extra stability would occur. Thus, it was determined that it was not appropriate at this time to investigate lateroflexion using the model in its current form.

Nonlinear Computational Modeling of Nerves

It is known that many materials in the real world are nonlinear and inelastic. The model seen in **Chapter 7 and 8** was analyzed with the plexus defined as a linear elastic material. Within finite element modeling, linear elastic constitutive equations are the most widely used to represent a solid material that is subjected to infinitesimal strain (88). A linear elastic material can be fully characterized by the two physical constants known as Young's Modulus and Poisson's ratio (89). When it comes to analyzing an isotropic, nonlinear elastic material, it cannot be represented by the two properties mentioned above – but instead is described by parameters that are scalar functions of the deformation. The complexity of FE nonlinear analysis is far too in-depth for a single chapter. The takeaway, however, is to recognize that there is an in-depth numerical method solving engineering and physics equations within computational modeling software, and these processes often pit the complexities of an accurately described material and structure against the goal of obtaining a solution in a reasonable period of time. While the overview of the modeling process involves developing boundary conditions, geometry, loading, and material properties, the overall goal is to develop a realistic model to reduce the need for physical prototypes. Thus, simplifications of material properties, such as used in **Chapters 6 and 7**, and simplified geometry, as seen in **Chapter 6**, are often pursued in FE modeling in order to begin the process of answering relevant questions.

It was recognized that while complex geometry was used in the 3D model, using linear elastic properties limited the accuracy of the model – especially in terms of deformation. The possibility of expanding the model to nonlinear properties was investigated. To begin the development and analysis of a nonlinear simulation, one needs appropriate material properties. These properties may represent a non-linear stress-strain response of a nonlinear elastic material, the time-dependent response of a viscoelastic material, or the directionally dependent properties of an anisotropic material – or some combination of these. As the next step in the model development, nonlinear elastic properties were considered.

As stated in previous chapters, the ability to analyze living neonatal nerves is impossible. When it comes to running an analysis with nonlinear elastic properties, the following material properties are needed: Poisson’s ratio, mass density, tensile strength, and a stress-strain curve. For our analysis, Poisson’s ratio and tensile strength was taken for piglet spinal cords (6). A bilinear depiction of Young‘s Modulus (stress-strain curve) was developed using known material property values of neonatal piglets **(Table 24)** in comparison to a stress-strain curve developed for the behavior of rabbit tibia nerves **(Figure 37)**(90). This bilinear model includes the important” toe” region that represents significant extension – typically through straightening of crimpled portions of the tissue – at low levels of applied stress.

Table 31: Material properties used to conduct nonlinear analysis in brachial plexus.

Material Properties	
Model Type	Nonlinear Elastic
Poisson’s Ratio	0.4
Mass Density $[kg/m^3]$	1000
Tensile Strength $[N/mm^2]$	0.22

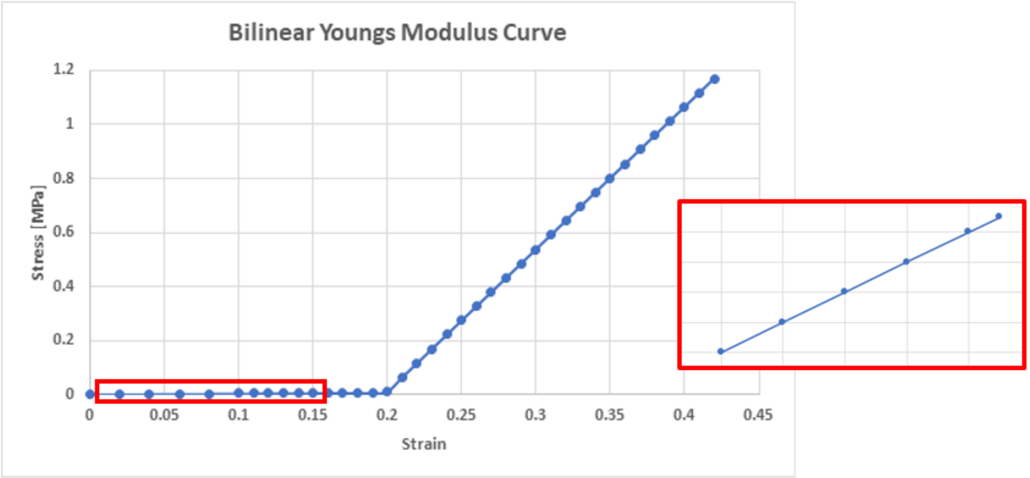

Figure 37: Bilinear Young’s modulus graph developed based off of known neonatal piglet linear modulus values and experimentally determined stress-strain curve for rabbit tibial nerve.

The objective of conducting an analysis of the brachial plexus using nonlinear elastic properties is to more accurately predict the deformation. This will provide a second set of experimental data (deformation or strain) that can be used for validation of the model. It will also be important if the stresses within the brachial plexus are caused by displacement – such as widening of the angle between the shoulder and the neck – rather than by an applied force. SolidWorks Simulation software was used to run nonlinear analysis of different portions of the brachial plexus. In order to build this model in 3D with nonlinear properties, a series of increasingly complex portions of the model were analyzed. These three models included: (1) a simple C5 nerve root; (2) C5 and C6 nerve root junction; and (3) all five nerve roots connected to the three trunks.

Non-Linear Results and Conclusion

Figure 38 illustrates a single nerve root (C5) where the medial cross-sectional face of the nerve root was fixed, and a tensile force of 0.25 N was applied perpendicular to the lateral cross-sectional face. Once the simulation was completed, the stress at certain time steps was analyzed – each time step represented 0.01 seconds. **Figure 38** describes three steps in the analysis (2, 39, and 122) and the maximum stress that coincides with each time point. The maximum stress seen within steps 1-122 can be seen in a graphical representation in **Figure 39.**

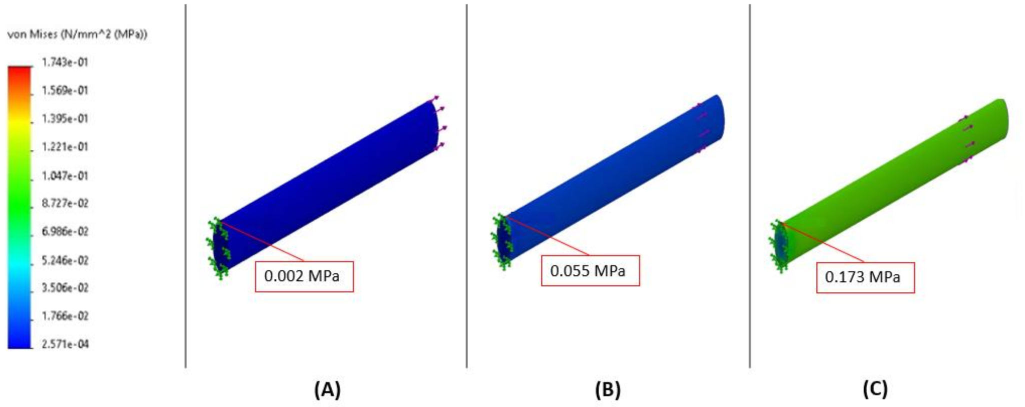

Figure 38: Nonlinear stress analysis results of a single C5 nerve root. Figure (A) illustrates step 2 at the time point of 0.0125 seconds with a maximum stress of 0.002 MPa; (B) step 39 at time of 0.17 seconds with a maximum stress of 0.055 MPa; and (C) step 122 at a time point of 0.99 seconds with a maximum stress of 0.173 MPa.

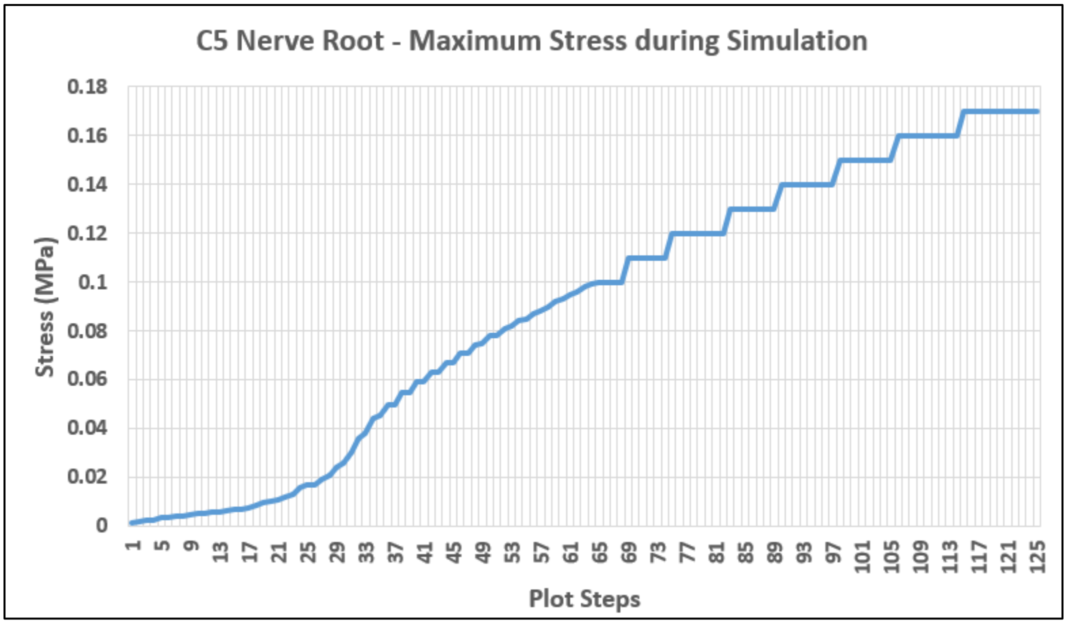

Figure 39: Graphical representation of the effect of 0.25 N of tensile force has on the maximum stress seen in a single nerve root modeled with the bilinear properties shown in Figure 34.

A C5 and C6 nerve root junction was designed and analyzed to see the effect of tensile force has on the change of stress within this more complex structure. Within this simulation, the medial cross-sectional face of each of the two-nerve roots was fixed, and a tensile force of 0.25 N was applied perpendicular to the lateral cross-sectional face. The maximum stress at step 100 was located at the inferior portion of the C5 cross-sectional face and had a value of 0.1672 MPa. For this model, 100 steps represented 1 second of model simulation.

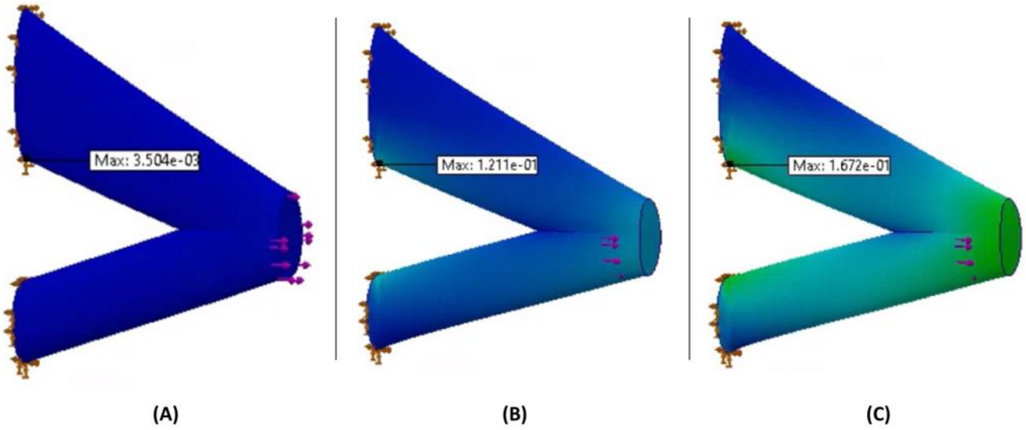

Figure 40: Non-linear stress analysis of C5 and C6 nerve roots at three different plot steps: 0, 50, and 100. Each plot step corresponds with 0.01 seconds of force being applied to the model.

The last nonlinear analysis conducted was for the spinal cord and the first two sections of the brachial plexus (roots and trunks) **(Figure 41)**. The boundary condition within this analysis included a fixed, encastré condition placed on the spinal cord – the same as in the model described in **Chapter 7**. A tensile force was applied and distributed equally to the three distal cross-sectional faces of the trunks. After an hour and 11 minutes (91 steps representing 0.56 seconds), the model's simulation ended with an error. This error may have occurred due to the available computational power and/or the material properties (stress-strain curve) that were used in the model not being accurate enough.

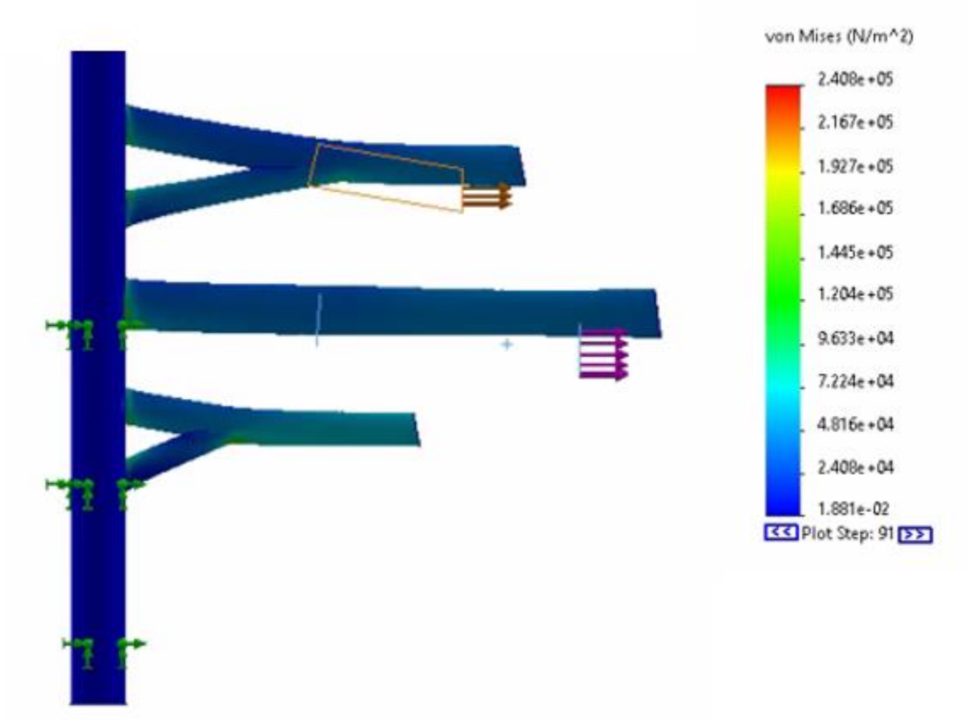

Figure 41: Non-linear analysis of all five roots and three trunks.

While **Figure 38** does not represent the intended length of the test, it does show that more deformation occurred in each of the trunks than in the model discussed in **Chapter 7**. This was expected, due to the inclusion of the toe region in the stress-strain curve. While including nonlinear properties is an eventual goal for this model, it was determined to be beyond the scope of this dissertation. The computational power needed to model the full plexus with non-linear properties is expected to be significant.

Advancements in Biomechanical Engineering and Computational Modeling

The primary objective of this project was to develop and validate a novel, 3D model of the neonatal brachial plexus that can then be used to investigate the occurrence of NBPP. Meeting this objective is a significant contribution to the field of biomedical engineering, as no complex model of a neonatal plexus previously existed. Throughout the development process of this model, dozens of prototype models were developed, analyzed, and discarded. The beginning prototypes were developed based on inaccurate dimensions, using a variety of material properties, and many different mesh types. The model was refined and polished to present the model seen in the above chapters – this 3D model is the first known complete, anatomically appropriate model developed of all five sections of the plexus. As discussed in **Chapter 3**, two 3D models previously were developed based on adult anatomy dimensions (67,68); however, neither of those showed the anatomical complexity beyond the level of the trunks.

In addition to the advancement in modeling, this project has also added to other bodies of knowledge. Biomedical engineering is a multidisciplinary field that combines the general principles of engineering, biological science, and aspects of human health. This research and the development of this computational model have contributed to the field of biomedical engineering in several ways, including:

1. **Contribute to academic knowledge:** The collaboration with the University of Michigan's Neurosurgery Department has advanced the knowledge of known dimensions of the complete adult brachial plexus. While there are many drawings available of the brachial plexus in anatomy atlases, to date there has been no publication that specifies the adult brachial plexus dimensions. By combining the full set of adult measurements with the unique average infant dimensions, also from the University of Michigan, a set of anatomically appropriate neonatal dimensions have been obtained. This can now serve as the basis of parametric analysis related to how anatomy of the plexus might affect the occurrence of NBPP.
2. **Improved Understanding of Nerve Injuries:** This brachial plexus model has enhanced our understanding of the mechanisms of injury in NBPP by providing a means to investigate how applied force generates tissue-level within the complete plexus. As a first analysis, this model demonstrates to neurosurgeons how NBPP can progress along the plexus when force is applied. Understanding the injury mechanism and its progression is

key to attempts that might focus on improving reconstructive surgical approaches or other therapies to address this injury when it does occur.

Further Research and Development

While this model is the first complex model developed on this biological structure –of a neural plexus, advancements of the model can occur in the future. In addition to identifying an appropriate way to include the nonlinear material properties of the tissue in the analysis, the following are potential future steps for this work:

1. Addition of the cervical spine including both vertebral bodies and intervertebral discs.
2. Integrate the developed neonatal brachial model into a simplified fetal model where the fetal model includes head, neck, torso, arms, and legs.
3. Lastly, in combination with the two steps stated above, integrate this complex model with developed pelvic and uterus models to simulate the birthing process.

This model could also lead to more sophisticated models that target more specific injuries or semi-personalized models that might be used to forensically assess a particular infant.

BIBLIOGRAPHY

1. Gherman RB, Chauhan SP, Clark SL, Gonik B, Grimm MJ, Grobman WA, et al. Neonatal brachial plexus palsy. Vol. 123, Obstetrics and Gynecology. American College of Obstetrician and Gynecologists; 2014. 902–904 p.
2. Crothers B, Boston MCP. OBSTETRICAL INJURIES OF THE SPINAL CORD' [Internet]. Available from: http://journals.lww.com/md-journal
3. Allen R, Sorab J, Gonik B. Risk factors for shoulder dystocia_ an engineering study of clinician-applied forces - PubMed.
4. Kawai H, Ohta I, Masatomi T, Kawabata H, Masada K, Ono K. Stretching of the brachial plexus in rabbits. Acta Orthop. 1989;60(6):635–8.
5. Kawai H, Kawabata H, Masada K, Ono K, Yamamoto K, Tsuyuguchi Y, et al. Nerve repairs for traumatic brachial plexus palsy with root avulsion.
6. Singh A, Shaji S, Delivoria-Papadopoulos M, Balasubramanian S. Biomechanical Responses of Neonatal Brachial Plexus to Mechanical Stretch. J Brachial Plex Peripher Nerve Inj. 2018;13(1):e8–14.
7. Bayot ML, Elzeftawy E. Anatomy, Shoulder and Upper Limb, Brachial Plexus [Internet]. StatPearls. 2018. Available from: http://www.ncbi.nlm.nih.gov/pubmed/29763192
8. Ferrante MA. Electrodiagnostic assessment of the brachial plexus. Neurol Clin [Internet]. 2012;30(2):551–80. Available from: http://dx.doi.org/10.1016/j.ncl.2011.12.005
9. Desai S, Varacallo Matthew. Anatomy, Shoulder and Upper Limb, Musculocutaneous Nerve. StatPearls [Internet] [Internet]. 2021; Available from: https://www.ncbi.nlm.nih.gov/books/NBK534199/
10. Leechavengvongs S, Teerawutthichaikit T, Witoonchart K, Uerpairojkit C, Malungpaishrope K, Suppauksorn S, et al. Surgical anatomy of the axillary nerve branches to the deltoid muscle. Clinical Anatomy. 2015 Jan 1;28(1):118–22.
11. Polatsch DB, Melone CP, Beldner S, Incorvaia A. Ulnar Nerve Anatomy. Vol. 23, Hand Clinics. 2007. p. 283–9.
12. Schuenke M, Schulte E, Schumacher U. Atlas of Anatomy. Third. Gilroy A, MacPherson B, editors. Thieme; 2016.
13. Gilcrease-Garcia BM, Deshmukh SD, Parsons MS. Anatomy, imaging, and pathologic conditions of the brachial plexus. Radiographics. 2020 Oct 1;40(6):1686–714.
14. Fessler R, Sekhar L. Atlas of Neurosurgical Techniques. Thieme; 2016.
15. Merriam-Webster [Internet]. [cited 2022 Aug 23]. Dorsal root ganglion. Available from: https://www.merriamwebster.com/dictionary/dorsal%20root%20ganglion#:~:text=dorsal%20root%20ganglion%20noun%20plural%20dorsal%20root%20ganglia,distinct%20rash%20localized%20to%20a%20single%20dermatome%20ensues.
16. Waxenbaum J, Reddy V, Williams C, Futterman B. Anatomy, Back, Lumbar Vertebrae - StatPearls - NCBI Bookshelf. [cited 2023 Aug 21]; Available from: https://www.ncbi.nlm.nih.gov/books/NBK459278/

17. Urschel HC. Anatomy of the Thoracic Outlet. Thorac Surg Clin. 2007 Nov;17(4):511–20.
18. Abzug JM, Kozin SH. Current concepts: neonatal brachial plexus palsy. Orthopedics. 2010 Jun;33(6):430–5.
19. Zafeiriou DI, Psychogiou K. Obstetrical brachial plexus palsy. Pediatr Neurol. 2008 Apr;38(4):235–42.
20. Romaña MC, Rogier A. Obstetrical brachial plexus palsy. Handb Clin Neurol. 2013;112:921–8.
21. Nikolaou S, Liangjun H, Tuttle LJ, Weekley H, Christopher W, Lieber RL, et al. Contribution of denervated muscle to contractures after neonatal brachial plexus injury: not just muscle fibrosis. Muscle Nerve. 2014 Mar;49(3):398–404.
22. O'Berry P, Brown M, Phillips L, Evans SH. Obstetrical Brachial Plexus Palsy. Curr Probl Pediatr Adolesc Health Care. 2017 Jul;47(7):151–5.
23. Abid A. Brachial plexus birth palsy: Management during the first year of life. Vol. 102, Orthopaedics and Traumatology: Surgery and Research. Elsevier Masson SAS; 2016. p. S125–32.
24. Andersen J, Watt J, Olson J, Van Aerde J. Perinatal brachial plexus palsy. Paediatr Child Health. 2006 Feb;11(2):93–100.
25. Heise CO, Martins R, Siqueira M. Neonatal brachial plexus palsy: a permanent challenge. Arq Neuropsiquiatr. 2015 Sep;73(9):803–8.
26. Proctor C, Chavis PS. Horner syndrome. Vol. 33, Journal of Neuro-Ophthalmology. 2013. p. 88–9.
27. Giuffre JL, Kakar S, Bishop AT, Spinner RJ, Shin AY. Current Concepts of the Treatment of Adult Brachial Plexus Injuries. J Hand Surg Am. 2010 Apr;35(4):678–88.
28. Pathomechanics _ definition of pathomechanics by Medical dictionary. [cited 2023 Jul 10]; Available from: https://medical-dictionary.thefreedictionary.com/pathomechanics
29. Pondaag W, Malessy MJA, van Dijk JG, Thomeer RTWM. Natural history of obstetric brachial plexus palsy: a systematic review. Dev Med Child Neurol. 2004 Feb;46(2):138–44.
30. Metaizeau JP, Prevot J, Lascombes P. [Obstetrical paralysis. Spontaneous development and results of early microsurgical treatment]. Ann Pediatr (Paris). 1984 Feb;31(2):93–102.
31. Jolly F. Ueber infantile entbindungslähmungen. Charite Annalen. 1896;
32. Thomas J. Two cases of bilateral birth paralysis of the lower-arm type. Boston Med Surgical . 1905;
33. Chauhan S, Blackwell S, Ananth C. Neonatal Brachial Plexus Palsy: incidence, prevalence, and temporal trends. Semin Perinatol. 2014;38(4):210–8.
34. Gordon M, Rich H, Deutschberger J, Green M. The immediate and long-term outcome of obstetric birth trauma. I. Brachial plexus paralysis. Am J Obstet Gynecol. 1973 Sep 1;117(1):51–6.

35. Turrentine MA, Ramirez MM. Adverse perinatal events and subsequent cesarean rate. Obstetrics and gynecology. 1999 Aug;94(2):185–8.

36. Gherman RB, Ouzounian JG, Goodwin TM. Obstetric maneuvers for shoulder dystocia and associated fetal morbidity. Am J Obstet Gynecol. 1998 Jun;178(6):1126–30.

37. Nocon JJ, McKenzie DK, Thomas LJ, Hansell RS. Shoulder dystocia: an analysis of risks and obstetric maneuvers. Am J Obstet Gynecol. 1993 Jun;168(6 Pt 1):1732–7; discussion 1737-9.

38. Jackson ST, Hoffer MM, Parrish N. Brachial-plexus palsy in the newborn. J Bone Joint Surg Am. 1988 Sep;70(8):1217–20.

39. Waters PM, Bae DS. Brachial Plexus Birth Palsy: Rationale for a Multicenter Prospective Study. Semin Plast Surg. 2004;18(04):377–84.

40. Chauhan SP, Rose CH, Gherman RB, Magann EF, Holland MW, Morrison JC. Brachial plexus injury: a 23-year experience from a tertiary center. Am J Obstet Gynecol. 2005 Jun;192(6):1795–800; discussion 1800-2.

41. Frade F, Gómez-Salgado J, Jacobsohn L, Florindo-Silva F. Rehabilitation of neonatal brachial plexus palsy: Integrative literature review. J Clin Med. 2019 Jul 1;8(7).

42. Kerns J, Piponov H, Helder C, Amirouche F, Solitro G, Gonzalez M. Mechanical Properties of the Human Tibial and Peroneal Nerves Following Stretch With Histological Correlations. Anat Rec (Hoboken). 2019 Nov;302(11):2030–9.

43. Ma Z, Hu S, Tan JS, Myer C, Njus NM, Xia Z. *In vitro* and *in vivo* mechanical properties of human ulnar and median nerves. J Biomed Mater Res A. 2013 Sep 30;101A(9):2718–25.

44. Topp KS, Boyd BS. Structure and Biomechanics of Peripheral Nerves: Nerve Responses to Physical Stresses and Implications for Physical Therapist Practice [Internet]. Vol. 86, Physical Therapy. 2006. Available from: https://academic.oup.com/ptj/article/86/1/92/2805155

45. Kleinrensink GJ, Stoeckart R, Mulder PG, Hoek G, Broek T, Vleeming A, et al. Upper limb tension tests as tools in the diagnosis of nerve and plexus lesions. Anatomical and biomechanical aspects. Clin Biomech (Bristol, Avon). 2000 Jan;15(1):9–14.

46. Millesi H, Zöch G, Reihsner R. Mechanical properties of peripheral nerves. Clin Orthop Relat Res. 1995 May;(314):76–83.

47. Wong YR, Pang X, Lim ZY, Du H, Tay SC, McGrouther DA. Biomechanical evaluation of peripheral nerves after crush injuries. Heliyon. 2019 Apr;5(4):e01557.

48. Marani E, van Leeuwen JL, Spoor CW. The tensile testing machine applied in the study of human nerve rupture: a preliminary study. Clin Neurol Neurosurg. 1993;95:33–5.

49. Millesi H, Zoch G, Reihsner R. Mechanical Properties of Peripheral Nerves. Vol. 314, CLINICAL ORTHOPAEDICS AND RELATED RESEARCH Number. 1995.

50. Grewal R, Xu J, Sotereanos DG, Woo SL. Biomechanical properties of peripheral nerves. Hand Clin. 1996 May;12(2):195–204.

51. Singh A, Magee R, Balasubramanian S. Methods for in vivo biomechanical testing on brachial plexus in neonatal piglets. Journal of Visualized Experiments. 2019;2019(154):1–7.

52. Cleveland Clinic. Nerves [Internet]. [cited 2023 Aug 22]. Available from: https://my.clevelandclinic.org/health/body/22584-nerves

53. Kawai H, Ohta I, Masatomi T, Kawabata H, Masada K, Ono K. Stretching of the brachial plexus in rabbits. Acta Orthop Scand. 1989 Jan 8;60(6):635–8.

54. Kleinrensink GJ, Stoeckart R, Mulder PGH, Hoek G v. d., Broek Th, Vleeming A, et al. Upper limb tension tests as tools in the diagnosis of nerve and plexus lesions. Clinical Biomechanics. 2000 Jan;15(1):9–14.

55. Narakas AO. Lesions found when operating traction injuries of the brachial plexus. Clin Neurol Neurosurg. 1993;95:56–64.

56. Singh A, Magee R, Balasubramanian S. An in Vitro Study to Investigate Biomechanical Responses of Peripheral Nerves in Hypoxic Neonatal Piglets. J Biomech Eng. 2021;143(11):1–4.

57. Zapałowicz K, Radek A. Mechanical properties of the human brachial plexus. Neurol Neurochir Pol. 2000;34(6 Suppl):89–93.

58. Zapałowicz K, Radek A. Experimental investigations of traction injury of the brachial plexus. Model and results. Ann Acad Med Stetin. 2005;51(2):11–4.

59. Kalmin O V. [The structural bases of the tensile strength properties of nerves]. Morfologiia. 1997;111(1):39–43.

60. Gefen Amit. The Pathomechanics of tissue injury and disease and the mechanophysiology of healing. Research Signpost; 2009. 414 p.

61. Sunderland S, Bradley KC. Endoneurial tube shrinkage in the distal segment of a severed nerve. Journal of Comparative Neurology. 1950;93(3):411–20.

62. Lindblom K, Rexed B. SPINAL NERVE INJURY IN DORSO-LATERAL PRO-TRUSIONS OF LUMBAR DISKS.

63. Landesman B, Lopez J. Chapter 11 - Electrodiagnostic Evaluation of Spinal Tumors. In: Tumor of the Spine. 2008. p. 283–97.

64. Verdú E, Ceballos D, Vilches JJ, Navarro X. Influence of aging on peripheral nerve function and regeneration. Journal of the Peripheral Nervous System. 2000 Dec;5(4):191–208.

65. Singhal I, Harinathan B, Warraich A, Purushothaman Y, Budde MD, Yoganandan N, et al. Finite element modeling of the human cervical spinal cord and its applications: A systematic review. Vol. 15, North American Spine Society Journal. Elsevier Inc.; 2023.

66. Cirovic S, Bhola RM, Hose DR, Howard IC, Lawford P V., Marr JE, et al. Computer modelling study of the mechanism of optic nerve injury in blunt trauma. British Journal of Ophthalmology. 2006 Jun;90(6):778–83.

67. Mihara A, Kanchiku T, Nishida N, Tagawa H, Ohgi J, Suzuki H, et al. Biomechanical analysis of brachial plexus injury: Availability of three-dimensional finite element model of the brachial plexus. Exp Ther Med. 2018;15(2):1989–93.

68. Perruisseau-Carrier A, Bahlouli N, Bierry G, Vernet P, Facca S, Liverneaux P. Comparison between isotropic linear-elastic law and isotropic hyperelastic law in the finite element modeling of the brachial plexus. Annales de Chirurgie Plastique Esthetique [Internet]. 2017;62(6):664–8. Available from: http://dx.doi.org/10.1016/j.anplas.2017.03.002

69. Metaizeau JP, Gayet C, Plenat F. [Brachial plexus birth injuries. An experimental study (author's transl)]. Chir Pediatr. 1979;20(3):159–63.

70. Ummu. Nurseship.com. 2021 [cited 2023 Oct 15]. Gravidity & Parity and GTPAL (Explained with Examples). Available from: https://nurseship.com/gtpal-gravidity-parity/

71. Cleveland Clinic Medical Professional. Cleveland Clinic. 2022 [cited 2023 Oct 15]. Apgar Score. Available from: https://my.clevelandclinic.org/health/diagnostics/23094-apgar-score

72. Staff H. Physical Growth in Newborns [Internet]. 2020 [cited 2022 Mar 8]. Available from: https://www.uofmhealth.org/health-library/te6295

73. Mathews T.J, Hamilton B. Mean Age of Mothers is on the Rise: United States, 2000-2014. NCHS Data Bried. 216AD;232.

74. Opinion C. Term and Post term Pregnancy. The American College of Obstetricians and Gynecologist. 2014;20(5):248–51.

75. Gul R, Iqbal S, Anwar Z, Ahdi SG, Ali SH, Pirzada S. Pre-pregnancy maternal BMI as predictor of neonatal birth weight. PLoS One. 2020 Oct 1;15(10 October).

76. Gherman RB, Goodwin TM. Shoulder Dystocia. Curr Opin Obstet Gynecol. 1998;10(6).

77. Doumouchtsis SK, Arulkumaran S. Are all brachial plexus injuries caused by shoulder dystocia? Obstet Gynecol Surv. 2009 Sep;64(9):615–23.

78. Wilson TJ, Chang KWC, Chauhan SP, Yang LJS. Peripartum and neonatal factors associated with the persistence of neonatal brachial plexus palsy at 1 year: A review of 382 cases. J Neurosurg Pediatr. 2016 May 1;17(5):618–24.

79. Narendran LM, Mendez-Figueroa H, Chauhan SP, Folh KL, Grobman WA, Chang K, et al. Predictors of neonatal brachial plexus palsy subsequent to resolution of shoulder dystocia. Journal of Maternal-Fetal and Neonatal Medicine [Internet]. 2021;0(0):1–7. Available from: https://doi.org/10.1080/14767058.2021.1882982

80. Nishida N, Kanchiku T, Ohgi J, Ichihara K, Chen X, Taguchi T. Mechanical properties of nerve roots and rami radiculares isolated from fresh pig spinal cords. Neural Regen Res. 2015;10(11):1869–73.

81. Singh A, Lu Y, Chen C, M Cavanaugh J. Mechanical properties of spinal nerve roots subjected to tension at different strain rates. J Biomech. 2006;39(9):1669–76.

82. Gurewitsch ED, Kim EJ, Yang JH, Outland KE, McDonald MK, Allen RH. Comparing McRoberts' and Rubin's maneuvers for initial management of shoulder dystocia: An objective evaluation. Am J Obstet Gynecol. 2005 Jan;192(1):153–60.

83. Phillips JB, Smit X, De Zoysa N, Afoke A, Brown RA. Peripheral nerves in the rat exhibit localized heterogeneity of tensile properties during limb movement. J Physiol. 2004 Jun 15;557(Pt 3):879–87.

84. Takai S, Dohno H, Watanabe Y, Yoshino N, Ogura T, Hirasawa Y. In situ strain and stress of nerve conduction blocking in the brachial plexus. J Orthop Res. 2002 Nov;20(6):1311–4.

85. Talamini B, Mao Y, Anand L. Progressive damage and rupture in polymers. Cambridge; 2017 May.

86. laconianni J, Balasubramanian S, Grimm M, Gonik B, Singh A. Studying the effects of shoulder dystocia and neonate-focused delivery maneuvers on brachial plexus stretch: a computational study. Submission to Journal of Biomechanical Engineering.

87. Gonik B, Zhang N, Grimm MJ. Prediction of brachial plexus stretching during shoulder dystocia using a computer simulation model. Am J Obstet Gynecol. 2003;189(4):1168–72.

88. Yang KH. Basic Finite Element Method as Applied to Injury Biomechanics. 1st ed. 2017.

89. Mihai LA, Goriely A. How to characterize a nonlinear elastic material? A review on nonlinear constitutive parameters in isotropic finite elasticity. Proceedings of the Royal Society A: Mathematical, Physical and Engineering Sciences. 2017 Nov 29;473(2207):20170607.

90. Rydevik BL, Kwan MK, Myers RR, Brown RA, Triggs KJ, Woo SLY, et al. An in vitro mechanical and histological study of acute stretching on rabbit tibial nerve. Journal of Orthopaedic Research. 1990 Sep;8(5):694–701.

91. ABAQUS. What is a module? [Internet]. [cited 2023 Nov 14]. Available from: https://abaqus-docs.mit.edu/2017/English/SIMACAECAERefMap/simacae-c-topwhatismodule.htm

92. SolidWorks Help. Simulation Toolbar - Fixtures/External Loads [Internet]. [cited 2023 Nov 18]. Available from: https://help.solidworks.com/2021/English/SolidWorks/cworks/c_simulation_toolbar_-_fixtures-external_loads.htm

APPENDIX A: ADDITIONAL INFORMATION REGARDING THE RESEARCH UNDERTAKEN IN THIS DISSERTATION PROJECT.

Table 32: Raw data of the 28 subjects used within Chapter 4.

Within the chart in **Table 32**, six groups were created based on injury location and severity (As stated above in Chapter 4). The values for C5 through T1 are numerically selected 1-5 depending on injury type:

- 1 = Rupture
- 2 = Avulsion
- 3 = Not determined
- 4 = Did not look during surgery
- 5 = Normal – no injury

Deidentified ID Number	C5	C6	C7	C8	T1	Maternal Gravidas	Maternal Age	Maternal BMI [kg/m^2]	Weeks Gestation	Paraterm	birth weight [kg]	Head circumference [cm]	Neonatal Height Length [cm]	Apgar score (1 minute)
SW1	1	1	5	5	5	9	39	NA	37	5	4.92	37.0	50.0	1
SW2	1	1	5	4	4	2	28	48	38	2	3.78	34.0	52.0	5
SW3	1	1	5	5	5	1	24	NA	38	NA	3.91	33.5	49.9	1
SW4	1	1	1	4	4	1	27	NA	37	0	3.47	34.5	49.0	7
SW5	1	1	1	5	5	1	20	26	40	0	3.91	NA	NA	7
SW6	1	1	1	5	5	11	29	42	37	2	3.94	34.3	56.0	7
SW7	1	1	1	5	5	9	28	34	37	6	4.46	35.5	56.0	2
SW8	1	1	1	5	5	2	30	NA	38	1	4.32	34.0	54.6	8
SW9	2	2	1	5	4	5	36	NA	38	3	4.54	NA	55.0	7
SW10	1	2	1	5	5	2	25	NA	40	0	4.66	36.0	55.4	4
SW11	1	2	1	5	5	2	24	NA	40	1	4.74	37.5	57.5	4
SW12	1	2	1	5	5	5	32	NA	38	3	4.19	36.0	52.1	5
SW13	1	2	1	5	5	4	27	NA	39	1	4.47	37.0	51.4	7
SW14	1	1	1	1	4	1	23	NA	39	NA	4.08	NA	54.0	5
SW15	1	1	1	1	1	1	20	NA	40	NA	3.95	NA	NA	6
SW16	1	1	1	1	1	3	27	40	37	1	3.57	NA	NA	2
SW17	1	1	2	1	4	1	22	45	41	NA	3.63	33.0	55.3	4
SW18	1	1	2	1	4	3	-1	NA	41	1	5.31	37.0	55.9	2
SW19	1	1	2	2	2	2	29	NA	38	1	4.51	37.0	52.0	5
SW20	1	1	2	2	1	9	38	NA	38	4	3.55	32.0	53.2	2
SW21	1	1	2	2	2	3	34	45	37	1	3.43	31.0	49.5	2
SW22	1	1	1	2	1	2	20	NA	40	1	3.43	32.0	53.5	2
SW23	1	1	1	2	1	4	37	NA	38	2	4.58	36.0	59.7	7
SW24	2	2	1	1	1	12	39	NA	40	4	3.55	33.7	54.6	6
SW25	1	2	1	1	1	5	25	NA	39	1	4.17	NA	55.0	4
SW26	2	2	2	2	1	2	26	36	39	3	NA	NA	NA	1
SW27	1	2	2	2	1	4	21	NA	39	1	NA	NA	NA	1
SW28	1	2	2	1	1	1	19	NA	39	NA	4.47	25.0	55.0	3

Table 33: Maternal, neonatal, and delivery factors collected but not used in statistical analysis **(Chapter 4)**.

Factors		
Maternal	**Neonatal**	**Delivery**
Age	Number of nerve roots involved	Method of delivery
Race	Avulsions (y/n)	Fetal presentation (vertex/breech/other)
BMI	C5/C6 Avulsion (y/n)	Final route and method of delivery (Vaginal spontaneous/ Vaginal forceps/Vacuum)
Gravidas (para-term/preterm/abortion/living)	Narakas	Station for vacuum or forceps
Diabetes (A1DM/A2DM/pre-pregnancy)	Cate Narakas	Vacuum number of pops off
Hypertension (gestation/pre-pregnancy)	Fetal death in utero	Birthing maneuvers used (McRoberts/Suprapubic/ Wood Screw Rubin/ Zavanelli)
Eclampsia	Biparietal diameter	Posterior Arm Delivery
Previous preterm births	Head circumference	Fundal pressure
Pregnancy resulting from infertility treatment	Abdominal circumference	Traction (gentle/normal/excessive)
Fertility enhancing drugs artificial insemination or intrauterine insemination	Femur Length	
Donor (Ovum/embryo)	USEF (Wg)	
Previous Cesarean birth	Abnormal fetal testing	
Smoking	Membrane Rupture	
Prior history of shoulder dystocia	Meconium	
Steroid Use	Shoulder dystocia (y/n)	
Fibroids	Estimated duration of shoulder dystocia	
Gestation	BMI	
Characteristics of labor and delivery (spontaneous/ ????)	Birthweight	
Cytotec Use	Length	
Cervdil Use	Sex	
Oxytocin Use	APGAR (1min/5min/10min)	
Indication of induction	Plurality (Single/Multiple)	

Table 33 (cont'd)

Factors		
Maternal	**Neonatal**	**Delivery**
Pre-eclampsia	Neonatal Anterior Shoulder (left or right)	
Chorioamnionitis	Anterior or Posterior Injury)	
Episiotomy	Position (OA/OP/LOA/LOP/LOT/ROA/ ROP/ROT/unknown)	
Perineal laceration	Bruising (y/n)	
Amount of blood loss	General composite neonatal morbidities	
Position during delivery (dorsal lithotomy/ squatting/ side/ kneeling)	Abnormal conditions	
Confirmed Sepsis	Assisted ventilation required immediately following delivery	
	Assisted ventilation required for more than six hours	
	NICU admission	

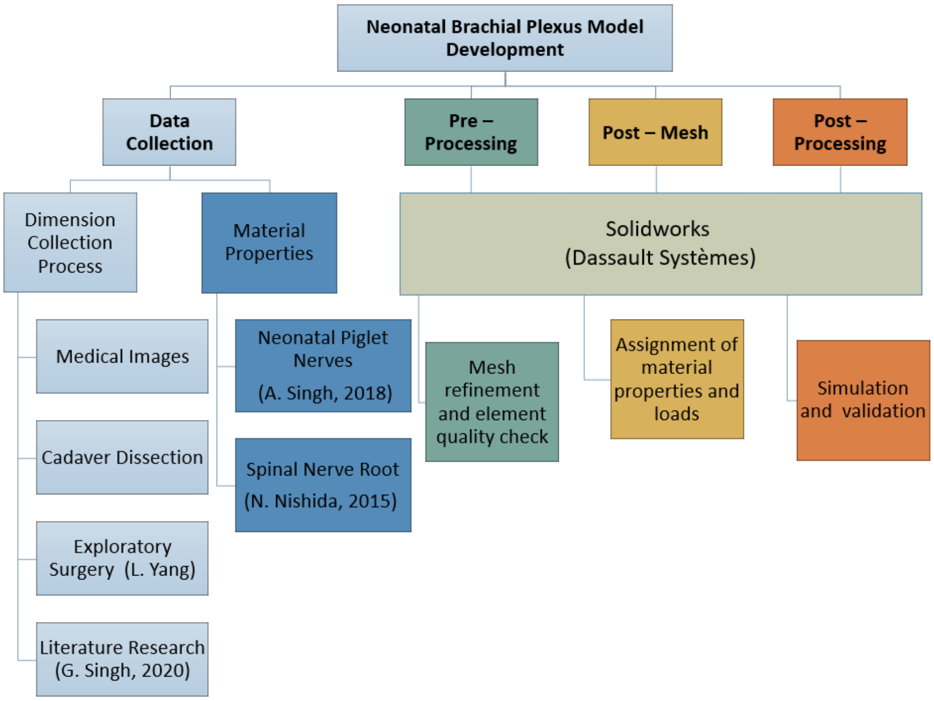

Figure 42: Flow chart describing the steps used to develop the 3D finite element model of the neonatal brachial plexus seen in **Chapters 7 and 8**.

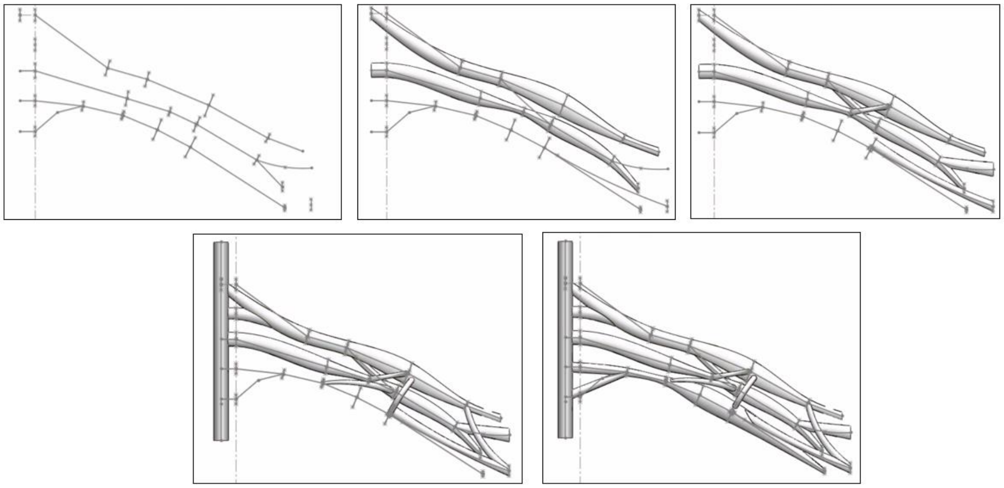

Figure 43: Model development progression through Solidworks Software.

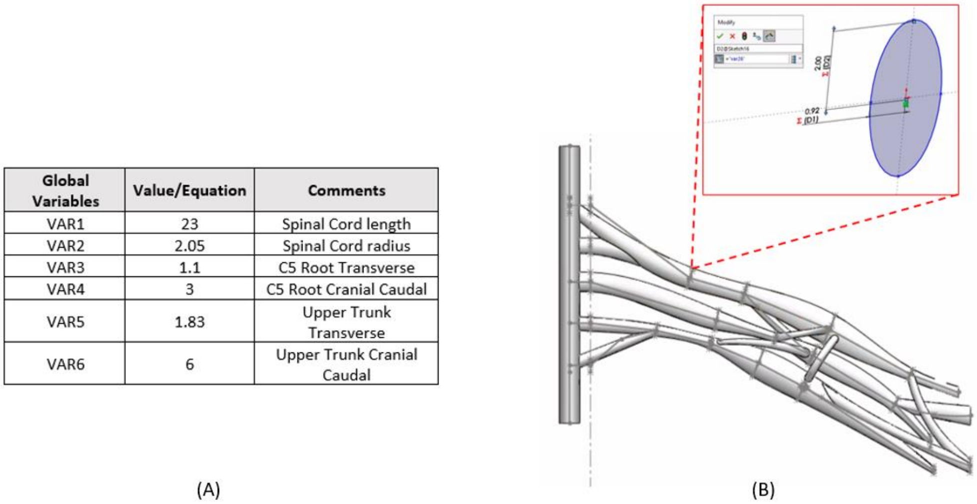

Global Variables	Value/Equation	Comments
VAR1	23	Spinal Cord length
VAR2	2.05	Spinal Cord radius
VAR3	1.1	C5 Root Transverse
VAR4	3	C5 Root Cranial Caudal
VAR5	1.83	Upper Trunk Transverse
VAR6	6	Upper Trunk Cranial Caudal

(A)

(B)

Figure 44: The model was developed through SolidWorks with each variable (length, cranial caudal thickness, transverse thickness, and angles) connected as a global variable. This global variable allows the model to easily change without the need to redo any geometrical details. For example, the model can be easily changed to match patient specific dimensions.

APPENDIX B: IN-DEPTH DESCRIPTION OF THE FEM MODEL DEVELOPMENT PROCESS CONDUCTED THROUGH ABAQUS AND SOLIDWORKS SOFTWARE

Note: This chapter was developed to describe some of the trials that occurred while developing the model. The full set of model iterations/prototypes are not described within this chapter – as there was an abundance of iterations that occurred to both the 2D and 3D models throughout this dissertation project. However, it is hoped that this detail will provide a point of departure for future research and reduce the need for others to repeat iterations that did not work.

Introduction

Computational modeling has many different aspects that need to be combined to develop a one-of-a-kind model. While many may think that computational modeling using existing software is a “plug-and-chug" exercise, there are many iterative decisions that need to be made to produce a model that accurately reflects the real-world scenario. The first step of modeling is to decide what software you are going to use. With today’s technological advancements, there are many different modeling software packages that have been developed for different computational modeling needs. For the two-dimensional and three-dimensional models discussed in **Chapters 5, 7, and 8,** ABAQUS/CAE (Dassault Systèmes) and SolidWorks (Dassault Systèmes) software were used, respectively.

At the start of this project, several different software packages were considered. Specifically, ABAQUS, FEBio, LS-DYNA, MADYMO, and Solidworks were considered and evaluated. MADYMO and LS-DYNA were being used by other members of the Grimm Research Group to develop additional model components, which was the reason that they were included in the list. The positive and negative aspects of each software package were evaluated.

For development of the 2D model, ABAQUS was the first software package considered – and it was determined to be the preferred option for this first step in model development. ABAQUS was selected for the 2D model as it allows for the development of geometry and mesh within its software, as well as the input of loads and boundary conditions. Therefore, there was no need for extra pre- or post-processing software packages when developing the model. In conclusion, the ability to run all aspects of finite element modeling, from start to finish in a single software package, seemed beneficial when developing this novel brachial plexus model.

When development of the 3D model began, it was quickly identified that ABAQUS did not easily support the complex anatomy that was needed. Attention was then turned to other possibilities, starting with MADYMO. This software is used primarily for analyzing and optimizing vehicle safety designs. While it has also been used for simulation of the effect of childbirth on the fetus using the rigid body modeling capabilities of the software, it is not generally used for models that include only finite element components. The ability to input complex geometry such as required for the 3D brachial plexus model is not as straightforward as in other software packages, and it was felt that the initial model and validation would be better accomplished through another package. LS-DYNA has many applications – from vehicle crashes and occupational safety to biomedical and medical device simulations. LS-DYNA provides the ability to develop geometry, mesh, and run simulations within the software. However, due to the complexity of the 3D brachial plexus models geometry LS-DYNA requires the use of a separate pre-processing software, such as Hypermesh (Altair) for the development of the model mesh. Because of the complexity of the geometry in the 3D model, and the need to refine each part of the geometry manually (**Appendix B**), going back and forth between Hypermesh and LS-Dyna to develop a final, meshed geometry was deemed to be counterproductive. The next software package that was researched was FeBIO. FeBIO is an open-source software tool for finite element analysis, and it is commonly used for modeling nonlinear responses for soft tissues. Though this software was designed to research biomechanical issues pertaining to biological samples, particular limitations occur within this package when developing complex geometry. First, to create an object within FeBio, the shape options include cubes, cylinders, hollowed cylinders, etc. These shapes do not allow the ability to create complex user defined spline shapes as seen in the 3D brachial plexus model. Due to the inability to precisely develop the needed complex geometry within FeBio, it was determined that it was appropriate to look at further FEM programs After careful analysis and consideration about the needs associated with the development of the 3D model, SolidWorks software was determined to be the preferred option for this first step in model development. SolidWorks software, while not a common biological FEM software, showed many benefits that would be helpful when developing this brachial plexus model. Solidworks allows the modeling process to occur from start to finish – including geometric development, material properties definition, application of loads and boundary conditions, development of mesh and mesh refinement, and lastly the ability to run and analyze simulations. The interface and options available for the geometry definition also provide the possibility of quickly changing the geometry to analyze some of the initial questions in this project, and the ability to scale the geometry in the future for further investigations.

ABAQUS Software

Modules within the software

Before one can fully develop a model through any FEM software, one needs in-depth training to be proficient in working with all aspects of the software. For ABAQUS, which has a number of modules that provide a set of functions or input capabilities for a particular task, one needs to learn the processes and limitations of the different options within each module. **Table 34** displays the different modules available in the ABAQUS/CAE software.

Table 34: Modules within ABAQUS/CAE software

Modules	Definitions
Part	Create individual parts by sketching or importing their geometry.
Property	Create section and material definitions and assign them to regions of parts.
Assembly	Create and assemble part instances.
Step	Create and define the analysis steps and associated output requests.
Interaction	Specify the interactions, such as contact, between regions of a model.
Load	Specify loads, boundary conditions, and fields.
Mesh	Create a finite element mesh.
Optimization	Create and configure an optimization task.
Job	Submit a job for analysis and monitor its progress.
Visualization	View analysis results and selected model data.
Sketch	Create two-dimensional sketches.

Note: Definitions were taken from ABAQUS documentation (91)

Module 1: Creating the Part

Through ABAQUS software, to develop a part there are many options and criteria to select from. The first step is to choose the modeling space, type, and base feature of the model, as seen in **Figure 45**. Model Space includes either 3D, 2D Planar, or axisymmetric options. Model type and base feature choices depend on the selection of the modeling space, as seen in the figure below. To first create a part, one must choose the desired base feature shape (solid, shell, wire, or point). If the model is being created in three dimensions, further options include selecting whether the part is deformable or is a discrete, rigid part. Lastly, one must also choose a type for each part that describes how it will be created (e.g., extrusion, revolution, sweep, planar, or coordinates).

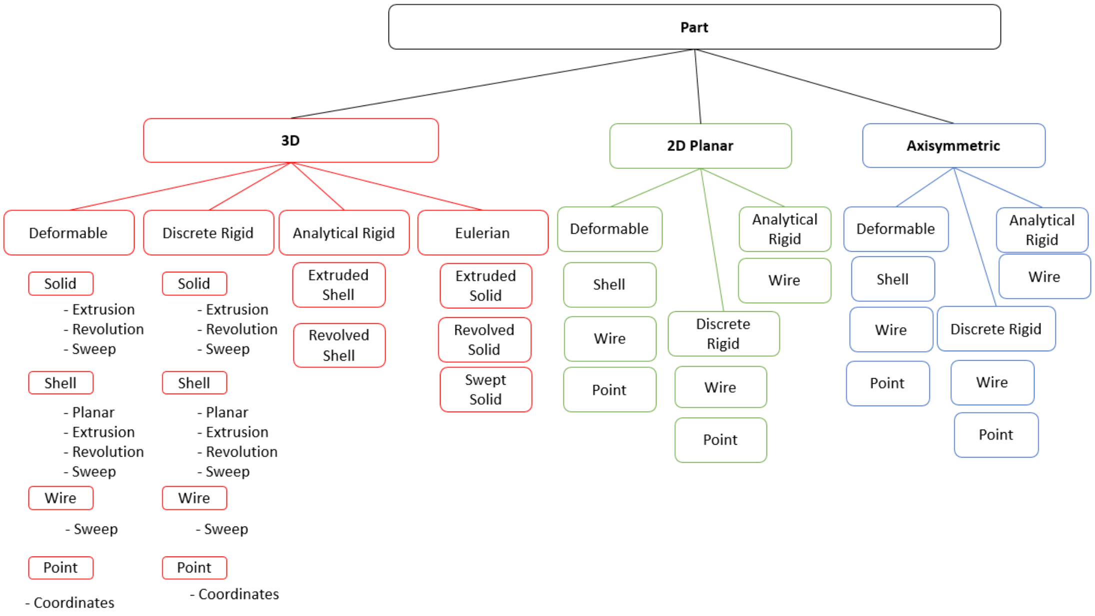

Figure 45: Diagram portraying different ways in which parts can be created within ABAQUS/CAE software. This includes selecting a Model Space (3D, 2D Planar, or axisymmetric); Model type; base feature (solid, shell, wire, or point); and type (extrusion, revolution, sweep, planar, or coordinates).

For the model described in **Chapter 5,** a 2D planar modeling space, deformable type, and a shell base feature were chosen. The choice of modeling space was based on the objective of first developing a 2D model, and the selection of a deformable structure was based on the fact that the tissue being modeled – brachial plexus nerves – is deformable. According to ABAQUS, a shell base feature is appropriate when the thickness of the solid is considered small in comparison to the width and depth. The next step in the development process was to create the geometry through the part module within ABAQUS. Geometry is developed under the Part Module, in which a multitude of shapes, lines, and points can be used to help develop a specific part.

Before geometry can be developed, one needs background knowledge of the units that are used within the software. ABAQUS is considered to be a unitless system – which requires the modeler to be conscious of which units are used for each parameter and to stay consistent. **Table 35** describes different unit systems within ABAQUS and the units that one would need to adopt for both parameters that are input into the software and results produced by the analysis.

Table 35: Unit systems used within ABAQUS/CAE software.

Quantity	SI	SI [mm]	US Unit [ft]	US Unit [inch]
Length	m	mm	ft	in
Force	N	N	lbf	lbf

Table 35 (cont'd)

Mass	kg	$tonne\ [10^3\ kg]$	$slug$	$lbf\ s^2/in$
Time	s	S	s	s
Stress	$Pa\ [N/m^2\ ]$	$MPa\ [N/mm^2]$	lbf/ft^2	$psi\ [lbf/in^2]$
Energy	J	$mJ\ [10^{-3}\ J]$	$ft\ lbf$	$in\ lbf$
Density	kg/m^3	$tonne/mm^3$	$slug/ft^3$	$lbf\ s^2/in^4$

For this project, the SI [mm] unit system was used, thus any length dimensions will be in millimeters, force will be newtons, and so forth. This unit system was selected based on the neonatal brachial plexus dimensions collected during primary reconstructive surgery. The dimensions are at an order of magnitude of millimeters rather than meters. In addition, the use of SI units is more common in scientific literature and research in comparison to US standards.

The anatomical dimensions needed to develop this two-dimensional model were collected during primary reconstructive surgery at the University of Michigan through their Neurosurgery Department, as described in **Chapter 5, Table 13**. These dimensions included the length of the roots and trunk segments, as well as the cranial caudal and transverse dimensions of each section.

The first question that was addressed was which of the collected dimensions should be used to develop this model -- were the cranial caudal or transverse dimensions the most appropriate for the thickness of the nerve roots and trunks within the two-dimensional model? Another question pertaining to dimensions related to the spinal cord – what portion of the spinal cord should be modeled: full thickness, half, or quarter? The decision on which spinal cord dimensions are used affects where the boundary conditions will be placed within the model (boundary conditions will be explained in further detail in coming sections).

The model was first developed using the transverse dimensions of the nerve roots as the thickness in the XY (coronal) plane and the entire width of the spinal cord, as seen in **Figure 26**. The results of the analysis using these dimensions and boundary conditions produced an imprecise stress solution (excess stress concentration at the T1 nerve root), which was recognized based on the fact that there is a general understanding of the expected results based on available experimental and clinical data. In addition to the impact of the dimensions, it must be remembered that other aspects of the model may have skewed the results, including the mesh, applied load, and boundary condition modules, among others.

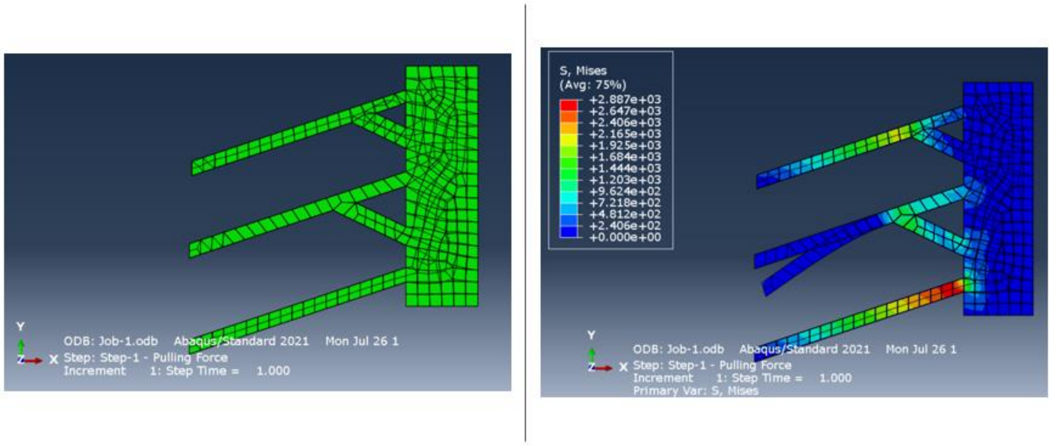

Figure 46: Model iteration using transverse nerve dimensions and entire thickness of the spinal cord.

Another iteration was developed and changed to further analyze the effect geometry has on the model. For this iteration, the dimensions used for the nerve root thickness were changed from the transverse to the cranial caudal dimensions, as seen in **Figure 47.** It was also recognized that the cranial caudal diameter did anatomically make more sense for a thickness in the coronal plane. The increase in the nerve root thickness allowed for a more refined mesh to be developed within the model. A more refined mesh within any finite element software is known to produce a more accurate result, as smaller elements in a finer mesh can more accurately capture stress gradients across the elements (1). In comparison to the previous iteration in **Figure 46** above, the stress concentration changed to show a higher stress observed in the upper trunk and C7 nerve root. While the model's anatomy was corrected to match the standard connections between the nerve roots and trunks using the cranial caudal dimensions – the results do not appear to be accurate. An accurate representation of the stress distributed within five of the nerve roots should occur. However, this model produced results that included low to no stress throughout the plexus, even when high levels of force were applied. A conclusion from this iteration was that further development was thus required to better understand this error.

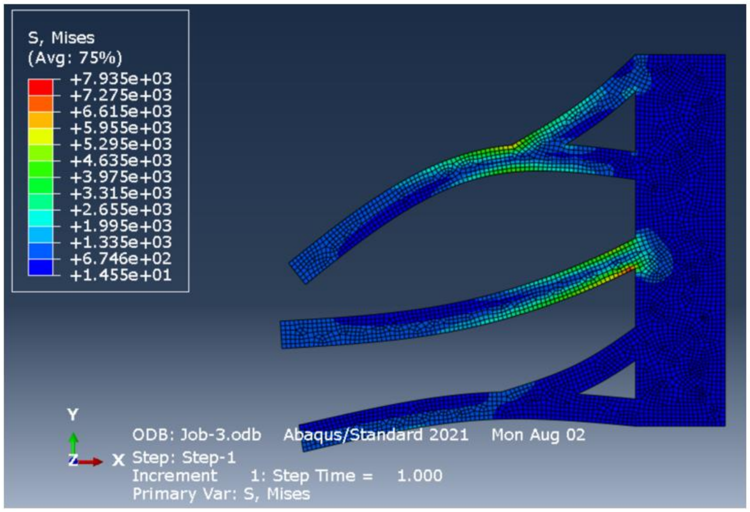

```
ODB: Job-3.odb    Abaqus/Standard 2021    Mon Aug 02
Step: Step-1
Increment     1: Step Time =    1.000
Primary Var: S, Mises
```

Figure 47: Model iteration where the thickness of nerves roots and trunks were changed to use the cranial caudal dimensions rather than transverse dimensions.

Another modeling decision worth discussing was whether to model two separate parts for the spinal cord and brachial plexus nerves rather than one solid part. The option to develop the model with two separate components seemed beneficial, as these two tissue components may have different mechanical properties. **Figure 48** displays an iteration in which a simplified spinal cord was modeled separately from the brachial plexus roots and trunks. This iteration allowed the analysis to be run with two separate parts connected through boundary conditions. The results of the analysis using two separate parts was deemed to be inaccurate because the stress concentration seemed to correspond to the elements of the model where the fixed boundary conditions were located. As many nerve root failures occur as ruptures outside of the vertebral foramen, this was not felt to reasonably represent the clinical evidence. Based on currently published literature on modeling peripheral nerves, it was determined that at this stage of the modeling using the same mechanical properties for the two portions is an appropriate assumption (67,80).

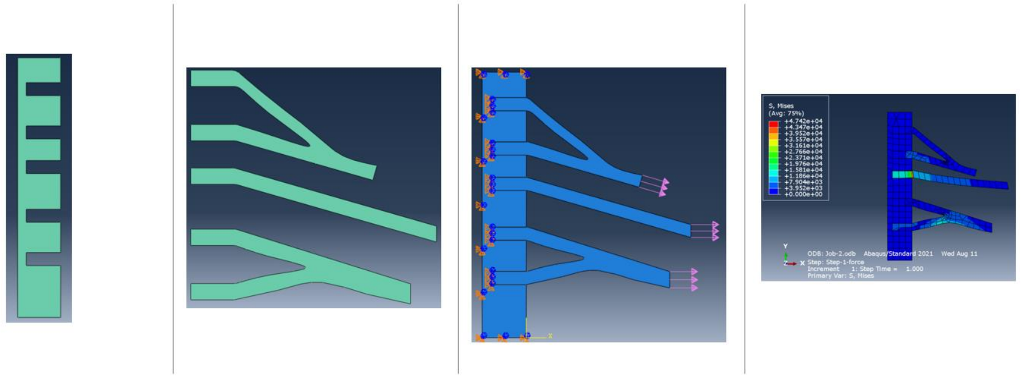

Figure 48: Model iteration describing the use of two separate parts (seen in green) and combining them with the use of boundary conditions.

In summary, the three iterations described within this section were only a few of many variations that were investigated to guide the development of the 2D model's geometry. Through this process, the following dimensions were selected for the 2D model used in the analysis discussed in **Chapter 5:** half of the width of the spinal cord; nerve roots/trunks thickness from the cranial-caudal diameter measurements **(Table 18)**; and angles based on combining the nerve roots for C5/C6 and C8/T1 with constraints on their length. The dimensions and model geometry were discussed with the University of Michigan's Neurosurgery collaborator to confirm that the anatomy was realistic. Overall, this geometry assumption represents the neonatal brachial plexus roots, trunks, and spinal cord portion to the best of our ability. The next step is to discuss assigning properties within the model.

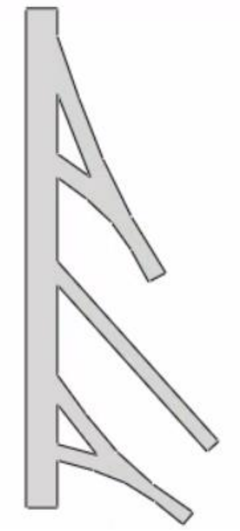

Figure 49: Two-dimensional brachial plexus model developed within ABAQUS/CAE software.

Module 2: Assign Properties

As stated in Chapter 5, there has been no assessment of the mechanical properties of the human neonatal brachial plexus. Thus, the Young's modulus and Poisson's ratio were from data collected from neonatal piglets, as seen in **Table 12** (6,80). The same material properties were used for both the brachial plexus and the spinal cord, as the model was constructed as a single, deformable structure.

Within ABAQUS software, there are many material properties to choose from including general, mechanical, thermal, electrical, and magnetic. Within the mechanical portion there are 15 general material properties as seen in **Table 36.** Within those 15 general properties, one can select through 47 specified material properties. Within this model, the material property selected was mechanical – elasticity – elastic. Within the software, the Youngs Modulus and Poisson's ratio values, seen in **Table 12**, were required to characterize the material.

Table 36: General properties under the mechanical toolbar when defining material properties within ABAQUS software.

Mechanical Material Properties
Elasticity
Plasticity
Damage for Ductile Metals
Damage for Fiber-Reinforced Composites
Damage for Elastomers
Deformation Plasticity
Damping
Expansion
Brittle Cracking
Eos
Viscosity
Super Elasticity
Crush Stress
Plastic Correlation

Module 3: Determining the Appropriate Boundary Conditions.

In addition to the geometry and material properties, the selection of boundary conditions can have a significant impact on the results of the analysis. Boundary conditions are typically investigated in parallel with geometry. The next set of iterations show how various boundary conditions were implemented and the assessment of the resulting analysis. **Figure 50** describes the different boundary condition categories that can be placed within an FEM model in ABAQUS.

There are three broad categories within the boundary condition module: mechanical, electrical/magnetic, and other. Each category has various types of conditions that can be selected based on the system that is being modeled and the desired categories of results.

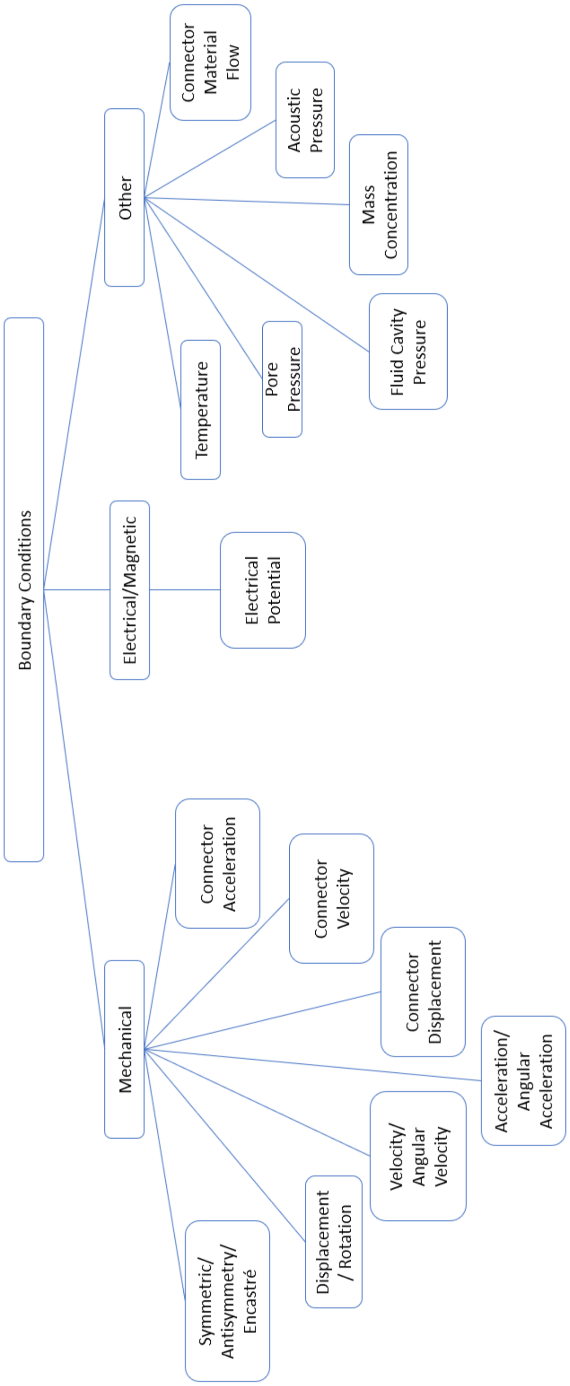

Figure 50: Categories pertaining to boundary conditions within ABAQUS software.

A finite element model can include any number of boundary conditions, and these can be specific to various portions or components of the model. A well-rounded knowledge pertaining to each boundary condition category is necessary to ensure the use of the correct condition throughout the model development process. The overall goal is to appropriately mimic the real-world constraints of the system that is being modeled, but through mathematics instead of physical conditions.

As stated in previous chapters, the brachial plexus is surrounded by many anatomical structures and components, including muscles, fascia, fat pads, etc. *In vivo* and *in situ*, tissue components are associated with each other based on location (e.g., contact), connective tissue (e.g., fascia and interstitial fat), and tissue transitions (e.g., nerve root junction into spinal cord or tendon to bone). While it is not feasible to specifically and individually portray all boundary conditions that occur within a section of the body, one must portray the overall factors that affect the response of a structure as realistically as possible to provide an analysis that has accurate results. For the 2D model, it was determined that the boundary conditions should represent: 1) the fact that the spinal cord is constrained by its location within the vertebral foramen that runs between the body of a vertebra and its posterior elements; and 2) that the displacement of the brachial plexus within the XY plane is limited by the surrounding tissues and structures. In other words, neither the spinal cord nor the brachial plexus will move significantly from its neutral position -- when the neck remains straight, and the arm remains adducted against the body.

Figure 51 portrays one of the variations investigated with respect to the use of two boundary conditions for the spinal cord and roots/trunks of the brachial plexus. These conditions include an encastré condition to the distal end of the three trunks, as well as an encastré condition to the inferior portion of the spinal cord. A traction load was placed on the superior portion of the spinal cord, parallel to its surface (-x direction). This traction force was selected to mimic the bending of the infant’s neck away from the anterior shoulder during the birthing process.

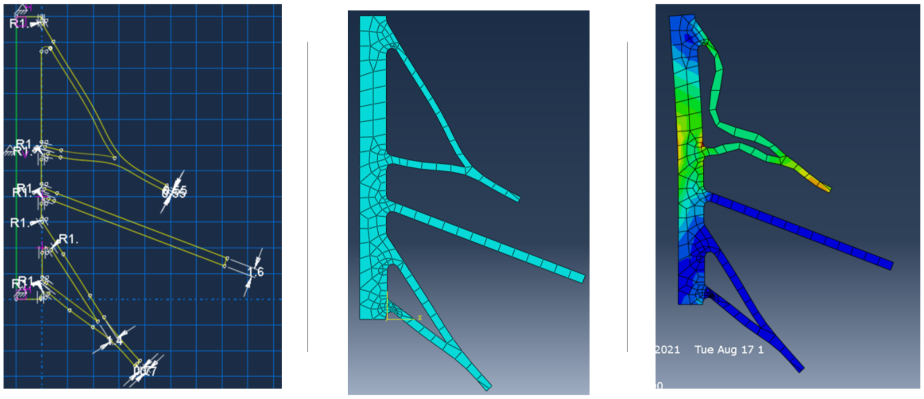

Figure 51: Model iteration describing the dimensions, mesh, and stress analysis results.

The results for using these specific boundary conditions at these locations did not match expectations based on clinical findings. In reality, it is known that neither the spinal cord nor the brachial plexus will move significantly from its neutral position *in situ*. Thus, these results show inaccuracy and further boundary condition options need to be examined.

The next trial of boundary conditions included fixing the spinal cord with two encastré conditions, one at the midline of the spinal cord and one at the inferior surface of the spinal cord. Traction was then applied to the superior surface of each of the nerve trunks. As seen in **Figure 52**, the results of using these boundary conditions and force values did not replicate what would be seen *in situ*, as the nerves would not crinkle as seen with the upper nerve roots. In addition, a high stress concentration at the midline of the spinal cord would not be accurate, as the vertebral column would encase the spinal cord and reduce the stress level at the midline of the structure (**Figure 52).** The next trial (not seen in a figure) included excluding the boundary condition on the midline of the spinal cord. When this analysis was conducted, a high concentration of stress occurred at the T1 nerve root. It is known from clinical data that a T1 nerve root injury alone is not common with the arm in the neutral position, and thus this model iteration was also not pursued.

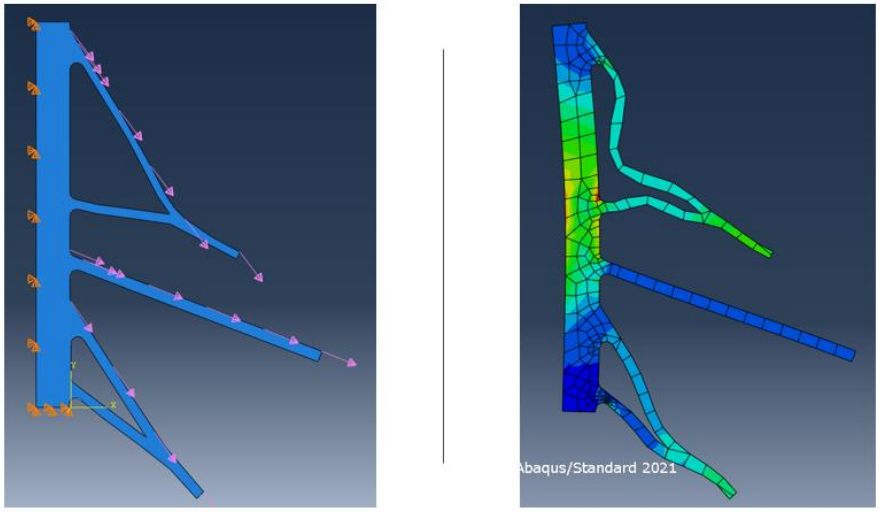

Figure 52: Model iteration describing boundary conditions and stress results. Boundary conditions included fixing an encastré condition to the midline and inferior portion of the spinal cord. Stress results did not replicate an anatomically accurate result.

If boundary conditions are not included in portions of the model that actually require them, a significant effect on the results from a model's analysis will be evident. **Figure 53** shows the results of a model with a lack of boundary conditions on the inferior and superior portion of the nerve roots. While the midline of the spinal cord is fixed with an encastré boundary condition, the distal nerve portions are free to move in all directions. The results show excess displacement at that portion of the nerves and limited stress values along the roots and trunks. This response supported adding boundary conditions that prevented abnormal upward deflection of the nerve roots and trunks when a downward force was applied to the distal end of the trunks.

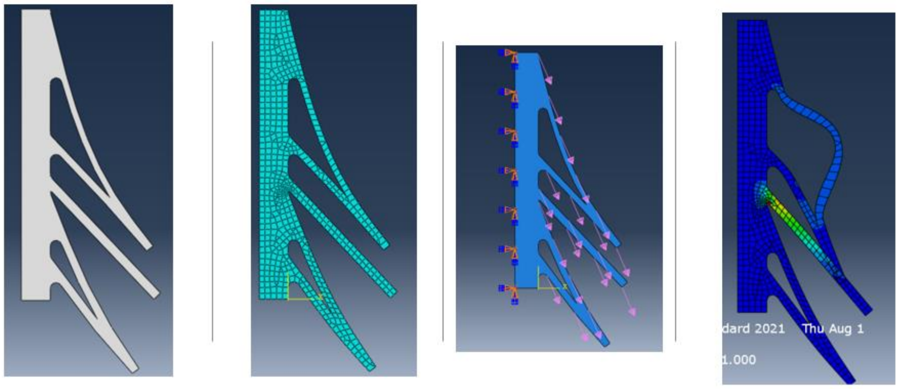

Figure 53: Model iteration describing the stress results that would occur with a lack of boundary conditions on the inferior and posterior portions of the roots and trunks.

In summary – within the two-dimensional model, boundary conditions were selected under the tab of 'Symmetry/Antisymmetry/Encastré' **(Figure 50).** Under this tab, there are eight different options to choose from. These possibilities can be seen in **Table 37.** Each option constrains deformation and deflection about specific axes of the reference coordinate systems. Two boundary conditions were selected to be placed at three different locations within the model, as seen in **Figure 54**. An encastré boundary condition was placed on the midline of the spinal cord to constrain all active structural degrees of freedom within the edge selected, and the XSYMM boundary condition was placed on the inferior and posterior surfaces of each nerve root and trunk to allow the nerve to stretch only in the plane of the model when loads were applied. An encastré boundary condition is more commonly known as a fixed boundary condition in other finite element modeling software. The XSYMM boundary condition has symmetry within a plane where X = constant (U1 = UR2 = 0). These boundary conditions were selected to represent the anatomical constraints that limit deformation or displacement of the spinal cord and nerve roots *in situ* – namely, the effects of the vertebral foramen around the spinal cord and the connective tissue and other soft tissues around the brachial plexus. The encastré and XSYMM boundary conditions can be seen in **Figure 54.**

Table 37: Boundary Conditions under the tab Symmetry/Antisymmetry/Encastré. These conditions constrain aspects of the model within specific reference coordinate planes.

Symmetry/Antisymmetry/Encastré	
Type	**Definition**
XSYMM	U1=UR2=UR3=0
YSYMM	U2=UR1=UR3=0
ZSYMM	U3=UR1=UR2=0
XASYMM	U2=U3=UR1=0; Abaqus/Standard only
YASYMM	U1=U3=UR2=0; Abaqus/Standard only
ZASYMM	U1=U2=UR3=0; Abaqus/Standard only
Pinned	U1=U2=U3=0
Encastré	U1=U2=U3=UR1=UR2=UR3=0

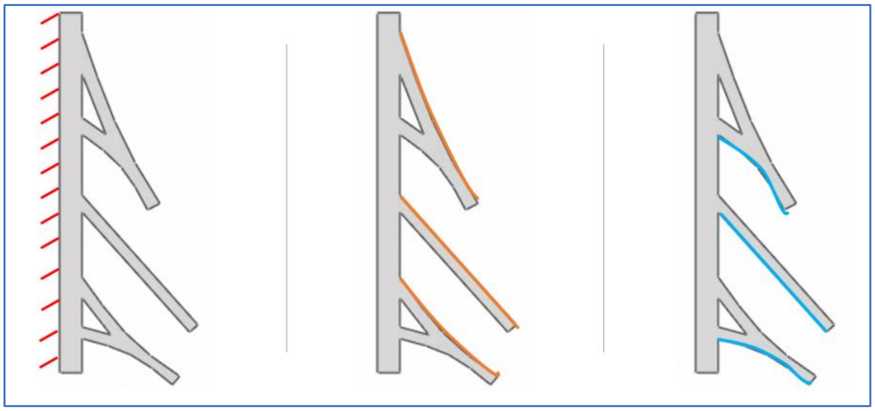

Figure 54: Boundary conditions selected to be placed on the developed two-dimensional brachial plexus model. Red: encastré; Orange and Blue: XSYMM.

Module 4: Developing Loading Conditions

ABAQUS software has seven different categories pertaining to loads. These categories include mechanical, thermal, acoustic, fluid, electrical/magnetic, mass diffusion, and other. In a two-dimensional static analysis, only three categories are of an option: mechanical, electrical/magnetic, and other. The subcategories of these three categories can be seen in **Figure 55.**

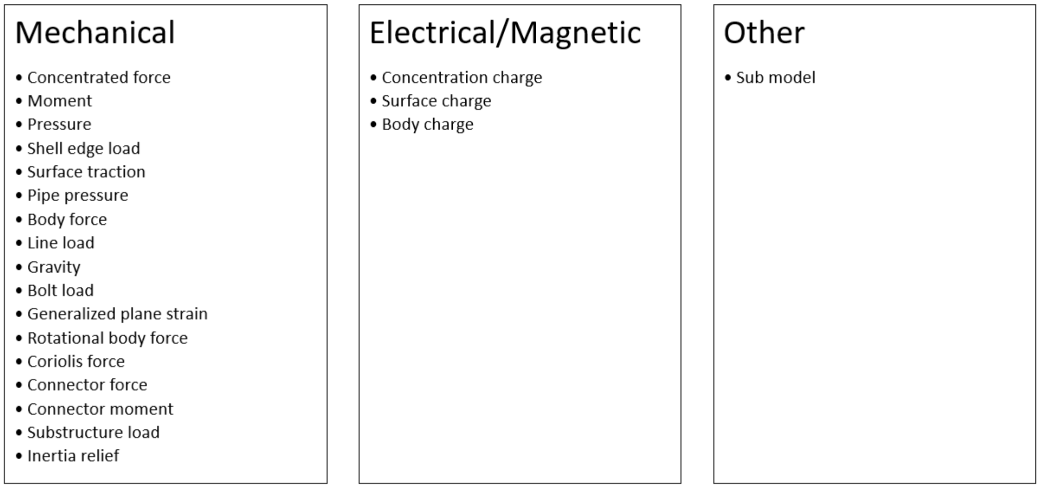

Mechanical

- Concentrated force
- Moment
- Pressure
- Shell edge load
- Surface traction
- Pipe pressure
- Body force
- Line load
- Gravity
- Bolt load
- Generalized plane strain
- Rotational body force
- Coriolis force
- Connector force
- Connector moment
- Substructure load
- Inertia relief

Electrical/Magnetic

- Concentration charge
- Surface charge
- Body charge

Other

- Sub model

Figure 55: Subcategories pertaining to loading options for a two-dimensional static analysis.

The goal from the beginning of development was to simulate a pulling force to represent what occurs to the nerves when excess force is applied to the neonate during the birthing process either through bending of the neck or depression of the shoulder. The concentrated force option was reviewed to see if it anatomically portrayed what occurs *in vivo*. Within ABAQUS, a concentration force allows one to place a force on a specific node, rather than on a line or face.

This did not represent the force distributed across the thickness of a nerve trunk, and so it was found to not be appropriate. The next condition researched included the mechanical surface traction load. Within this option, a shear surface traction can be applied as element-based or surface-based distributed loads. **Figure 56** illustrates a surface traction load at the inferior and posterior portion of the nerves. While this produced a reasonable stress pattern, the ability to replicate experimental data or compare it to previously published *in vitro* work was deemed impossible.

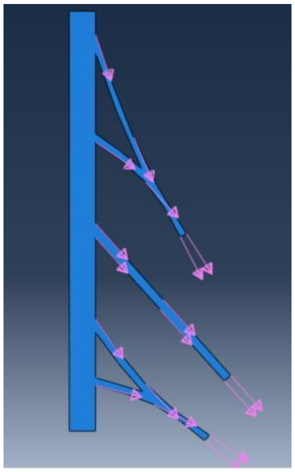

Figure 56: Surface traction loading condition applied to both the inferior and superior portions of the nerves.

In conclusion, the loading condition that was selected for this portion of the project included a mechanical – pressure condition **(Figure 57)**. This condition allows the simulation of a pulling force to occur at the distal end of each nerve trunk. The process for calculating the needed pressure value for each load is discussed in **Chapter 5.**

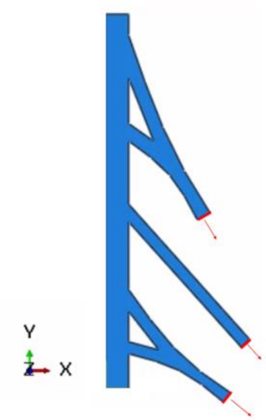

Figure 57: Final loading condition applied to the distal face of the three trunks.

Module 5: Aspects Pertaining to Mesh Development

A mesh within a finite element model is a network formed of elements and points (known as nodes). The quality of an FE mesh is an important aspect to discuss, as a low-quality mesh is likely to lower the accuracy of the finite element model. Conversely, a very fine mesh requires much higher computational time. When it comes to creating a mesh within ABAQUS software, the global seed needs to be defined through two inputs: curvature control value and minimum size control **(Table 38)**. The curvature control value allows ABAQUS to calculate the seed distribution based on the curvature of the edge along with the target element size. Furthermore, seed distribution occurs when markers are placed along edges of the part to specify the target mesh density in that region. Another aspect within the mesh controls includes selecting the element shape. Within a two-dimensional model, there are three element shape options, including quad (quadrilateral only), quad-dominated (allows triangular elements at transitions), and tri (triangular only).

Table 38: Mesh criteria within ABAQUS software.

Global Seed	
Sizing Controls	**Software Input**
Curvature Control	Maximum deviation factor
Minimum Size Control	By fraction of global size or absolute value

A mesh convergence study was conducted within ABAQUS to determine the number of required elements to ensure that the results of the analysis are not affected by the mesh size and therefore provide an accurate solution. During this convergence study, different global mesh size iterations were simulated on the same geometric model. The goal was to analyze how much the converged stress solutions changed with each mesh refinement, with a goal of having the change in calculated stress change less than 5% between steps. Following this convergence study, a maximum global mesh size of 2 mm and a minimum mesh size of 0.2 mm was selected to be used throughout the model. The model was meshed with a total of 304 nodes and 212 elements – 206 linear quadrilateral (CPS4R) and 6 triangular (CPS4).

Conclusion on the Development of the Two-Dimensional Brachial Plexus FEM

The use of ABAQUS software allowed this two-dimensional brachial plexus model to be developed and refined through many iterations. The final decisions selected for each particular condition was reviewed, discussed with medical professionals, and connected back to real world anatomical and engineering aspects to determine accuracy and effectiveness. The model used in the analysis is fully described in **Chapter 5.**

Solidworks Software

Solidworks software allows one to develop geometry, run mesh refinements, input boundary conditions (fixtures) and external loads, and run simulations with no need for any additional pre- or post-processor software. Solidworks was initially selected to create the geometry of the 3D model, as it supports the creation of 3D structures with irregular curves. A decision was then made to use it for the FEM analysis of the three-dimensional brachial plexus model as the software has the ability to run linear, non-linear, static, and dynamic analyses. As stated in previous chapters, the current model was analyzed using linear properties due to the lack of nonlinear material property descriptions for human neonatal nerves or neonatal surrogates (e.g., piglets). The lack of detail in the collected properties makes it difficult to develop the stress-strain curve needed to run non-linear analysis through the software.

The first step within SolidWorks is starting a new file as a part, assembly, or drawing. A part is defined as a 3D representation of a single design component, an assembly is a 3D arrangement of parts and/or other assemblies, and a drawing is a 2D engineering drawing, typically of a part or assembly. To begin the development process of the model within the software, one again first needs to develop the geometry.

Module 1: Development of the geometry for a three-dimensional model

The development of the geometry within Solidworks begins through the three reference planes known as front, top, and right plane. When it came to developing a complex three-dimensional model of nerves, as seen in **Chapter 7 and 8**, many offset, angle, and midplane planes were created in reference to those three main reference planes. Offset planes are developed to reference an already developed geometry, face, or plane and set a distance for the offset. An angle plane is developed through reference to known developed faces and an axis line to rotate around. Lastly, a midplane is developed equidistant between two selected faces.

Figure 58 shows the beginning process and complexity of using multiple reference planes to develop the complex geometry of the brachial plexus nerves. This figure has the upper and middle root, trunk, and division portions modeled. Within this model iteration, errors occurred pertaining to how the nerves were joined together. In this iteration, the merging of the nerve roots had inaccurate geometry, as the posterior division is seen protruding out of other nerves. A better solution to join the nerves needed to be developed.

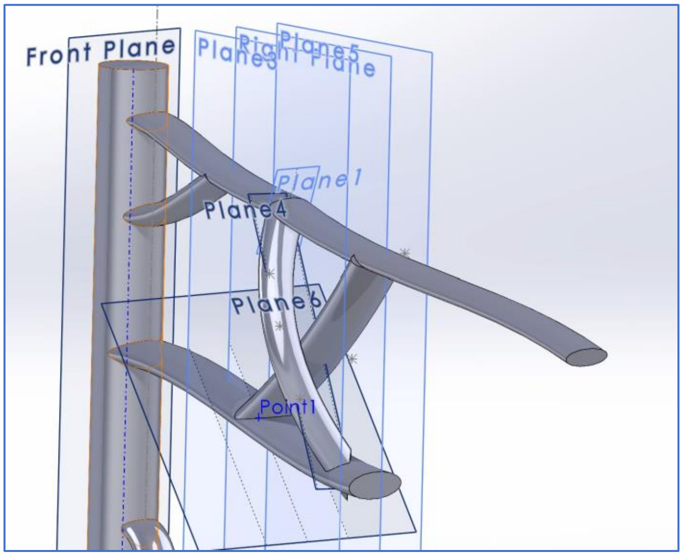

Figure 58: Solidworks geometry illustrating the use of multiple offset and angle planes to develop an iteration of the three-dimensional model.

For the development of geometry, the sketch tab within SolidWorks software has many tools to select from. One can develop sketches through the use of points, lines, and many shapes. Once a sketch is developed, the feature table has many aspects to select from to turn a 2D sketch into a 3D object, including extrude, revolve, swept, and loft. In **Figure 59Figure 59**, lofts and splines were used within the sketching tab of SolidWorks. However, the use of lofts in this iteration created an inaccuracy in the angles joining the upper and middle divisions together.

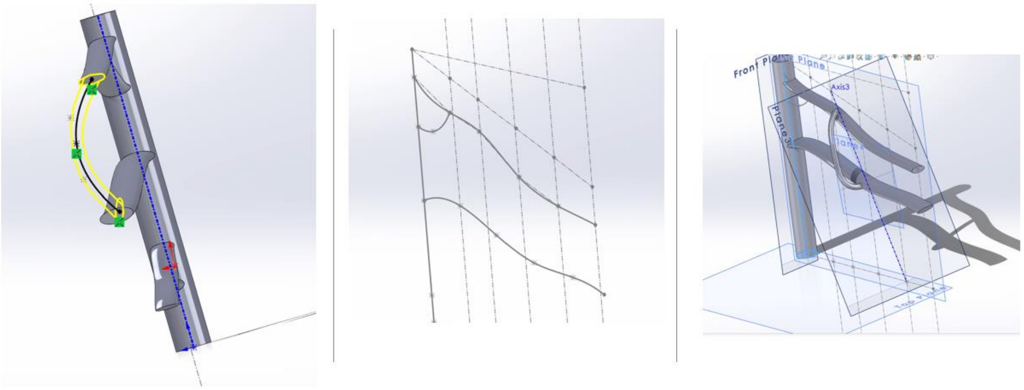

Figure 59: Portions of the lofting process within SolidWorks software, where points, reference lines, splines, and many planes are used to develop the two-dimensional sketches. A lofting tool, as seen in yellow, is used to make a loft to join the upper and middle plexus anatomy.

A major question that was asked in the beginning of the development process was how the nerves were going to join together. **Figure 60** illustrates the initial step of placing the two nerves side by side, with the goal of wrapping these shapes with a hollow cylinder acting as the epineurium. Obvious limitations would occur if this iteration was pursued, as both anatomical and mechanical characteristics would be inaccurate. It was a quick decision that this was not going to work and other avenues were discussed. **Figure 61** illustrates the use of spines, angles planes, ellipses, and merging of the nerve roots. This merging technique took many iterations to provide accurate results. The ability to merge the nerves as one solid part, as seen in **Figure 61**, allows an accurate transition point when it comes to the cross-sectional area within that portion of the model.

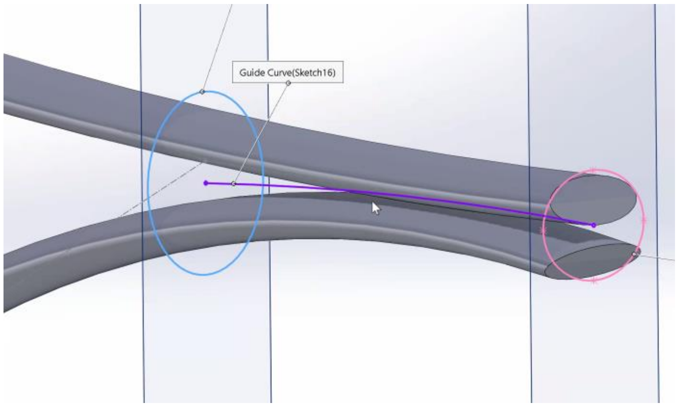

Figure 60: An iteration of the modeling illustrating a plan to wrap joining nerve sections in an epineurium.

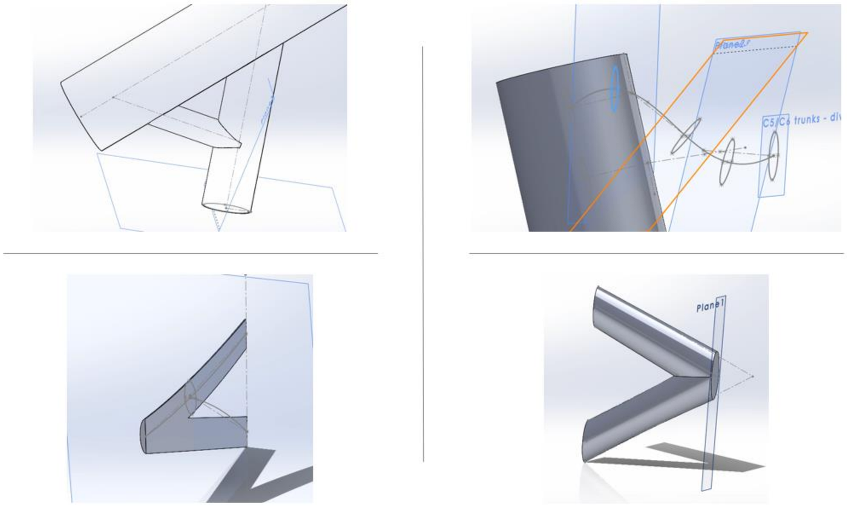

Figure 61: Refining the model through ellipses, angle planes, and splines. A lofting technique was used to merge the C5 and C6 nerve roots into one solid part.

Figure 62 is considered the prototype of our three-dimensional neonatal brachial plexus model. This prototype was implemented after dozens of geometrical iterations were developed, critiqued, and discarded. This model was the first model to be simulated with material properties, a mesh, boundary conditions, and load applied. Initially, geometry was imported into ABAQUS/CAE, but issues developed first pertaining to the transition from one software to another. Due to the complexity of the model developed within SolidWorks software, when meshing the model within ABAQUS software the mesh developed inaccurate results **(Figure 65)**. It was decided that it would be more appropriate to refine the geometry within the SolidWorks software due to the complexity of the model and the need to refine and change different aspects within the geometry. Further model iterations were simulated through the Solidworks Simulation package.

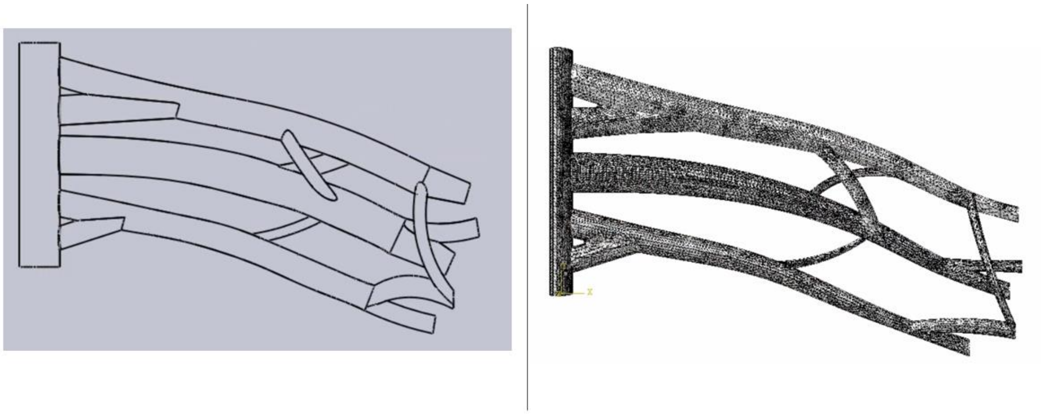

Figure 62: Geometry developed within Solidworks software and imported into ABAQUS/CAE to conduct simulation.

Visualization of *in situ* brachial plexi made it clear that the cross-sectional area of the trunks through the distal nerves, as illustrated in **Figure 62**, did not need to be constant. Discussions with the University of Michigan Neurosurgical team and review of anatomic atlases supported the refinement of the geometry into the structure presented in **Chapters 7 and 8.** While it is common to develop biological finite element models through the use of medical images, reconstructive techniques, and image processing software, this does not work for the brachial plexus due to the obstruction of key components of the plexus by the clavicle. Thus, there was a need to model every dimension and angle of the plexus by hand.

Figure 63 and 64 illustrates the final geometry used within the three-dimensional model. **Figure 63** illustrates only a fraction of the planes used within the final development of the geometry. Throughout the development of this model, there were over 300 sketched lines, shapes, and points placed within the model in addition to nine lofts, 12 fillets, and over 116 different reference planes.

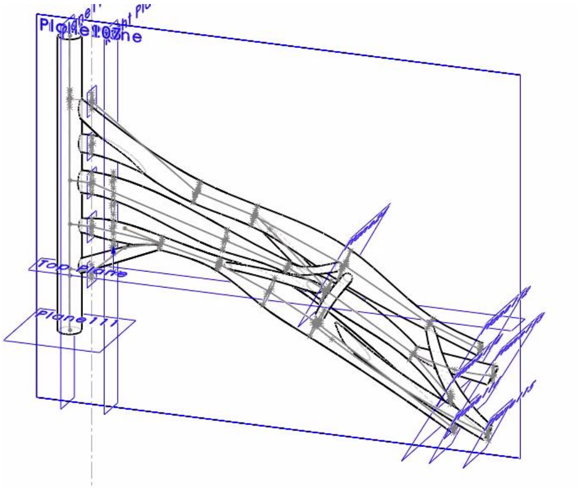

Figure 63: Final geometry developed solely by hand within Solidworks software. This model includes all five portions of the plexus including roots, trunks, divisions, cords, and terminal branches.

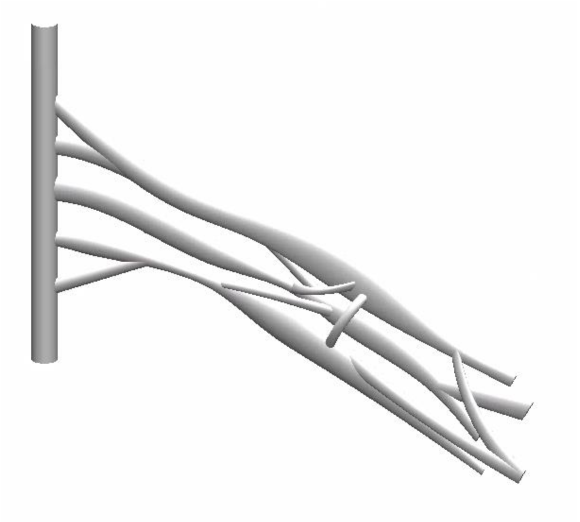

Figure 64: Shaded view of the three-dimensional model discussed in **Chapters 7 and 8.**

Module 2: Mesh Analysis

The process for three-dimensional mesh analysis has similarities and differences in comparison to the two-dimensional model discussed in the previous section. A three-dimensional mesh requires more time and computational power to mesh and solve. Additionally, three-dimensional meshes use hexahedrons, tetrahedrons, wedges, and pyramids as elements – in comparison to two-dimensional model that meshes using triangular and quadrilateral elements, as seen in **Chapter 5.**

As ABAQUS software was used to mesh our two-dimensional brachial model, the first meshing iteration occurred within that software. As stated above, due to the complexity of the model developed within SolidWorks software, when meshing the model within ABAQUS software it developed an inaccurate mesh (**Figure 65**). Subsequently, the model mesh was attempted using Hypermesh (Altair) software.

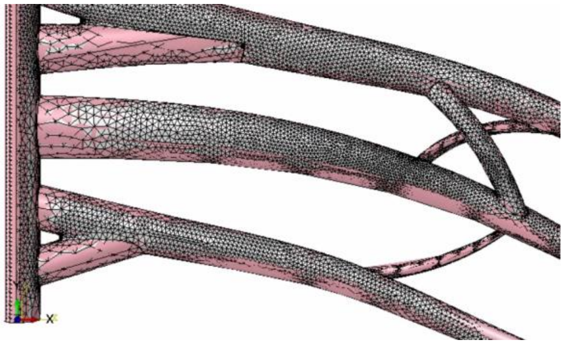

Figure 65: Inaccurate mesh developed with ABAQUS software.

Figure 66 illustrates a mesh developed within Hypermesh software. While this model iteration only included the roots and trunks of the brachial plexus, imprecise meshed elements were observed. Through Hypermesh, the ability to create a "topology refinement" may occur, which includes modifying the topology in order to obtain a quality mesh. According to Hyperworks documentation, highly complex shapes can make it hard to get a quality mesh. Thus, the conclusion was drawn that it would be necessary to test other meshing software.

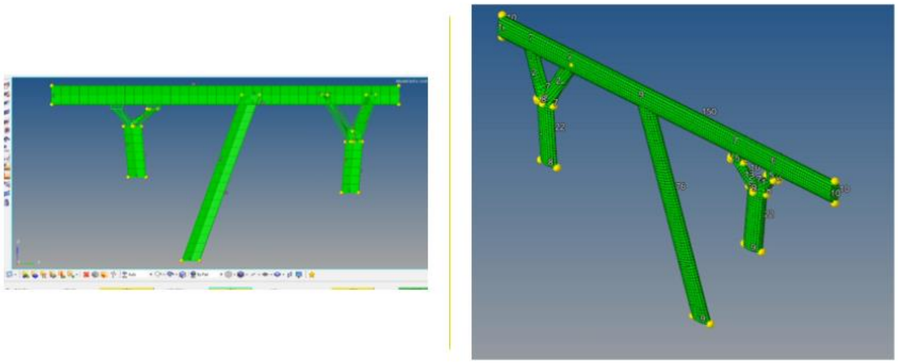

Figure 66: Mesh developed within Hypermesh software.

The use of SolidWorks Simulation to mesh and run analysis of the complete brachial plexus model was pursued. SolidWorks Simulation package has many features that correspond with the needs associated with the development of the three-dimensional brachial plexus model seen in

Chapter 7 and 8. This software allows one to develop a quick mesh or an advanced mesh through their simulation package. A quick mesh simply allows one to pick between a coarse or fine mesh in order to develop the needed mesh. The complexity of the brachial plexus model required the use of the advanced meshing option, which includes three options: standard mesh, curvature-based mesh, and blended curvature-based mesh.

Figure 67 shows the final mesh developed within Solidworks Simulation package. An advanced mesh interface was used to select the needed mesh type. A blended curvature- based mesh was used due to its ability to calculate minimum element size. This option provides the ability to capture small geometric features automatically. This was determined to be a benefit for the brachial plexus model due to the small dimensions that existed throughout the plexus.

When developing a mesh in any finite element software, a convergence study is of importance. A convergence study is the process of running the same simulation with different resolutions and analyzing how much the converged solution changes with each mesh. Within Solidworks Simulation and through the adaptive tab one can run an h-adaptive or p-adaptive convergence study. An h-adaptive mesh refinement reduces the element size in areas of high strain within three iterations until a defined tolerance level is achieved. In contrast, a p-adaptive study changes the polynomial order of the elements – up to the 5th order. Simply, the p-adaptive mesh refinement does not refine the mesh but uses progressively higher element order to improve results, while the h-adaptive mesh refinement refines the mesh and does not change the element order. In the final mesh refinement, the h-adaptive mesh was used, as stated in **Chapter 7**. **Table 39** describes the values of the three mesh iterations run in the refinement process. These three mesh iterations were simulated at first to depict a coarse, normal, and fine mesh. These iterations had different minimum and maximum element sizes. After the three mesh's were simulated, different factors were researched to conclude which mesh should be used within the final model. The factors reviewed included computational time, number of nodes, number of elements, and the change in predicted stress.

Table 39: H adaptive mesh refinement details.

Mesh	Maximum Element Size [mm]	Minimum Element Size [mm]
Coarse	4.97	0.24
Normal	2.48	0.12
Fine	1.24	0.06

In conclusion, as stated in **Chapter 7**, a 5% variation in predicted stress was selected as the tolerance level when reviewing the stress values of the mesh iterations due to the variability that exists within both the material properties and anatomy between individuals – both of which impact the precision of the results. The refinement went through iterations portraying maximum element sizes from 4 – 1.5 mm, with the corresponding minimum element sizes of 0.25 – 0.12 mm. Taking into consideration computation time, number of nodes, number of elements, and the change in predicted stress between these iterations, the mesh size selected had a maximum element dimension of 2.48 mm and a minimum of 0.12 mm. The total number of nodes within the model was 269,637, with 165,439 elements. The element shape was primarily tetrahedral.

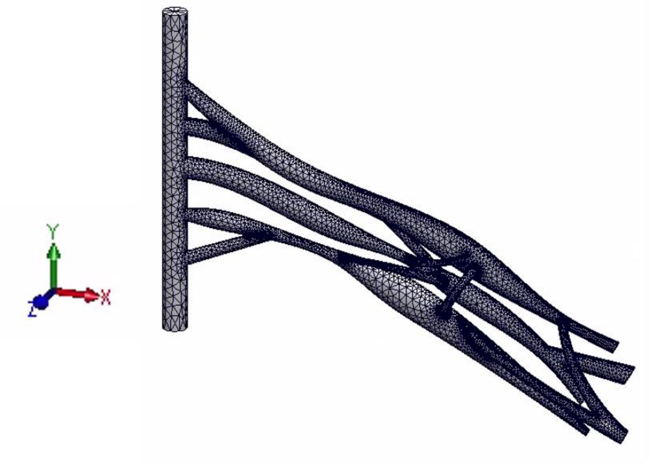

Figure 67: Final mesh developed within Solidworks software with a maximum element dimension of 2.48 mm and a minimum of 0.12 mm.

Module 3: Boundary Conditions

The next step of model development is to define the boundary conditions within the model. Boundary conditions within Solidworks Simulation are known as fixtures, which allow constraints to be defined on edges, vertices, beam joints, and faces. Specifically, they can define zero (no movement) or a prescribed value of displacement in any direction. After a few boundary condition iterations, it was concluded to use four different fixtures within the model. These fixtures were selected to mimic the complex anatomy that surrounds the brachial plexus. This anatomy includes fascia, nerves, vessels, fat pads, and muscles and helps restrain the nerves in place.

The first fixture within the model was placed on the outer face of the spinal cord geometry of the model. This finite element condition constrains all available degrees of freedom in the reference coordinate system (x, y, z) as the spinal cord is encased within the vertebral canal. This condition mimics the constraint that occurs within the anatomical complexity of human anatomy. The final three constraints include using a fixture constraint in relation to the front plane of the model along the faces of the roots through the branches of the plexus. These constrain the model by prescribing zero displacements in the + y and ± z directions – as the nerves distally extend in the + x and - y direction when traction is applied approximately parallel to their length. **Figure 68** visually shows, in blue, the faces of the nerves selected to prescribe zero displacement. This figure specifically shows arrows in the + y direction that would prescribe zero displacement in that specific direction. In summary, these four boundary conditions (fixtures) constrain the model as would occur within the human body.

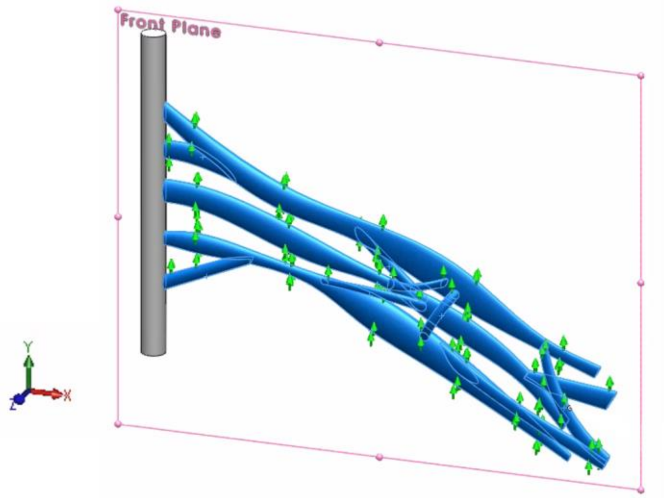

Figure 68: Sample image illustrating one of the four fixture constraints used within this model. The faces (seen in blue) are fixed with a zero-displacement constraint in the + y direction.

Module 4: External Load Conditions

The last step in model development includes selecting the external loads needed to simulate an analysis. Within Solidworks, there are many options to select to apply a load to the model. **Table 40** lists the options available within the software when selecting a load.

Table 40: Categories and definitions within SolidWorks external load tool set.

External Loads	Definition
Force	Defines a force, torque, or moment on the selected entities for the active structural study (static, frequency, buckling, or nonlinear study). The specified value is applied to each selected entity.
Pressure	Defines a pressure on the selected entities for the active structural study (static, frequency, buckling, or nonlinear study).

Table 40 (cont'd)

Gravity	Defines gravity loading for the active structural study (static, frequency, or buckling).
Centrifugal	Defines centrifugal forces (angular velocity/acceleration) for the active structural study (static, frequency, buckling, or nonlinear study).
Bearing Load	Defines bearing load on set of cylindrical faces with respect to a coordinate system for the active structural study.
Temperature	Defines a temperature on the selected entities for the active study.
Remote load/mass	Defines remote load/mass on a set of faces with respect to a coordinate system for the active structural study.

Note: Definitions were taken from SolidWorks documentation (92)

By reviewing **Table 40**, it was recognized from the beginning that the 'force' external load was the needed category to use on the model, as a pulling force would occur with the depression of the shoulder while the head and neck remained aligned with the axis of the spine during the birthing process. The orientation of how this tensile force was going to be applied took many iterations and changes.

The application of load changed throughout the development process due to the iterations that occurred with the model's geometry. **Figure 69** illustrates an iteration where the geometry of the nerve endings were first cut perpendicular to the x-axis of the model – which was a parallel cut in comparison to the spinal cord. This geometric cut on the terminal nerve endings did not seem to infer the true pulling direction that would occur if the infant experienced a force that depressed the shoulder and caused traction on the nerves. Thus, the geometry was altered to depict the terminal nerve endings cut perpendicular to the lengths of each of the nerve cords. The final external load was applied as a pulling force perpendicular to the distal, cross-sectional face of the nerve (as seen with blue arrows in **Figure 69**).

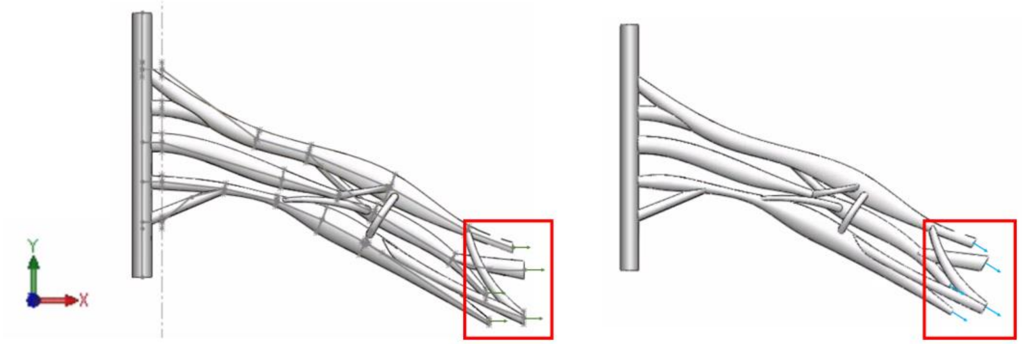

Figure 69: First model iteration, where the tensile force was applied in the positive x-direction (as seen in green). The final force iteration was applied as a pulling force perpendicular to the distal, cross-sectional face of the nerve.

Conclusion on the Development of the Three-Dimensional Brachial Plexus in SolidWorks

The use of SolidWorks software allowed this three-dimensional brachial plexus model to be developed and refined through many iterations pertaining to geometry, mesh, boundary conditions, and external loads. Similar to the two-dimensional model, final decisions selected for each particular condition were reviewed, discussed with medical professionals, and connected back to real world anatomical and engineering aspects to determine accuracy and effectiveness. The model used in the analysis is fully described in **Chapters 7 and 8**.